UNIVERSITA' DEGLI STUDI DI PARMA

SCUOLA DI DOTTORATO IN INGEGNERIA E ARCHITETTURA

DOTTORATO DI RICERCA IN INGEGNERIA CIVILE

CICLO XXVIII – CURRICULUM GEOMATICA

UAS PHOTOGRAMMETRIC BLOCKS: ACCURACY, GEOREFERENCING AND CONTROL

DISSERTAZIONE PER IL CONSEGUIMENTO DEL TITOLO DI DOTTORE DI RICERCA

COORDINATORE: PROF. ING. GIANFRANCO FORLANI
RELATORE: PROF. ING. GIANFRANCO FORLANI
TUTOR: PROF. ING. RICCARDO RONCELLA

DOTTORANDO: ING. MARINA SANTISE

PARMA, GENNAIO 2016

Ai miei cari
Papà e Mamma
per l'amore incondizionato
e a Nonna
perché è la mia roccia.

Contents

Contents I
Index of Figures V
Index of Tables XI
Index of Acronyms XV

Chapter 1 Introduction 1

1.1. Introduction 3
1.2. Motivation 3
1.3. Overview 4

Chapter 2 Unmanned Aircraft Systems 7

2.1. Introduction 9
2.2. History of UAS and current trends 9
2.3. UAS Definition 12
2.4. UAS Classification 13
2.5. Pros & Cons with respect to manned aircrafts 18
2.6. UAS platforms 19
2.6.1. HexaKopter 20
2.6.2. EASYFLY 21
2.6.3. Falcon 8 22
2.6.4. SwingletCAM 24
2.6.5. eBee 26
2.7. UAS Policy Framework 27
2.7.1. EASA 28
2.7.2. ENAC 33

Chapter 3 UAS Photogrammetry 41

3.1. Introduction 43

3.2. Potential of UAS photogrammetry 43

3.3. Flight planning 49

3.3.1. Ground Control Station: Mission planner 53

3.4. Navigation and orientation systems 55

3.5. Data processing 60

3.5.1. Camera calibration 61

3.5.2. Image orientation 63

3.5.3. Dense image matching and 3D reconstruction 68

Chapter 4 A simulation study on georeferencing UAV blocks 71

4.1. Introduction 73

4.2. BBA procedures for UAV blocks with GCP 74

4.3. Synthetic block generation and Monte-Carlo simulations 75

4.4. Simulation MC 1: accuracy of different BBA procedures 78

4.4.1. Analysis of the results 80

4.5. Georeferencing with GPS on board 84

4.6. Simulation MC 2: accuracy of GPS-Assisted Aerial Triangulation 87

4.6.1. Analysis of the results 88

4.7. Required precisions of GPS and sensitivity to gross errors in GPS positions 90

4.7.1. GPS data precision requirements 90

4.7.2. Vulnerability to gross errors 92

Chapter 5 Empirical accuracy test of UAV photogrammetric surveys 99

5.1. Introduction 101

5.2. Campus: Motivations and objectives......................................101

5.2.1. Study area 102

5.2.2. UAS survey 103

5.2.3. Ground data acquisition 105

5.2.4. Data processing 106

5.2.5. Digital Surface Model production 111

5.2.6. Conclusions 116

5.3. Accuracy assessment of a block oriented with GPS-assisted AT ……………………………………………………………...117

5.3.1. Study area and data acquisition 118

5.3.2. Block orientation 119

5.3.3. Digital Surface Model production 124

5.3.4. Conclusions 128

Chapter 6 Application of UAS photogrammetry 129

6.1. Introduction 131

6.2. Gossolengo 131

6.2.1. Study area and data acquisition 132

6.2.2. Block orientation 134

6.2.3. Digital Surface Model production 138

6.2.4. Volume Estimate 141

6.2.5. Conclusions 142

6.3. Gran Sommetta Rock Glacier..143

6.3.1. Study area 144
6.3.2. UAS photogrammetry 144
6.3.3. Ground data acquisition 146
6.3.4. Data processing 146
6.3.5. Conclusions 150
6.4. Veleia Romana 150
6.4.1. Study area and data acquisition 151
6.4.2. Block orientation 153
6.4.3. Conclusions 158

Conclusions 161

Bibliography 165

Index of Figures

Chapter 2 Unmanned Aircraft Systems

Figure 2.2.1 – Evolution of military drones from the beginning to present day: a) unmanned balloons used by Austrian to attack Venice in 1849; b) gpsunmanned aerial torpedo Kettering Bug; c) Switchblade kamikaze drone by AeroVironment; d) Gyrodyne QH-50 DASH. 10

Figure 2.4.1 – Examples of UAS categories in the world. In bold UAV classification, in italic model name in the market: a) NANO: Black Hornet by Prox Dinamics (Norway). b) MICRO: PD-100 BLACK HORNET by Prox Dynamics (Norway). c) MINI: WASP III by AeroVironment (USA). d) CR: Prion Odin aero by UAS norway (Norway). e) SR: RQ-7 Shadow by AAI corporation (USA). f) LE: Scaneagle by Insitu (USA). g) MRE: RQ-5 Hunter by Israel Aircraft Industries (Israel). h) LALE: Apoena 1000 by Xmobots (Brazil). i) MALE: MQ-1 Predator by General Atomics (USA). l) HALE: RQ-4A Global Hawk by Northrop Grumman Corporation (USA). m) UCAV: nEUROn by Dassolt Aviation (France). n) **LETH**: Terminator by AeroVironment Inc (USA). o) **DEC**: Tornado by Integrated Dynamics (Pakistan). p) **STRATO**: AirStrato by ARCA (Romania). 17

Figure 2.6.1 –The HexaKopter with the Control Station. 20

Figure 2.6.2 – EASYFLY by Eurodrone: this hexacopter has been used for the survey of Veleia Romana archeological site. 21

Figure 2.6.3 – Falcon 8 drone. 23

Figure 2.6.4 – SwingletCAM by SenseFly: fixed-wing in expanded polypropylene foam and carbon structure. It has been used for the survey of Gran Sommetta rock glacier. 24

Figure 2.6.5 – eBee RTK by SenseFly: fixed-wing in expanded polypropylene foam and carbon structure. It has been used for the survey of Gran Sommetta rock glacier. 26

Chapter 3 UAS Photogrammetry

Figure 3.2.1 – 24th March, 2011 aerial photo taken by a drone and released by AIR PHOTO SERVICE [5], the crippled Fukushima Dai-ichi nuclear power plant. From top to bottom, Unit 1 through Unit 4. (Air Photo Service Co. Ltd., Japan). 44

Figure 3.2.2 – The accuracy of measurement methods in relation to the object/area size in [39], a review of [79]. 46

Figure 3.2.3 – Flowchart of a UAS photogrammetric project. 47

Figure 3.3.1 – Geometry of the flight plan in flat areas [70]. 50

Figure 3.3.2 – Example of flight plan in Mission Planner: on the left the projection of WP on the Google Satellite Map; on the right the command list and the WP coordinates. 54

Figure 3.4.1 – Flight lines carried out in: a) manual mode (image overlap and flight height not respected); b) autonomous mode with low-cost navigation system (irregular image overlap); c) automated mode with low-cost quality navigation system. 55

Figure 3.4.2 – Comparison of low-cost antennas with the same geodetic receiver Novatel OEMV-3 in [119]. On the left plot of carrier-phase multipath RMS in cm; on the right plot of code multipath RMS in m. 58

Figure 3.4.3 – Comparison of low-cost receivers with the same geodetic antenna Novatel GPS-702-GG in [119]. On the left plot of carrier-phase multipath RMS in cm; on the right plot of code multipath RMS in m. 58

Figure 3.5.1 – Colour map of connection matrix between images of a UAS block: the brown to white colour scale indicates a decreasing number of correspondences (from high to none). 65

Chapter 4 A simulation study on georeferencing UAV blocks

Figure 4.3.1 – Monte Carlo Simulation Flowchart. 76

Figure 4.3.2 – Perspective view of the camera positions (in red), tie points (in green) and GCP (in white) for block MC 1. 77

Figure 4.3.3 – Perspective view of the camera positions (in red) and of the terrain (in white) for block MC 2. 77

Figure 4.4.1 – Scheme of MC 1 simulation: parameters and variables of “Block creation”, “Monte Carlo Simulation” with noise to image points of each sample and different techniques of BBA and the last “Comparison” step. 78

Figure 4.4.2 – Block geometry of reference blocks: 1.a, 1.b, 2.a, 2.b. The camera positions (blue square), tie points (black dots) and GCP (green triangles) are indicated. 80

Figure 4.4.3 – Case 1.b: 60-20% overlap, tie point on a regular grid block oriented in free-net adjustment (on the left) and with GCP (on the right). Color map of the mean error distribution in Z. Note: color scales are different. 82

Figure 4.4.4 – Case 2.b: 60-60% overlap, tie point on a regular grid block oriented in free-net adjustment (on the left) and with GCP (on the right). Color map of the mean error distribution in Z. Note: color scales are (slightly) different. 82

Figure 4.4.5 – Plot of tie point multiplicity on von Gruber bands: a) 60-20% overlap; b) 60-60% overlap. As shown in Legend the lower number is 2, indicated in purple, the higher number is 9, indicated in dark green. 83

Figure 4.4.6 – Plot of multiplicity of tie points on a grid: in the case of 60-60% overlap. The lowest value is 2 (purple colour), the highest is 9 (dark green colour). 83

Figure 4.6.1 – Scheme of MC 2 simulation with parameters of “Block creation” step, “Monte Carlo Simulation” with noise added to image points and GPS antenna positions for orientation using GPS-AT and the last “Comparison” step. 88

Figure 4.6.2 – Color map of the mean square error distribution of ground coordinates of the MC 2: a) σ_x, b) σ_y, c) σ_z. 90

<u>Chapter 5 Empirical accuracy test of UAV photogrammetric surveys</u>

Figure 5.2.1 – The area used for the case studies. In light yellow the 140 m high flight zone, in blue the 70 m flight zone. Yellow, blue and red dots show the GCPs used respectively for both case studies, only for the 140 m flight and only for the 70 m flight. 102

Figure 5.2.2 – GCP and CP distribution and categorization over the area of interest. 105

Figure 5.2.3 – Types of marker for Ground Control and Check Points. 105

Figure 5.2.4 – Image overlap and camera locations of 140 m flight..................... 108

Figure 5.2.5 – Distribution of 9 GCPs for the block orientation in the a) version. 109

Figure 5.2.6 – Image overlap and camera locations of 70 m flight 110

Figure 5.2.7 – DSM of flight at 140 m and GPS survey points location. 113

Figure 5.2.8 – Raster at 20 cm resolution of the differences between the 140 m flight DSM with 28 GCPs (brown and light blue triangles) and 9 GCPs (light blue triangles). 113

Figure 5.2.9 – DSM of 70 m flight and GPS survey locations. 114

Figure 5.2.10 – Detail of the difference between the DSMs of the 140 m and 70 m flight (raster at 20 cm resolution).......... 115

Figure 5.3.1 – Location of 16 Ground Control Points: in green the 13 points used as check points for the RTK- oriented block.......... 119

Figure 5.3.2 – Tie points extracted for the GCP and GPS oriented blocks.......... 120

Figure 5.3.3 – Camera location and image ground coverage of the block.......... 120

Figure 5.3.4 – Residuals on camera locations (black dots). Z residuals are represented by the ellipse colour. X, Y residuals are represented by the ellipse semi-axes.......... 121

Figure 5.3.5 – The RTK GPS Camera location, in pink the cameras fixed for georeferencing the block.......... 123

Figure 5.3.6 – Colour map at 0.5 m resolution of the differences (m) between the GCP DSM and the all GPS DSM with location of Check Points (blue triangles).124

Figure 5.3.7 – Raster at 0.5 m resolution of the differences (m) between the GCP and all GPS DSMs DSMs in the active glacier area. 126

Figure 5.3.8 – Image residuals from the self-calibrating BBA. 126

Figure 5.3.9 – Raster at 0.5 m resolution of the differences (m) between the GCP and half GPS DSMs. 127

Figure 5.3.10 – Differences between point clouds oriented with GCP (reference data) and GPS on-board on the active glacier area. 128

Chapter 6 Application of UAS photogrammetry

Figure 6.2.1 – Volume estimation of gravel heap: images acquired by HexaKopter in a preliminary phase of flight (upper); 3D model reconstruction of the quarry (lower).......... 132

Figure 6.2.2 – Flight lines performed during the survey.......... 133

Figure 6.2.3 – Types of marker for Ground Control Points. 133

Figure 6.2.4 – The two GCP configuration: on the left 10 GCP and 11 CP, on the right 6 GCP and 15 CP..137

Figure 6.2.5 – Differences between the DSMs generated by the same software with the two configurations of GCPs. From top to bottom, left to right: Agisoft PhotoScan, Dense Matcher and PhotoModeler...139

Figure 6.2.6 – From top to bottom: differences between the Agisoft PhotoScan model and, respectively, Dense Matcher and PhotoModeler (configuration with 10 GCPs)..140

Figure 6.3.1 – Type of signalized marker for Ground Control Point...................145

Figure 6.3.2 – Camera location and image overlap of 2012 flight (on the left) and of the 2015 flight (on the right)...145

Figure 6.3.3 – Location of GCPs. 146

Figure 6.3.4 – Localization of the 48 GNSS measured points.............................148

Figure 6.4.1 – Veleia Romana archaeological site: 1- Forum, 2 - Basilica, 3 – Thermae, 4 – Residential district, 5 - Cistern. 151

Figure 6.4.2 – Photogrammetric targets (left and centre) and laser scan target (right). 151

Figure 6.4.3 – On the left camera locations, on the right image overlap of the Flight 1. 152

Figure 6.4.4 – The homologous points found between images of Flight 1 (top) and of Flight 2 (bottom): the erroneous match, highlighted by red arrows, regards a feature located in the Forum for the Flight 1 and in the Cistern in the Flight 2....155

Figure 6.4.5 – Test 1- RGB: the images of Flight 1 and Flight 2 were oriented in two distinct models in VisualSFM after the automatic orientation......................156

Figure 6.4.6 – Test 1 RGB: Flight 1 and Flight 2 oriented in a single block in PhotoModeler Scanner after manual collimation of some tie points and input of EO parameters extracted from separate PhotoScan orientations................................156

Figure 6.4.7 – Camera locations and 3D points of the flights automatically oriented: on the left, Test 2 – Relative Height Flight, on the right Test 3 – NIR..157

Figure 6.4.8 – Test 5 - ALL: Link between images after the process of automatic orientation. In the upper part, the connection found between the nine images of the

SwingletCAM, in the lower part the isolated three oriented images of the Easyfly. 157

Figure 6.4.9 – Colour map of the connection matrix between the twelve images of the 4 flights after the automatic orientation in Test 5 - ALL: the brown to white colour scale indicates a decreasing number of correspondences (from high to none). The images of the Flight 1 have high correlation each other but none with SwingletCAM flights. 158

Index of Tables

Chapter 2 Unmanned Aircraft Systems

Table 2.4.1 – UAV Classification. 14

Table 2.4.2 – Major features of fixed-wing versus rotary-wing platform. 15

Table 2.6.1 – Technical specifications of HexaKopter. 21

Table 2.6.2 – Technical specifications of UAS EASYFLY. 22

Table 2.6.3 – Technical specifications of UAS Falcon 8. 24

Table 2.6.4 – Technical specifications of UAS SwingletCAM. 25

Table 2.6.5 – Technical specifications of UAS eBee. 27

Chapter 3 UAS Photogrammetry

Table 3.2.1 – Features of aerial, close range and UAV photogrammetry, from [39]. 45

Table 3.3.1 – Flight Planning of UAV survey on the Campus of Parma with the same values of flight height, sensor camera, overlap and area of interest, but with short image size along (A) or across (B) flight direction. 52

Table 3.4.1 – Characteristics of low-cost antennas (upper) and receivers (lower) (italic: geodetic-grade) from [119]. 57

Chapter 4 A simulation study on georeferencing UAV blocks

Table 4.4.1 – Feature of blocks run in MC 1. 79

Table 4.4.2 – Mean square errors (MSE) of the ground coordinates of the MC 1 simulations: in the upper part (blue rows) BBA with GCP, in the lower part (grey rows) results for the CV method before and after Helmert transformation (R3D). 81

Table 4.6.1 – Minimum, maximum and mean square errors of the ground coordinates of the MC 2 simulations. 89

Table 4.6.2 – Theoretical precisions of ground points in square blocks oriented with GCP. 89

Table 4.7.1 – Orientation with GCP: Theoretical precisions on ground coordinates. 91

Table 4.7.2 – GPS assisted aerial triangulation (σx ,σy :3 cm, σz:5 cm): Theoretical precisions on ground coordinates..91

Table 4.7.3 – Precisions on ground coordinates using different precision of GPS data w.r.t. control with GCP: in light blue the Geodetic category (σz: 30-50 mm) is indicated; in green the Low-Cost category (σz from 150mm) is indicated............92

Table 4.7.4 – List of combination of Shift errors on antenna coordinates input in the GPS-assisted AT. Central strip errors (left); lateral strip errors (right)............93

Table 4.7.5 – List of Shift errors imposed on the central (left) and on the lateral strip (right) antenna coordinates of the reference block...94

Table 4.7.6 – Statistics of Ground coordinates corrections for the simulation cases 21-29 of shift error on the Central strip of the block. 95

Table 4.7.7 – Statistics of Ground coordinates corrections for the simulation cases 21-29 of shift error on the Lateral strip of the block...95

Table 4.7.8 – Statistics of Ground coordinates corrections for the simulation cases with 20 cm shift error on the Lateral strip of the block. 96

Table 4.7.9 – Effect of shift error only on tie point coordinates............................96

Table 4.7.10 – Statistics of ground coordinates corrections for the simulation cases with 20 cm drift error on the Lateral strip of the block..97

Table 4.7.11 – Effect of drift error only on tie point coordinates. 97

Chapter 5 Empirical accuracy test of UAV photogrammetric surveys

Table 5.2.1 – UAS flight plan characteristics at 140 m. 104

Table 5.2.2 – UAS flight plan characteristics at 70 m. 104

Table 5.2.3 – Inner orientation parameters of the self and analytical calibration. 107

Table 5.2.4 – Flight 140: coordinates difference value in the three configuration of UAS block on all CPs, on buildings and on the ground.......................................110

Table 5.2.5 – Flight 70: RMSE of total CPs, of CPs on buildings and on the grounds...111

Table 5.2.6 – Differences in elevation between the DSM 140 (version block with 28 GCPs and 9 GCPs) and CPs..112

Table 5.2.7 – Differences between Kinematic GPS and DSM 70 with 20 GCPs. 114

Table 5.3.1 – Summary of the eBee RTK flight parameters................................118

Table 5.3.2 – Statistics of the residuals on the Projection Centres for the block georeferenced with all RTK GPS camera location. 121

Table 5.3.3 – Statistics of the errors (discrepancies) at the 12 CP for the block georeferenced with all GPS-determined camera stations.................................... 122

Table 5.3.4 – Statistics of the errors (discrepancies) at the 12 CP for the block georeferenced with half GPS-determined camera stations. 123

Table 5.3.5 – Differences between raster DSMs from GCP and GPS on board (all and half camera stations) 125

Table 5.3.6 – Differences between the DSM raster differences at 0.5 m resolution and the error on the 12 Check Points (all and half camera stations). 125

Table 5.3.7 – Differences between GCP and GPS on board point clouds. 127

Chapter 6 Application of UAS photogrammetry

Table 6.2.1 – Calibration parameters estimated by PhotoModeler Scanner V.7.2012.2.1.. 134

Table 6.2.2 – Parameters of the three dataset: EyeDEA, PM and PS. 136

Table 6.2.3 – RMS of coordinates differences between the two GCP configurations. 137

Table 6.2.4 – RMS of the standard deviations of the TP coordinates, estimated by the BBA with 10 GCPs. 137

Table 6.2.5 – RMSE on the CPs: BBA with 10 GCP (top); BBA with 6 GCP (bottom). 138

Table 6.2.6 – Differences in each software between the volumes computed for the two configurations of GCPs. 142

Table 6.2.7 – Differences between the Agisoft PhotoScan estimated volume, respectively, the Dense Matcher and PhotoModeler ones. 142

Table 6.3.1 – Summary of the UAS flights characteristics. 145

Table 6.3.2 – Statistics of the comparison between the GNSS elevation data and the photogrammetric reconstructed DSM for the 2012, 2014 and 2015 flights.......... 147

Table 6.3.3 – Statistics of the ground coordinates for the two BBA configurations. 149

Table 6.3.4 – Summary of the UAS flights parameters for the July - August 2015 flights. 149

Table 6.3.5 – Statistics of the 9 CPs residuals for the July and August 2015 flights. 149

Table 6.4.1 – Summary of the UAS flight characteristics. 153

Table 6.4.2 – Summary of the performed test... 154

Index of Acronyms

AAT	Automated Aerial Triangulation
ABM	Area Based Matching
AGL	Above Ground Level
ANN	Approximate Nearest Neighbour
A-NPA	Advance Notice of Proposed Amendment
ANS	Air Navigation Services
APM	ArduPilotMega
ARPAVdA	Agenzia Regionale per la Protezione dell'Ambiente Regione Autonoma Valle d'Aosta – Environmental Protection Agency of Valle d'Aosta
ASIFT	Affine SIFT
ATM	Air Traffic Management
BA	Bundle Adjustment
BBA	Bundle Block Adjustment
BLOS	Beyond Line Of Sight
CofA	Certificate of Airworthiness
CR	Close Range
CV	Computer Vision
DASH	Drone Anti-submarine Helicopter
DEC	Decoys
DEM	Digital Elevation Model
DGPS	Differential Global Positioning System
DICA	Department of Civil and Environmental Engineering of Milan Polytechnic
DSM	Digital Surface Model
EASA	European Aviation Safety Agency
EC	European Commission
ENAC	Ente Nazionale per l'Aviazione Civile – Italian Civil Aviation Authority
EO	Exterior Orientation
ETSO	European Technical Standard Order
EURO UVS	European Unmanned Vehicle Systems Association
EVLOS	Extended Visual Line Of Sight
FBM	Feature Based Matching

GCP	Ground Control Point
GCS	Ground Control Station
GLOH	Gradient Location and Orientation Histogram
GNSS	Global Navigation Satellite System
GPS	Global Positioning System
GS	Ground Station
GSD	Ground Sampling Distance
HALE	High Altitude Long Endurance
HGIS	Historical Geographic Information System
IMU	Inertial Measurement Unit
INS	Inertial Navigation System
IO	Interior Orientation
JARUS	Joint Authorities for Regulation of Unmanned System
LALE	Low Altitude Long Endurance
LE	Long Endurance
LETH	Lethal
LSM	Least Square Matching
MALE	Medium Altitude, Long Endurance
MAV	Micro Aerial Vehicle
MC	Monte Carlo
MEMS	Micro Electro Mechanical Systems
MP	Mission Planner
MPGC	Multi Photo Geometrical Constrained
Mpixel	Megapixel
MR	Medium Range
MRE	Medium Range endurance
MSE	Mean square errors
MSs	Member States
MTOM	Maximum Take-Off Mass
MVS	Multi View Stereo
NAAs	National Aviation Authorities
NRTK	Network Real Time Kinematic
OA	Operation Authorization
PARS	Photogrammetry and Remote Sensing
PC	Projection Centres
PDOP	Position Dilution Of Precision
PM	PhotoModeler Scanner
PPx	Principal Point x coordinate

PPy	Principal Point y coordinate
PS	Agisoft PhotoScan
qe	Qualified Entity
RC	Remote Controlled
RMSE	Root Mean Square Error
ROC	Remote Operator Certificate
RPA	Remotely Piloted Aircraft
RPAS	Remotely Piloted Aircraft System
RPV	Remotely Piloted Vehicle
RTC	Restricted Type Certificate
RTK	Real Time Kinematic
SfM	Structure From Motion
SIFT	Scale Invariant Feature Transform
SLR	Single Lens Reflex
SR	Short Range
STRATO	Stratospheric
SURF	Speeded Up Robust Features
TC	Type Certificate
TLS	Terrestrial Laser Scanning
TP	Tie Points
TTFF	Time To First Fix
UA	Unmanned Aircraft
UAS	Unmanned Aircraft Systems
UAV	Unmanned Aerial Vehicle
UCAV	Unmanned Combat Aerial Vehicle
UVS	Unmanned Vehicle Station
VLOS	Visual Line of Sight
VRS	Virtual Reference System
VRX	Virtual Rinex
VTOL	Vertical Take-Off and Landing
WP	Waypoint

Chapter 1
Introduction

1.1. Introduction

The use of UAVs is having a big impact on photogrammetry. Quoting Professor Armin Gruen of ETH Zurich “It is safe to say that in the years to come, we will see an increase in UAV making activities, both in terms of hardware and software development, a most interesting and challenging area for research, development and practice. This makes a clear transition from toys to tools.” [57]. What has made this transition possible are small digital cameras and powerful software that enable large numbers of small format images to be calibrated and oriented through use of photogrammetric block adjustment. UAVs have significant advantages over traditional air photography, including being highly transportable which allows for rapid mobilisation. UAVs can also typically operate below cloud coverage, making them less dependent on weather conditions. They can operate at a flying height of 150 metres above ground level and can achieve a ground sampling distance (GSD) of 5 cm or smaller. UAVs however are not without problems. Strong or even moderate wind for light models can make it impossible to fly or anyway to respect a flight plan. The introduction of regulation from aviation authorities after years of freedom of operation is perhaps the key fact that may hamper the dramatic developments of the last 10 years. Permission to fly is required in many countries and standards and certification of hardware are being enforced to ensure safe operation; public concern on safety as well as privacy issues is mounting. Academics and amateurs have been using UAVs for a long time for research purposes or for fun; now entering a commercial stage as a tool for mapping companies, the introduction of standards can be expected.

1.2. Motivation

The growing use of UAS (Unmanned Aircraft Systems) platform for aerial photogrammetry comes with a new family of Computer Vision highly automated processing software expressly built to manage the peculiar characteristics of these blocks of images. It is of interest to photogrammetrists and professionals, therefore, to find out whether the image orientation and DSM generation methods implemented in such software are reliable and the DSMs and orthophotos are accurate. On a more general basis, it is interesting to figure out whether it is still worth applying the standard rules of aerial photogrammetry to the case of drones, achieving the same inner strength and the same accuracies as well.

UASs are today a viable alternative for collecting remote sensing data for a wide range of applications in agriculture, cultural heritage, restoration, environmental monitoring, safety, cadastral management, map updating, etc… All the above-mentioned applications need a metric validation and reliability of results for the acquired data to be suitable to their purposes. It is in this matter that the photogrammetrists question about the accuracy of the results.

In particular, the topic of this work concerns the quality control, in terms of both accuracy and reliability of UAS photogrammetric blocks. Investigations have been performed by a series of Monte Carlo (MC) numerical simulation over synthetic blocks in order to study impact of the block control and the camera network design on the block orientation accuracy.

1.3. Overview

The thesis consists of six chapters, as follows.

Chapter 2 provides a general overview of the UAS world with definition, history and classifications, highlighting advantages and possible limitations in their use. To exemplify the characteristics of UAS employed for civil photogrammetric applications, a brief description of the drones used in this work is provided. Finally, the current (summer 2015) status of regulations for civil drone applications in the European and Italian context is given with a discussion on potential consequences on survey applications.

Chapter 3 describes the flow chart of Unmanned Aerial Systems photogrammetric projects, to give an overview of the features, issues and state of the art and to point out similarities and differences with respect to aerial analogue and digital photogrammetry.

Chapter 4 investigates from a theoretical standpoint the accuracy and reliability issues, through the above mentioned Monte Carlo (MC) simulations. The random error propagation from image to ground coordinates is simulated to find out to what extent systematic deformations are controlled by image redundancy, ground control and dense tie point distribution. In addition, GPS-assisted aerial triangulation accuracy requirements and reliability is examined, again by MC simulations.

In Chapter 5 the two most significant empirical investigations on UAS photogrammetry among those investigated by the author are presented. The former case study DSM focus on the verification of the accuracy of block orientation ad of DSM generation in a testfield set up at the Campus of Parma University. The latter describe the first results on the accuracy of a UAS block oriented with GPS-assisted aerial triangulation in the survey of a rock glacier using RTK positioning from a on-site ground station.

Finally, Chapter 6 describes three case study of application of UAS photogrammetry in volume estimation, periodic survey of a rock glacier displacements and the survey of an archaeological site with sensors in the visible and near-infrared spectrum.

Chapter 2
Unmanned Aircraft Systems

2.1. Introduction

Drones have been used in military applications for many years. Nevertheless, the phenomenal development of drones has made accessible to everyone this technology. Without rules for civilian applications, anyone interested has been able to build, fly, sell and advance the technology.

This chapter provides a general overview of the Unmanned Aerial Vehicles (UAV) world: history, definition, and classifications are summarised together with advantages and possible limitations in their use. Then, the drones employed in this work were describes. Finally, regulations for civilian applications in the European and Italian context are provided.

2.2. History of UAS and current trends

Until a few years ago development of UAV was an exclusively military affair. Depending on how broad is your definition of drone, their history might date back centuries.

Many authors consider hot-air balloons, which were developed in the late 16th century, to be the first step towards modern UAVs, (see Figure 2.2.1). These were first used for military purposes when the Austrians attacked Venice in 1849, using unmanned balloons equipped with explosives controlled by time fuses (Figure 2.2.1 - a). These balloons, of course, could not be remotely controlled and backfired when they were flown back by wind over the Austrian lines.

A further step towards modern drone systems was the ‘Kettering Bug’, developed by the US army in the final stages of World War I. The ‘Bug’ (Figure 2.2.1 – b) was a 4 m long biplane that carried an 80 kg warhead and resembled a missile more than a drone. Sometime after launch, the engine would shut off, the wings would be released, and the ‘Bug’ would plunge to earth and detonate on impact. The ‘Bug’ is considered a precursor of today’s drones because the development of drones and missiles took place simultaneously. Advances in one system influenced those in the other. This also explains why ambiguities regarding definitions still exist. Some modern systems such as so-called “kamikaze drones” are difficult to classify, resembling drones as well as missiles. A recent example is the Switchblade made by AeroVironment (Figure 2.2.1 - c): it is able to crash into its target with an explosive warhead to destroy it; it is small enough to be carried in a backpack and can be launched from a variety of ground, maritime, and air platforms.

A milestone for UAV development was the introduction of the Gyrodyne QH-50 DASH (Drone Anti-submarine Helicopter) in the early 1960s. The ‘Dash’ was a vertical take-off UAV which could fly from the deck of ships. Armed with two torpedoes, it was used by the US Navy to fight enemy submarines. Unlike the ‘Kettering Bug,’ the ‘Dash’ could be piloted remotely and was recoverable; it can thus be considered the first real armed drone.

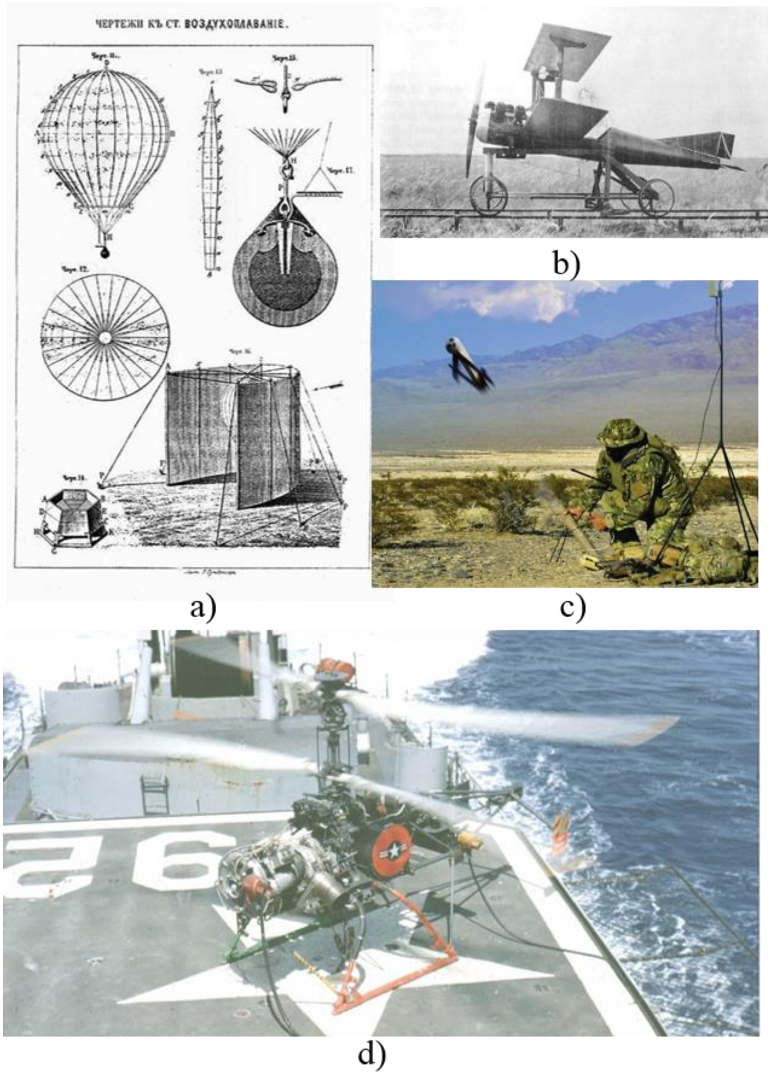

Figure 2.2.1 – Evolution of military drones from the beginning to present day: a) unmanned balloons used by Austrian to attack Venice in 1849; b) unmanned aerial torpedo Kettering Bug; c) Switchblade kamikaze drone by AeroVironment; d) Gyrodyne QH-50 DASH.

The heyday of drone development began after the 1982 Lebanon War. Israel’s successful use of drones to destroy enemy surface-to-air missiles attracted a lot of attention. Thereafter, armed forces around the world, particularly in the US and Israel, began to invest heavily in unmanned systems. As this development coincided with technical advances such as the development of GPS (Global Positioning System) and better data-storing and camera techniques, interest in drones began to take off. Particularly in the last decade, drones have become a must-have item for armed forces around the world. Today, 76 countries are known or suspected to have military drones at their disposal. Drones have firmly established their place in modern military operations.

From early 2000, a combination of factors led to the rise of drones for recreational and commercial use. Low-cost GPS and navigation boards, improvement and diffusion of low-cost open source microcontrollers and platforms made construction of home-made drones possible also to very small companies and led to their widespread use in the world. In fact, in 2007 Chris Anderson, founded DIYDrones.com [36], the largest community for amateur UAV. This community is the home of ArduPilot [7] (now known as APM (ArduPilotMega)), the world's first universal autopilot platform (planes, multicopters of all sorts and ground rovers). Today the Pixhawk [135] autopilot runs a variety of powerful free and open UAV software systems from the Dronecode Foundation [35], a collaborative project that brings together existing and future open source drone projects under a non-profit structure governed by the Linux Foundation [78].

Some of the currently proposed civil and commercial applications of UAS include:

- Security awareness;
- Disaster response, including search and support to rescuers;
- Communications and broadcast, including news/sporting event coverage;
- Cargo transport;
- Spectral and thermal analysis;
- Critical infrastructure monitoring, including power facilities, ports, and pipelines;
- Commercial photography, aerial mapping and charting, and advertising.

The market is booming and the Chinese DJI company has now inaugurated on December 2015 its first drone megastore with 800 m^2 of area.

Lots and lots of start-ups arise for designing, managing and making use of drones by inventing tools, software, app for mobile phones or by patenting new hardware for drones. Open Communities dedicated to drones were born and leader companies such as Google, Microsoft, Apple, Sony, employ their own research units to be at the forefront of drone development.

Most analyses indicate a growth of the drone civil market with an increase of its share compared to the military market. However, the military market will remain largely predominant by value. Market development is dependent on two main elements:

a. the implementation of a regulatory framework that will allow for safe, secure and environmentally friendly drone operations while at the same time addressing the citizens' concerns about privacy and data protection;
b. adoption of technologies mature enough to ensure full integration in non-segregated airspace;

Today, drones are essentially used for the so-called aerial work in manned aviation. However, several companies and institutions are looking at UAS for transportation of goods. A first case was the transportation of medications in disaster areas where access through roads was not possible [32]. Flight trials have already been conducted in Germany by DHL company, for the delivery of goods in remote areas of the countries (e.g. islands, mountains) There is currently serious work under way to be able to deliver goods in urban environments — an operation which will pose significant challenges (e.g. traffic management between drones of the same or other companies). Apart from delivering goods, a soldier was evacuated recently using an unmanned rotorcraft, a case that could be the first step towards transportation of persons[1].

Other trends could be miniaturisation following the general development of electronics; continuous development of autonomous drones; swarms of drones cooperating to ensure a mission.

2.3. UAS Definition

An unmanned aircraft system is composed of the drone (the flying component), a command and control station, a data link, and any other components necessary for operations (e.g. a take-off ramp).

There are two main groups of drones: those that are remotely piloted and those that are autonomous. An autonomous drone does not need pilot intervention in the management of the flight; however, drones for non-military use can be switched from autonomous to pilot at any time. The description proposed above covers a

[1]http://www.military.com/daily-news/2015/05/28/firms-demonstrate-casualty-evacuation-with-unmanned-helicopter.html

wide range of aircraft (fixed-wing rotorcraft, tilt rotor, etc.), control links (Wi-Fi, VHF, etc.), and control stations (iPad).

According to the EURO UVS International (European Unmanned Vehicle Systems Association) (a non-profit association that federates 22 national association for promotion of non-military use of drones), a UAV is a generic aircraft designed to operate with no human pilot on-board. The term UAV is used commonly in the Geomatics community, but also terms like Remotely Piloted Vehicle (RPV), Remotely Piloted Aircraft System (RPAS), Remotely Operated Aircraft (ROA), Remote Controlled (RC) Helicopter, Unmanned Vehicle Systems (UVS) and Model Helicopter are often used.

2.4. UAS Classification

Based on size, weight, endurance, range and flying altitude, UVS International defines three main categories of UAVs:

- *Tactical UAVs* which include micro, mini, close-, short-, medium-range, medium-range endurance, low altitude deep penetration, low altitude long endurance, medium altitude long endurance systems. The mass ranges from few kilograms up to 1000 kg, the range from few kilometres up to 500 km, the flight altitude from few hundred meters to 5 km, and the endurance from some minutes to 2-3 days.
- *Strategic UAVs*, including high altitude long endurance, which fly higher than 15000 m altitude.
- *Special tasks UAVs* like unmanned combat autonomous vehicles, lethal decoys systems, stratospheric and exo-stratospheric systems and have an endurance of 2-4 days.

The primary airframe types are fixed and rotary wings while the most common launch/take-off methods are, beside the autonomous mode, air-, hand-, car/track-, canister-, bungee cord launched.

Recent mini-UAVs have reached a state of development that allows the operator to navigate primarily in three distinct flight modes [39]:

- *Manual flight mode*. All degrees of freedom are controlled remotely by a human operator, directly and freely. The system follows the commands received from the pilot's remote control and no automation is involved. The pilot or a second operator observes the system status, such as fuel, batteries, radio link and so on, from the ground station.
- *Semi-automated or assisted flight mode*. The pilot or the operator can control the UAV through commands (vertical, lateral, longitudinal velocity

and heading). Assisted mode simplifies the UAV handling, since the UAV system is stabilized and the pilot and the operator only need to take care of the position based on the GNSS (Global Navigation Satellite Systems) and do not have to compensate for influences such as the wind.

– *Autonomous flight mode*. The pilot leaves the position and attitude control fully to the on-board navigation unit, which follows a predefined flight path. System parameters again can always be checked at the ground control station (GCS), while the UAV is stabilized. This mode is the most useful for conventional photogrammetric flights as it allows for efficient and accurate navigation to the image acquisition locations.

As far as tactical micro UAS are concerned, there are two main categories: rotary-wing and fixed-wing rotary aircraft. Both have advantages and limitations that render them more or less appropriate for determinate applications (in Table 2.2 are shown the major features of drones).

Table 2.4.1 – UAV Classification.

Name	Payload [kg]	Range [Km]	Flight altitude [m]	Endurance [h]
Tactical UAV				
Nano	< 0.0025	< 1	100	< 1
Micro	< 5	< 10	< 250	1
Mini	< 30	< 10	150 – 300*	< 2
Close Range (CR)	150	10 –30	3000	2 – 4
Short Range (SR)	200	30 – 70	3000	3 – 6
Medium Range (MR)	150	70 - 200	3000 – 5000	6 – 10
MR Endurance (MRE)	500	> 500	5000 – 8000	10 – 18
Low Altitude Long Endurance (LALE)	< 30	> 500	3000	> 24
Medium Altitude Long Endurance (MALE)	1000 – 1500	> 500	5000 – 8000	24 – 48
Strategic UAV				
High Altitude Long Endurance (HALE)	2500 – 12500	> 2000	15000 – 20000	24 – 48
Special Task UAV				
Unmanned Combat Aerial Vehicle (UCAV)	10000	+/- 1500	+/-10000	+/-2
Lethal (LETH)	250	300	3000 – 4000	3 – 4
Decoys (DEC)	250	0 – 500	50 – 5000	> 4
Stratospheric (Strato)	-	> 2000	20000 – 30000	> 48
*according to national legal restrictions				

Fixed wings aircraft allow flying at high altitude and for long duration. Having a very low weight and packed size, Regulations consider “safe” these platforms in *uncritical* operations (see for example ENAC Regulations for UAS with MTOM ≤ 2 kg in Paragraph 2.7.2. – Section II). Thus, fixed-wing are suitable for mapping wide areas. On the contrary, these UAS have the disadvantage of requiring a runway or a launcher to take off and landing and are unable to hover. Furthermore, fixed-wing are typically marketed as full package with sensors and flight control system (camera, software and ground station) in fixed configurations. Thus, they are user-friendly and easy to operate, but customizations and changes are generally not permitted.

In contrast, rotary-wing platforms have a greater mechanical and dynamic complexity, lower speed, lower altitudes and shorter flight ranges. Manual piloting is not trivial and requires a long training. The main advantages are the ability to Vertical Take-Off and Landing (VTOL), to hovering on a fixed point and also to fly in any direction (vertical, horizontal). Due to the mechanical frame characteristics and less stringent requirements on aerodynamics (though not on flight dynamics) payload customization is generally possible; in fact, a wider range of sensors can be employed and assembled as required. Rotary-wing drones are ideal for inspection and surveys in confined environments, vertical walls, bridge inspections, etc. since the camera can rotate both vertically (0-90° in Zenith) and horizontally (0-360° in Azimuth), unlike fixed-wing systems.

Table 2.4.2 – Major features of fixed-wing versus rotary-wing platform.

Fixed-wing versus Rotary-wing Features		
	Fixed-wing	**Rotary-wing**
Low Weight	+ +	– –
Max Flight Altitude	+ + +	– –
Endurance	+ + +	– – –
Areal coverage per mission	+ + +	– – –
Flight Speed	+ + +	+
Vertical Take-Off and Landing	– – –	+ + +
Nadiral Imaging	+	+
Oblique Imaging	– – –	+
3D Gimbal	– – –	+
Horizontal Imaging	–	+
Ability to Fly Vertical Flight Lines	– – –	+ + +
Ability to Fly Horizontal Flight Lines	+ + +	+ + +
Sensing Payload Customization	– – –	+ + +

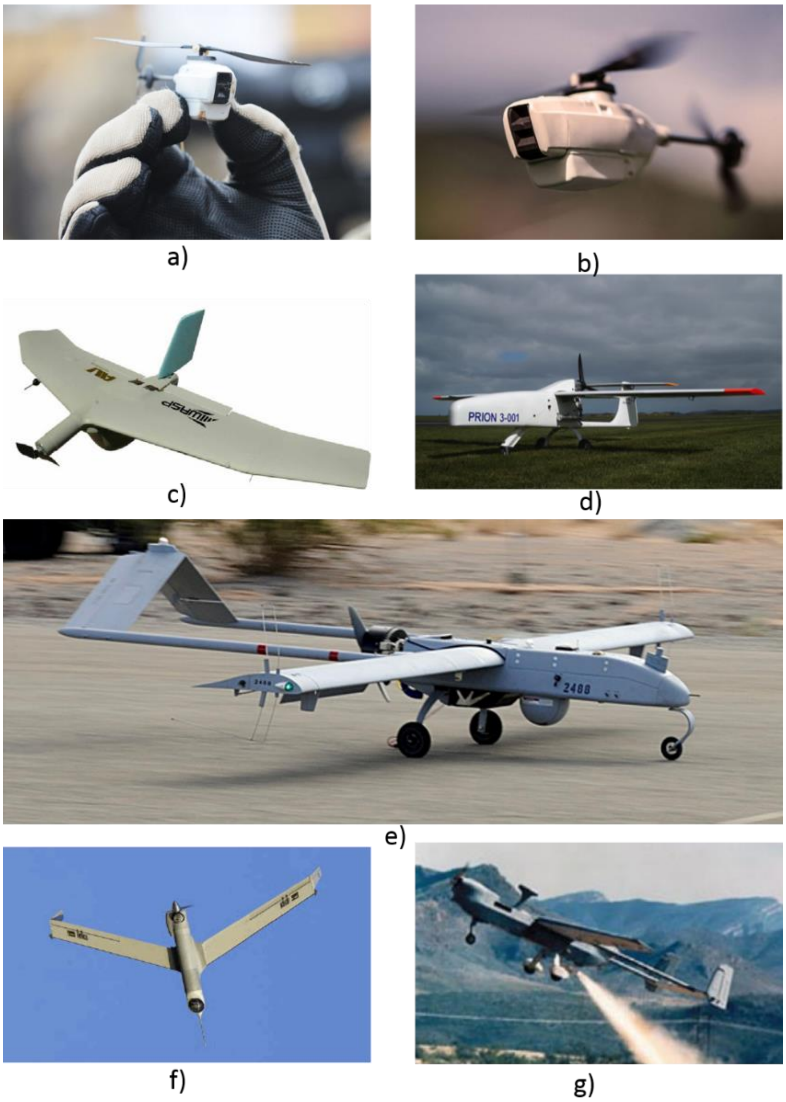

Fig 2.1.2 – continued.

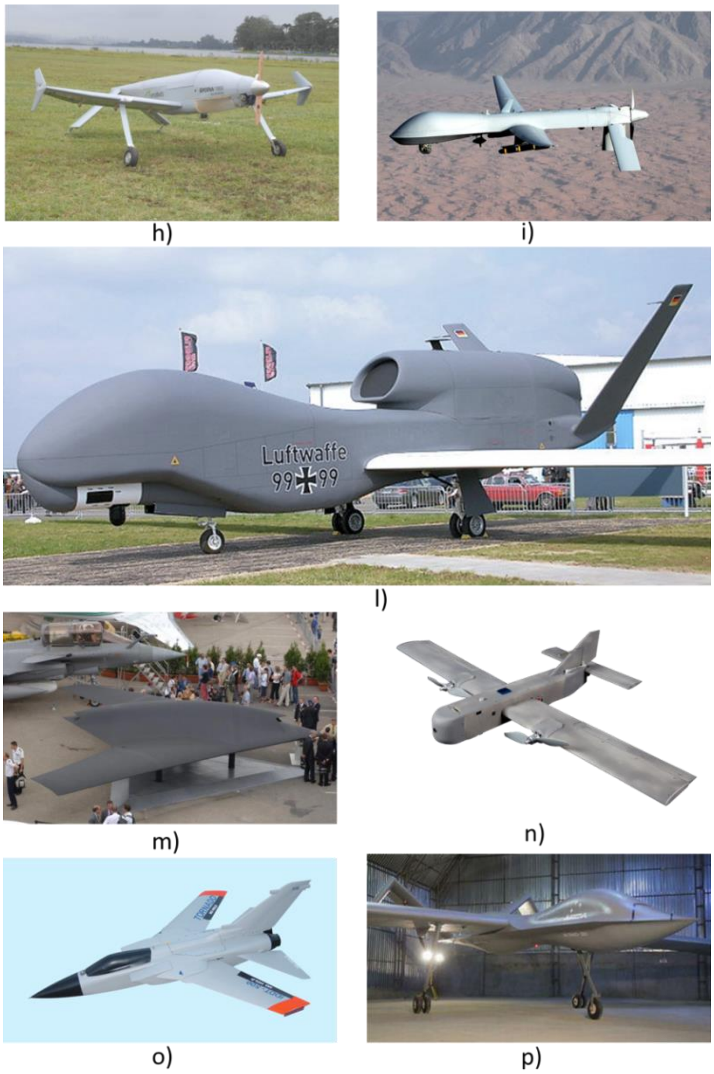

Figure 2.4.1 – Examples of UAS categories in the world. In bold UAV classification, in italic model name in the market: a) NANO: Black Hornet by Prox Dinamics (Norway). b) MICRO: PD-100 BLACK HORNET by Prox Dynamics (Norway). c) MINI: WASP III by AeroVironment (USA). d) CR: Prion Odin aero by UAS norway (Norway). e) SR: RQ-7 Shadow by AAI corporation (USA). f) LE: Scaneagle by Insitu (USA). g) MRE: RQ-5 Hunter by Israel Aircraft Industries (Israel). h) LALE: Apoena 1000 by Xmobots (Brazil). i) MALE: MQ-1 Predator by General Atomics (USA). l) HALE: RQ-4A Global Hawk by Northrop Grumman Corporation (USA). m) UCAV: nEUROn by Dassolt Aviation (France). n) ***LETH****: Terminator by AeroVironment Inc (USA). o)* ***DEC****: Tornado by Integrated Dynamics (Pakistan). p)* ***STRATO****: AirStrato by ARCA (Romania).*

2.5. Pros & Cons with respect to manned aircrafts

Drones, compared to traditional manned aircrafts, have advantages and disadvantages. Their distinctiveness, of having no pilot on board, certainly makes them less expensive in terms of construction and running costs (pilot salary, fuel consumption, maintenance). In fact, the drones are born in the civil sector as a cheaper alternative to traditional platforms, especially for inspections of damaged, disaster-hit or sensitive areas (i.e. earthquake post-scenario) that are dangerous for humans. Moreover, UAS can fly where manned aircraft are not allowed or do not have the capability to fly, e.g. at low altitude and at flight lines close to the objects, obtaining very high-resolution imagery. Their mission can be programmed and remotely controlled with minimum human operator intervention; real-time data transmission to the ground control station can be foreseen (though is not always necessary).

On the other hand, development of collision avoidance systems and other artificial intelligence software and hardware tools for safe operation of UAS in the so-called critical environment are far from widespread. Authorities in charge of airspace regulations are working to address these topics (see Paragraph 2.7 where European and Italian Regulations of UAS will be discussed). As of today, most drones, in front of a sudden obstacle, would not change automatically the route, as would a pilot aircraft. However, collision avoidance is now a research topic and there is no reason to think that, as for automatic car driving, the problem will be solved. For instance, one such system for drone safe flight operation, devised at MIT, is being tested on a fixed wing UAS [15]. The identification in real time of obstacles is performed through stereoscopic vision provided by two cameras located on the wings. In particular, the software allows extrapolating information from the camera recording at 120 frames per second. The drone saves these pixels in memory, and the next image (taken 8.3 cm later if the drone is flying at 10 meters per second) adds more pixels beyond the previous set. In this way, the drone can very efficiently build up a 3D map of what is directly in front of it, and take action based on that map. This technique is called “push broom stereo detection,” because the detection area is like a three-dimensional broom that is being pushed forward.

Other issues are related to communication links (long range, sufficient bandwidth, out of line-of-sight capability). In fact, both low quality connectivity of radio-signal and a wrong manoeuvring in the attempt to manually control contribute to control the drone badly. Investing resources on better data-link is necessary for safety, integrity and accomplishment of survey, in addition to a training to become an experienced pilot.

Basically, the main limit for civil applications of micro-mini UAV is the payload allowed, in weight as well as in size. This means that in most cases only a sensor at a time can be installed and that digital compact cameras are often chosen. The better sensors and optics of SLR (single lens reflex) or mirrorless cameras would provide a better image quality and resolution. A higher number of images must therefore be acquired to cover the same area at the same resolution, with implications on image storage capacity on board and a more demanding in-office data processing.

Trembling caused by external factors like wind also compromise the image quality. In particular, electro motors UAS are more susceptible to external factors since they are lightweight; on the contrary, drones powered by fuel are heavier and more stable. However, even if they allow for larger payloads, getting rid of the vibrations from the engine is tricky and expensive and the advantage of a better sensor might be lost. Indeed virtually all UAS for photogrammetric and environmental applications use today electric motors.

Another issue regards navigation sensors and systems. Due to limitation on payload, they are often chosen according to (low-cost and) low-weight standard. Being less accurate, they allow autonomous navigation but not (yet) direct georeferencing of images. However, even the relatively low accuracy direct orientation observations can improve the absolute georeferencing accuracy as reported in the simulation study in [108]; with high quality GNSS or GNSS/IMU (Inertial Measurement Unit) data, in theory, there is no need for GCPs at all.

2.6. UAS platforms

In this paragraph, the UAS platforms employed in the current work will be presented. In particular three rotary-wing and two fixed-wing aircrafts are described with their technical features. These drones belong to different partners (universities, photogrammetric companies, professionals, etc.) that were not only instrumental to this research (our Department currently does not own drones) but first and foremost made invaluable contributions through the exchange of technical expertise and know-how. In fact, these partners come from different background and, pursuing different goals, contributed to build a more comprehensive picture of UAV photogrammetry. Likewise, the drones used in the collaborations present a rather comprehensive panorama of the available models, the most suitable for the applications.

2.6.1. HexaKopter

The HexaKopter, (http://wiki.mikrokopter.de/HexaKopter) built by the German company MikroKopter, belongs to the Geodesy and Geomatics Section, – Department of Civil and Environmental Engineering (DICA), of the Polytechnic of Milan. The research group performs UAS surveys for remote sensing and mapping purposes: tree species classification, 3D modelling, generation of digital surface models and digital terrain models as well as of precise orthophotos. With such variety of products, it is important to have an open system, flexible enough to accommodate different sensors so that customization is possible. Being also the first UAV bought by the Department, ease of operation and low-cost were additional requirements, all met by the HexaKopter, shown in Figure 2.6.1. It is an off-the-shelf model costing only a few k€, including the commercial kit and the assembly which was carried out by the Italian company RestArt (2012).

Figure 2.6.1 –The HexaKopter with the Control Station.

This VTOL aircraft is equipped with six brushless motors with 25.4 cm long propellers; it weighs about 1.2 kg with batteries, whereas the maximum transportable payload is 0.5 kg. The HexaKopter can fly up to 200 m away from the take-off point and the flight duration is limited to 10 minutes (enough to acquire an area of roughly 100 × 70 m). The power supply is assured by two Lithium 4000 mAh batteries.

The complete equipment comprehends some control boards and navigation sensors, listed below:

- Six brushless control boards, which regulate the rotation speed of the motors;
- A Flight Control board to receive operator command via remote control and to interpret them for the flight execution;

- A remote control to pilot the aircraft (flight height, hovering on a specific point, “return home” function, navigation trough waypoints).
- A Navi Control board to execute the above mentioned commands.
- A GNSS receiver with a single frequency antenna ublox LEA-4H. The positional information is transmitted to the Navi control by a serial link.
- Two XBee Pro 2 modules to establish a bi-directional wireless connectivity between the Navi Control board and the Ground Control Station. This link is required to manage the operations during the flight and its nominal range is equal to 1 km in open-space.

The GCS is composed by a laptop with a MikroKopter software tool that manages all component settings: waypoints definition and transmission to the HexaKopter, system checks during flight operations and verification of the received telemetry data.

Table 2.6.1 – Technical specifications of HexaKopter.

HexaKopter technical specifications	
Weight	1.2 kg
Weight at Take-off	2.7 k
Payload capacity	0.5 kg
Endurance	10 min
Max flight radius.	200 m
Max flight altitude above ground	150 m
Material	Aluminium booms/ rigger and milled centre plates

2.6.2. EASYFLY

Figure 2.6.2 – EASYFLY by Eurodrone: this hexacopter has been used for the survey of Veleia Romana archeological site.

Easyfly [37] by the Italian company Eurodrone is a multi-rotor wing (see Figure 2.6.2). It has an endurance of about 15 minutes depending on the type of payload. It can fly up to an altitude of 3000 meters (a.s.l.) with a payload up to 1 kg. It is equipped with six brushless motors powered by two Lithium batteries by 4000 mAh.

It can execute a mission fully automatic (take-off, flight execution according to plan, and landing) thanks to the radio link between the autopilot on the drone and the ground control station. The navigation system is based on Ublox GPS receiver for the position and a navigation control that memorize and uses these data for flight operation.

Table 2.6.2 – Technical specifications of UAS EASYFLY.

EASYFLY technical specifications	
Weight	3 kg
Weight at Take-off	2.9 kg
Payload capacity	1.2 kg
Endurance	15 min
Nominal cruise speed	1-5 m/s
Wind resistance	< 25 km/h
Maximum area coverage (single flight)	1 km^2
Max. Take off elevation	3300 m above sea level
Max. flight altitude above ground	500 m
Flight range (line of sight)	1500 m
Material	Aluminium frame and Kevlar calotte

2.6.3. Falcon 8

The collaboration with the photogrammetric company STAF, interested in the potential of UAS for urban map updating, has given opportunity to employ the AscTec Falcon 8 produced by the German company Ascending Technologies, (http://www.asctec.de/uav-uas-drohnen-flugsysteme/asctec-falcon-8/) shown in Figure 2.6.3.

The Falcon 8 is suitable to perform surveys for urban map updates for its flight duration, its VTOL ability (typical of a rotary-wing) and its higher manoeuvrability thanks to an adaptive flight control system.

It is a V-shaped Octocopter, equipped with eight electrical brushless motors and 20 cm long propellers; it weighs about 1.1 kg without batteries, whereas the maximum transportable payload is 0.8 kg. The Falcon 8 can fly up to 200 m far from the take-off point and the flight duration varies between 12 to 22 minutes (according the flight mode chosen). The power supply is assured by two Lithium 6250 mAh batteries.

Three flight modes are foreseen: GPS mode, Height Mode or Manual Mode; switch between modes during a flight is permitted.

Figure 2.6.3 – Falcon 8 drone.

The complete equipment comprehends control boards and navigation sensors, listed below:

- Eight brushless control boards, which regulate the rotation speed of the motors (12-15 m/s);
- A Flight Control board to receive operator command via remote control and to interpret them for the flight execution;
- A remote control to pilot the aircraft (flight height, hovering on a specific point, “return home” function, navigation trough waypoints, navigation along a Circle-Of-Interest – that generates waypoints on a circle to enable the systematic capturing of images around the point of interest.
- A Navi Control board to execute the above mentioned commands.
- Three IMU.
- A video receiver used to receive video signal from the drone at 5.8 Ghz.

The Mobile Ground Station consists of a Remote Control via a Diversity data-link. The Futuba FX-22 remote control is only used as a control input device. The GS manages all components settings: it defines waypoints, transmits them to the Falcon 8, checks the system during flight operations and verifies the received telemetry.

Table 2.6.3 – Technical specifications of UAS Falcon 8.

Falcon 8 technical specifications	
Weight	1.1 kg
Weight at Take-off	2.3 kg
Payload capacity	0.8 kg
Endurance	12- 22 min
Nominal cruise speed	16 m/s
Wind resistance	< 15 m/s
Maximum coverage	0.035 km^2
Radio link range	< 1km
Max. Take off elevation	4500 m above sea level
Max. flight altitude above ground	1000 m above ground level
Material	carbon structure & composite parts

2.6.4. SwingletCAM

The Climate Change Unit of ARPAVdA (Agenzia Regionale per la Protezione dell'Ambiente, Regione Autonoma Valle d'Aosta - Environmental Protection Agency of Valle d'Aosta) is another partner. This operative unit studies the impact of climate change on high-mountain infrastructures monitoring several sites. Extreme environments, such as high mountain areas, are difficult and sometimes dangerous places for survey operations. Therefore, the use of a drone represents an easy and safe way to conduct the monitoring activities. In this particular context, UAS have to be effortlessly transportable and to be able to fly at high altitude over an extended area in a short time, to quickly exploit every chance the wind allows for a safe flight. Assuring endurance, low power consumption and safety of operation in case of sudden weather changes is necessary. Thus, the Agency bought the lightweight drone “SwingletCAM” by SenseFly [117].

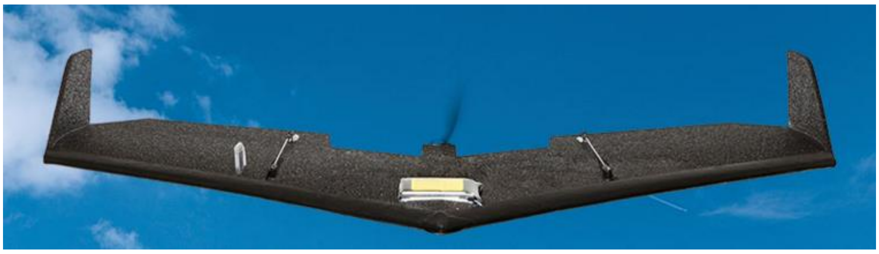

Figure 2.6.4 – SwingletCAM by SenseFly: fixed-wing in expanded polypropylene foam and carbon structure. It has been used for the survey of Gran Sommetta rock glacier.

The Swinglet is a very lightweight UAV, weighting less than 500 g including an Ublox GPS chip, an attitude sensor, a radio transmitter and an autopilot circuit board (Figure 2.6.4). The maximum payload is 125 g. An autopilot drives the UAV automatically on the flight lines and triggers the camera. The camera setup for data acquisition manages automatically the autofocus and the speed-aperture settings. To protect the camera during take-off and landing, the camera is shutdown. The latest firmware provides a more flexible trigger function accounting for the flight height above ground, ground velocity and expected overlap.

Power supply is assured by a small Lithium-Ion battery that provides a flight autonomy of about 30 min. The Swinglet can operate only in low wind (less than 25 km/h).

The full SwingletCAM package also includes the eMotion ground station software that is a tool for flight planning and system control. It allows planning and simulating a flight; furthermore, it allows monitoring in real time the launched drone, in order to check flight parameters, battery level and image acquisition progress. The software tools of the GCS provide for a safe return of the drone to the landing site (take-off point or Home point) if something goes wrong (e.g. loss of radio signal, low battery level, etc.).

Customization is very restricted to specific Canon digital cameras of the Ixus series. In the surveys of the Gran Sommetta glacier a 12 Mpixel 120 IS, a 12 Mpixel 220 HS and a 16 Mpixel 125HS were used with a pixel size of 1.54 μm. The focal length varies from 5 mm to 20 mm.

Table 2.6.4 – Technical specifications of UAS SwingletCAM.

SwingletCAM technical specifications	
Weight	0.50 kg
Weight at Take-off	0.55 kg
Payload capacity	0.0125 kg
Flight duration	30 min
Nominal cruise speed	36 km/h
Wind resistance	< 25 km/h
Maximum area coverage (single flight)	6 km^2
Radio link range	< 1km
Max take off elevation	4000 m above sea level
Ceiling	5200 m above sea level
Material	EPP foam, carbon structure & composite parts

2.6.5. eBee

The Climate Change Unit of ARPAVdA is considering the purchase of a drone equipped with RTK GPS (real time kinematic-GPS) to monitor the high-mountain sites. Upon the good experiences with the SwingletCAM, considering it is discontinued product, the lightweight “eBee RTK” by SenseFly [38] has been rent for an experimental survey over the Gran Sommetta rock glacier (see Section 5.3).

Figure 2.6.5 – eBee RTK by SenseFly: fixed-wing in expanded polypropylene foam and carbon structure. It has been used for the survey of Gran Sommetta rock glacier.

The eBee RTK is a very lightweight UAV, weighting less than 700 g including a double frequency RTK receiver, an attitude sensor, a radio transmitter and an autopilot circuit board (Figure 2.6.5). The maximum payload is 125g. An autopilot drives the UAV automatically on the flight lines and triggers the camera. The camera setup for data acquisition manages automatically the autofocus and the speed-aperture settings. To protect the camera during take-off and landing, the camera is shutdown. The latest firmware provides a more flexible trigger function accounting for the flight height above ground, ground velocity and expected overlap.

It is has more endurance than the SwingleCAM, in fact the battery power has been increased, providing a flight autonomy of about 40 min over a 8km^{2}area. The eBee can operate also in moderate-to-strong wind (up to 45 km/h).

The full eBee package, as for the SwingletCAM, also includes the eMotion ground station software that is a tool for flight planning and system control. It allows planning and simulating a flight; furthermore, it allows monitoring in real time the launched drone, in order to check flight parameters, battery level and image acquisition progress. The software tools of the GCS provide for a safe return of the drone to the landing site (take-off point or Home point) if something goes wrong (e.g. loss of radio signal, low battery level, etc.).

The eBee is equipped with an 18.2 Mpixel SONY WX digital compact camera with a pixel size of 1.22 micrometres and focal length of 4.5 mm.

Table 2.6.5 – Technical specifications of UAS eBee.

eBee technical specifications	
Weight	0.70 kg
Weight at Take-off	0.73 kg
Payload capacity	0.0125 kg
Flight duration	40 min
Nominal cruise speed	40-90 km/h
Wind resistance	< 45 km/h
Maximum area coverage (single flight)	8 km^2
Radio link range	< 3 km
Max take off elevation	4000 m above sea level
Ceiling	5200 m above sea level
Material	EPP foam, carbon structure & composite parts

2.7. UAS Policy Framework

The development of Unmanned Aircraft Systems has opened a promising new chapter in the history of aeronautics.

Unmanned Aircrafts can offer a wide range of possibilities for the benefit of society, ranging from environmental control, security, as well as a fascinating variety of commercial services. UAS can perform air operations that manned aviation can hardly do, with cost savings and environmental benefits while reducing the risk to human life.

However, the absence of a clear EU regulatory framework limits the possibility to fly UAS in non-segregated airspace. It is a potentially quite severe limitation for the development of UAS market, which requires a careful balance between safety concerns and economic development. Policy should not therefore be left only to the airspace regulation authorities.

2.7.1. EASA

To ensure a safe, secure and environmentally friendly development, and to respect the citizens legitimate concerns for privacy and data protection, European Aviation Safety Agency (EASA) has been charged by the European Commission (EC), following the Riga Conference and its associated Declaration[2], to develop a regulatory framework for drone operations as well as concrete proposals for the regulation of low-risk drone operations.

The draft text is the Advance Notice of Proposed Amendment (A-NPA) 2015-10 of 31 July 2015, in line with Regulation (EC) Nº 216/2008. It has been developed by EASA based on the inputs of the Joint Authorities for Regulation of Unmanned Systems (JARUS), and numerous meetings and workshops with the EASA Member States (MSs), drone industry and operators as well as "manned aviation" stakeholders.

This regulatory framework follows a risk- and performance-based approach; it is progressive- and operation-centric. It presents several terms such as Unmanned Aircraft Systems (UAS), Remotely Piloted Aircraft Systems (RPAS) (an UAS subcategory), but finally followed the general usage of the term 'drone' with the following definition: "Drone shall mean an aircraft without a human pilot on board, whose flight is controlled either autonomously or under the remote control of a pilot on the ground or in another vehicle".

This definition has significant consequences. It encompasses the two main groups of command and control systems, thus addressing the fast-growing development of drones operating autonomously. By defining only the drone (the flying part), it allows to treat regulatory-wise the drone separately from the command and control station, thus providing flexibility. Consequently, rules need to address both the drone and the associated parts not attached to it.

It introduces three categories of operations as already proposed in the published EASA Concept of Operations for Drones[3]:

- "Open" category (low risk): safety is ensured through operational limitations, compliance with industry standards, requirements on certain functionalities, and a minimum set of operational rules. Enforcement shall be ensured by the police.
- "Specific operation" category (medium risk): authorisation by National Aviation Authorities (NAAs), possibly assisted by a Qualified Entity

[2] http://ec.europa.eu/transport/modes/air/news/doc/2015-03-06-drones/2015-03-06-riga-declaration-drones.pdf

[3] http://easa.europa.eu/system/files/dfu/204696_EASA_concept_drone_brochure_web.pdf

(QE) following a risk assessment performed by the operator. A manual of operations shall list the risk mitigation measures.

– "Certified" category (higher risk): requirements comparable to manned aviation requirements. Oversight by NAAs (issue of licences and approval of maintenance, operations, training, Air Traffic Management (ATM)/Air Navigation Services (ANS) and aerodrome organisations) and by EASA (design and approval of foreign organisations).

Low-risk operations – "open" category

The '*open*' category operation is low-risk and simple-drone operation, where the risk to third parties on the ground and to other airspace users is mitigated through operational limitations. 'Open' category operation is any operation with small drones under direct visual line of sight with a Maximum Take-Off Mass (MTOM) of less than 25 kg operated within safe distance from persons on the ground and separated from other airspace users. No certification, approval, license or other equivalent document is required in relation to the operation of drones, except in the case of more complex, low-risk operations where adequate knowledge and skills need to be demonstrated.

To prevent unintended flight outside safe areas and to increase compliance to applicable regulations, it is proposed to mandate geofencing and identification for certain drones and operation areas. Geofencing means automatic limitation of the airspace a drone can enter, while identification means the capability to react on interrogations from enforcement entities and provide information about the drone, the operator and the operation. Standards for identification and geofencing functions will be endorsed by the Agency and could be referenced in the market regulations system in order to ensure that the majority of consumer products comply with these standards and to ensure harmonisation at technical level. This will enable manufacturers to develop adequate equipment and to declare compliance with these standards.

To ensure safety, environmental protection, and security and privacy, the competent authorities can define 'no-drone zones' where no operation is allowed without authority approval, and 'limited-drone zones' where drones must provide a function to enable easy identification and automatic limitation of the airspace they can enter and should have a limited mass.

All drone operations in the "open" category must be conducted within the defined limitations:

– Only flights in direct visual line of sight of the pilot are allowed.
– Only drones with a maximum take-off mass below 25 kg are allowed.

- No operation of drones in ‘no-drone zones’ is permitted.
- Drones operating in ‘limited-drone zones’ must comply with the applicable limitations.
- The pilot is responsible for the safe separation from any other airspace user(s) and shall give right of way to any other airspace user(s).
- A drone in the ‘open’ category shall not operate at an altitude exceeding 150 m above the ground or water.
- The pilot is responsible for the safe operation and safe distance from uninvolved persons and property on the ground and from other airspace users and shall never fly the drone above crowds (> 12 persons).

For any drone operations over 50 m above ground, with a higher risk of conflict with manned aviation, basic aviation awareness shall be required for the pilot.

Three subcategories for the ‘open’ category are established to allow for a more flexible adaption to the risk and are: 1) CAT A0: ‘Toys’ and ‘mini drones’ < 1 kg; 2) CAT A1: ‘Very small drones’ < 4 kg; 3) CAT A2: ‘Small drones’ < 25 kg.

1) Additional requirements for CAT A0 are that operation shall be performed below 50 m above ground. Furthermore, any drone sold as a toy or consumer product with a mass below 1 kg could comply with the applicable product safety Directive and shall have limited performance to assure flight below 50 m above ground and local operation or alternatively the means to automatically limit the altitude and the airspace they can enter.
2) Additional requirements for CAT A1: any drone sold as a consumer product, which is heavier than 1 kg, could comply with the applicable general product safety Directive and shall have the means to automatically limit the airspace it can enter and the means to allow automatic identification. Drones operating in the ‘limited-drone zones’ shall have active identification and up-to-date geofencing capability enabled. For any operation over 50 m above ground, the pilot needs to have basic aviation awareness. Any failures, malfunctions, defects or other occurrences that lead to severe injuries to or fatalities of any person need to be reported.
3) Additional requirements for CAT A2: any drone sold as a consumer product, which is heavier than 4 kg, could comply with the applicable general product safety Directive and shall have the means to automatically limit the airspace it can enter and the means to allow automatic identification. Operation in the ‘limited-drone zones’ is not permitted in the ‘open’ category for drones with a take-off mass above 4 kg. For any

operation over 50 m above ground, the pilot needs to have basic aviation awareness. Any failures, malfunctions, defects or other occurrences that lead to severe injuries to or fatalities of any person need to be reported to the Agency.

Tethered aircraft up to a mass of 25 kg or a defined volume for aircraft lighter than air can be operated in the 'open' category outside 'no-drone zones' below 50 m above ground or water, or in dedicated areas notified to other airspace users.

Specific risk operation – "specific" category

"Specific risk operation" is any operation with drones which poses more significant aviation risks to persons overflown or which involves sharing the airspace with manned aviation. Each specific aviation risk needs to be analysed and mitigated through a safety risk assessment. In the 'specific' category we could expect operations of drones out of the visual line of sight of the pilot, sharing airspace with other users where separation assurance with respect to other aircraft cannot be performed by the pilot and this function relies on the safety equipment installed on the drone (i.e. the 'detect and avoid' function), or on specific operational procedures. Operations with large drones but also with small drones above densely populated areas, like city centres, could also fall in the 'specific' category.

The operator taking into account all the elements that contribute to the risk of the particular operation shall perform a safety risk assessment. For this purpose, the operator shall:

- provide to the competent NAA all the information required for a preliminary applicability check of the category of operation;
- provide to the competent authority a safety risk assessment covering both the drone and the operation, identifying all the risks related to the specific operation, and proposing adequate risk-mitigation measures.
- compile an appropriate Operations Manual containing all the required information, descriptions, conditions and limitations for the operation, including training and qualification for personnel, maintenance of the drone and its systems, as well as occurrence reporting and oversight of suppliers.

The competent authority of the State of the operator shall be responsible to issue the Operation Authorization (OA) after the review and agreement with the safety risk assessment of operator and the Operations Manual in the "specific" category.

The operation shall be performed according to the limitations and conditions defined in the OA:

- The operator shall not carry out specific operations, unless holding a valid operation authorisation.
- The operator shall ensure that all involved personnel is sufficiently qualified and familiar with the relevant operation procedures and conditions.
- Before the initiation of any operation, the operator is responsible to collect the required information on permanent and temporarily limitations and conditions and to comply with any requirement or limitation defined by the competent authority or to request specific authorisation.

The operation in the “specific” category might be performed with drones or equipment that is certified or otherwise approved. The operation might exceed the operational limitations for the certified equipment when specifically authorised and when the operation ensures application of adequate risk mitigations as identified in the OA. Equipment, parts and functionalities might be approved independently from the drone itself and an approval may be granted. The IRs will define the required processes based on the ‘European Technical Standard Order (ETSO)’ process. The process for release and continuing airworthiness oversight needs to be adapted as equipment might not be installed on certified drones. This might cover ground stations or qualified ‘detect and avoid equipment’ installed on drones in the ‘specific’ category.

Operators may voluntarily make use of suppliers or personnel holding certificates or voluntarily apply for a Remote Operator Certificate (ROC) detailing the means on how responsibilities are shared and having adequate privileges to authorise operations.

Higher-risk operation – “certified” category”

Certification will be required for operations with an associated higher risk due to the kind of operation, or might be requested on a voluntary basis by organisations providing services (such as remote piloting) or equipment (such as detect and avoid). When unmanned aviation risks rise to a level similar to normal, manned aviation, the operation would be placed in the “certified” category of operations. These operations and the drones involved therein would be treated in the classic aviation manner: multiple certificates would be issued (as for manned aviation) plus some more certificates specific to drones.

In order to operate a drone in the “certified” category, the airworthiness of the aircraft and its compliance with environmental standards shall be ensured in the same way as it is done today for manned aviation by issuing a TC (Type

Certificate) or Restricted Type Certificate (RTC) for the type, and a Certificate of Airworthiness (CofA) or restricted CofA for the particular drone.

The TC or RTC might cover the complete unmanned aircraft system including the drone and the components on the ground (like the control station), or may cover only the drone and its airborne systems. When only the drone is included in the TC or RTC, the limitations and conditions for the compatible ground control stations and command and control link including bandwidth, latency and reliability requirements will be established under the TC or RTC.

The pilot shall be licensed and the operator shall hold a ROC.

The TC or RTC might cover the complete unmanned aircraft system including the drone and the components on the ground (like the control station), or may cover only the drone and its airborne systems. When only the drone is included in the TC or RTC, the limitations and conditions for the compatible ground control stations and command and control link including bandwidth, latency and reliability requirements will be established under the TC or RTC.

2.7.2. ENAC

On July 2015, Italian Civil Aviation Authority (Ente Nazionale per l'Aviazione Civile – ENAC) approved the second version of Regulations[4] on unmanned aircraft vehicles.

The second draft of the Italian regulation has covered many elements indicated in the EU regulation.

The Regulation - in force since September 15, 2015 - has introduced some changes in particular to the use of unmanned aircraft under 25 kg. It has been issued in implementation of Code of Navigation 743 Article, which allows the identification of the competence of ENAC to set technical characteristics and limitations to the use of unmanned aircraft.

The regulations is composed of six sections and thirty-seven articles:

- Section I – General.
- Section II – Remotely Piloted Aircraft Systems with maximum take-off mass of less than 25 kg.
- Section III – Remotely Piloted Aircraft Systems with maximum take-off mass more than or equal to 25 kg.
- Section IV – Provisions for pilots of Remotely Piloted Aircraft.
- Section V – Traffic rules and use of airspace.

[4]http://www.enac.gov.it/repository/ContentManagement/information/N122671512/Reg_APR_Ed%202_2.pdf

– Section VI – General Provisions for Remotely Piloted Aircraft Systems.
– Section VII – Model Aircraft.
– Section VIII – Final Provisions.

Section I contains general definitions helpful to clarify some basic recurring concepts as UA and limits of applicability. Sections II and III list, according to the maximum take-off mass of the vehicle, the requirements to be complied with to operate the different categories of Remotely Piloted Aircraft Systems. Section IV provides rules for becoming a Remotely Piloted Aircraft pilot. Section V lists the operational rules applicable to the airspace concerned by the operations. Section VI provides common rules for the operation of all Remotely Piloted Aircraft Systems. Section VII provides the requirements to be complied with for the use of model aircraft. Final provisions in Section VIII.

The Regulation applies to the operations of Remotely Piloted Aircraft Systems pertaining to the competence of ENAC and to the activities of model aircraft for Remotely Piloted Aircraft Systems of maximum take-off mass not exceeding 150 kg and those designed or modified for research, experimental or scientific purposes are under ENAC responsibility.

Section I

The regulations contains in Section I definition of remotely piloted aircraft:

- *Remotely piloted aircraft (RPA)* is a remotely piloted aerial vehicle without persons on board, for use different from recreations and sports.
- *Remotely piloted aircraft System (RPAS)* is a system consisting in a RPA, not used for recreation and sports, and in the additional components necessary for control and command by a remote pilot.
- *Model aircraft* is a remotely piloted device, without people on board, used exclusively for recreational and sports purposes that does not feature any installed equipment enabling autonomous flight, and it is used under the direct and continuous visual control of the operator, without visual aids.

Furthermore, definitions of typical operations:

- *Beyond Line Of Sight (BLOS)* are operations conducted at a distance that do not allow the remote pilot to continuously remain in direct visual contact with the RPA, or to comply with the applicable rules of the concerned volume of the airspace.
- *Visual Line of Sight (VLOS)* indicates that the operations are carried out under conditions in which the remote pilot remains in visual direct contact with the aircraft, without the aid of optical and/or electronic

devices, to manage and comply with the rules of the air applicable to the concerned volume of the airspace.

- *Extended Visual Line Of Sight (EVLOS)* are operations performed exceeding the limits of the VLOS conditions, for which the direct visual contact with the RPA can be satisfied using alternative means.

This Section reports two classifications, in accordance with MTOM of RPA, in: a) systems with a vehicle of MTOM of less than 25 kg; b) systems with a vehicle of MTOM equal to or more than 25 kg and less than 150 kg.

Therefore, definitions of RPAS operations were provided as specialised operations as well experimental activities. *Specialised Operations* are service activities, whether remunerated or not, such as surveillance of land or installations, environmental monitoring, agricultural use, photogrammetric activities, advertising, etc.. *Noncritical Specialised Operations* are operations in VLOS not involving the over-flight of congested areas, gatherings of people, urban or critical infrastructure, even in the event of failures and malfunctions. *Critical Operations* are those that do not respect restrictions provided for noncritical operations.

Section II

In Section II, RPA with MTOM of less than 25 kg are covered. Regulation provides the requirements to be met to obtain the relevant authorizations to operate, defining the different methods of access to airspace, the permitted operations, and airworthiness certifications applicable, the conditions to carry out specialized operations and for obtaining Operator Certificate aerial work.

Regardless of weight, any RPAS must be equipped with identification instrument:

a) A plate showing identification data of the system and the operator. The plate must be also installed on the ground station (GS).
b) An electronic device enabling the transmission in real time and the registration of flight data, navigation data and operator data.
c) Any RPAS must be equipped with Flight Handbook.
d) Special system to signalize height of flight.
e) Lights to increase vehicle visibility in VLOS operations, in uncontrolled airspaces (where service traffic control is not provided).
f) High visibility jacket worn by remote pilot with specification of “RPA pilot”.

For RPA with MTOM of less than 25 kg uncritical and critical operations are permitted. Uncritical operations are permitted upon presentation to ENAC of appropriate declaration, whereas critical operations require prior authorization by

ENAC. Either way is not allowed to over flight congested areas, gatherings, urban areas and critical infrastructures.

For RPAS with MTOM ≤ 2 kg, all the operations are not considered critical if the vehicle is assured as a tool *not offensive* by ENAC or by otherwise qualified person. Flight operations are permitted only for person holding a certificate. The operations conducted by RPA of take-off mass ≤ 0.3 kg and speed maximum ≤ 60 km/h, are not considered critical in all operational scenarios. The pilot is not required to hold a certificate (Art.12).

Disposition for *declaration* and *authorization* application are reported in Article 9. The *declaration*, made by the operator, must certify compliance with the applicable sections of the Regulations and specify the conditions and limitations applicable to envisaged flight operations, including, possibly, the need to operate in segregated airspace. To obtain the *authorization*, the operator shall submit a form to ENAC, attesting compliance with the applicable sections of the Regulations and indicating conditions and limitations applicable to envisaged flight operations, including, possibly, the need to operate in segregated airspace.

The operator must have an adequate technical and operational organization for the activities and provide operations handbook setting out procedures necessary for managing flight operations and systems maintenance. Furthermore, the operator has the obligation to record and store data of activities, including assessments of related risk associated.

For manufacturers of RPAS < 25 kg, Article 123 specifies that they may require ENAC the release of a *Project Certificate* attesting compliance with the Regulations. In particular, the manufacturer must demonstrate to have: i) a suitable organization for the management of incidents; ii) the RPAS configured correctly; iii) carried out analyses and tests necessary to establish, depending on the scenario envisaged, the conditions and limitations to related level of security; iiii) prepared the Flight Manual and Maintenance Manual or equivalent documents. For the use in critical specialized operations, any RPAS holding a certificate of project must be accompanied by a certificate of conformity issued by the manufacturer certifying the compliance to the configuration identified in the project certificate.

Section III

This section covers RPA with a mass greater than or equal to 25 kg. The items discussed are similar to those in the previous section, with the difference that the qualification to navigation must be attested by the same types of certificates provided for manned aircraft.

These RPAS must be recorded trough registration in the Register of Remote Pilot Aircraft. Following registration, dedicated registration marks are affixed both on vehicle and on GS. The enabling navigation is confirmed by issuance of *Flight License* specifying the conditions and/or limitations, where the operations will be conducted.

In order to carry out specialized operations, the RPAS operator must obtain the permission of ENAC, demonstrating to have an adequate technical and operational organization for the activities intending to carry out and to establish an adequate maintenance program to ensure the maintenance of 'airworthiness'.

Section IV

In this section, provisions applicable to all RPAS pilots are specified and the RPA training centres are described.

To conduct unmanned aerial vehicle with MTOM < 25 kg in VLOS conditions it is necessary to hold a *Pilot Certificate*. This is issued by a RPA Training Centre after completion of a training course and a training program about type or class RPA to pilot, and passing a practical examination in an approved RPA Training centre (art.21).

To conduct unmanned aerial vehicle with MTOM ≥ 25 kg or for all the operations of BLOS is necessary to hold the *Pilot License* issued by ENAC. The pilot License and Certificate are issued in accordance with the same procedures used for personnel flight licenses, and are valid for five years. To obtain a RPA pilot license, the applicant must demonstrate adequate aeronautical knowledge base and conduction capacity of the RPA acquiring according to programs established by the Organisation and carried out at in approved RPA training centres holding specific qualification (art.22).

The RPA training centres are approved by ENAC and provide both theoretical and practical training. They must be equipped with appropriate organization and have a sound process, teaching materials and resources for training, one or more instructors and at least one examiner, recognized by ENAC, to oversee the practical tests and the release or the renewal of RPA pilot Certificates (art.23).

Section V

Rules of circulation and use of airspace are discussed in Section V for VLOS, EVLOS and BLOS operations for any RPAS.

The VLOS operations are permitted up to a maximum distance of 500 m in the horizontal plane and up to a maximum height of 150 m AGL (Above Ground Level). Distances and heights exceeding the limits may be authorized by ENAC, following a risk assessment. VLOS operations cannot be conducted within the traffic airport, in the areas below the take-off and landing trajectories and at a distance of less than 5 km. Furthermore, these operations cannot be conducted within regulated or prohibited areas, reported in the AIP (Aeronautical Information

Publication). In the areas below the take-off and landing trajectory, from 5 to 15 km, the maximum relative flight elevation is 30 m.

The BLOS operations are permitted up to a maximum distance in the horizontal plane of 500 m and up to a maximum height of 150 m AGL. Distances and heights above may be authorized by ENAC, following a risk assessment.

Alternative methods should be adopted to maintain eye contact with the RPAS by means of observers and / or additional pilot stations. These operations can be conducted only with the approval by ENAC and only within segregated airspace (temporary or permanent). Segregated airspace is controlled airspace or uncontrolled expressly identified in size, volume and time windows for any particular purpose and expressly authorized by the Civil Aviation Authority. BLOS operations must comply with the same rules as VLOS operations near airports.

Finally, RPAS *uncritical* operations in VLOS and EVLOS, with an operating mass take-off of less than 25 kg, must be conducted at a horizontal distance of safety of at least 150 m from congested areas, and at least 50 m from people who are not under the direct control of the RPA operator. These operations for RPAS less than 25 kg can be conducted within the regulated areas, following a specific request to ENAC for authorization.

In all other cases, the operator must submit to ENAC an appropriate risk assessment. Unless specific provision by ENAC for special operations, and with the agreement with the supplier of the Air Navigation Services in charge, the RPAS operations are not provided of air traffic services and do not require the use of the transponder within the space national air.

Section VI

In this Section general provision for RPAS are regulated, i.e. conservation of the documentations, communications, sanctions, insurances, privacy, etc., by RPA operators. The conservation of documentation produced for RPAS is mandatory for operator, manufacturer, organization of the project and pilot in accordance with their responsibility, since they are required to maintain and make it available to ENAC (art. 28). The same subjects, in accordance with their responsibility, are required to report to ENAC, within the limit of 72 hours, any accident and serious incident.

Temporary or long-term sanctions are foreseen for those who violate the Regulations (art. 30). Indeed, ENAC may take measures to suspend all or part of the authorizations or certifications up to 6 months, in case of breach of Regulations or in case of lack of assurance from the operator of compliance with the requirements of the Regulations. ENAC may take measures to suspend the validity of the Pilot Certificates or Licenses for up to 12 months, in the case of failure to respect the rules set by the Regulation by the RPA pilot. Furthermore, administrative sanctions provided for in Article 1174 of the Code of navigation in the event of lack of necessary provided authorization ENAC for critical operations or of operator declaration for the non-critical operations.

Obligations for the RPA operator during planning and flight operations are given in Articles 31-33. The operator must take appropriate measures to protect the RPAS to prevent illegal acts during the operations through voluntary interference on the *radio link*. The operator must ensure the implementation of the functions of *Command and Control*, through the *data link*, with necessary continuity and reliability in relation to the area of operations. He must establish procedures to prevent access of unauthorized persons to the area of operations, in particular to the control station, and the securing of the system and must verify the existence of any instructions issued by the police authorities in the areas affected by operations.

The latter provision regard data protection and privacy (art.34). Where the operations carried out through a RPAS could lead to the processing of personal data, this must be mentioned in the documents submitted for the issuance of the relevant authorization. The processing of personal data must be made in each case in accordance with the decree of 30 June 2003, n. 196, as amended (Code concerning the protection of personal data), with particular regard to the use of arrangements that avoid identification when unnecessary in accordance with art.3 of the Code, as well as measures and precautions to safeguard the interested prescribed by the Authority for the protection of personal data.

Section VII

In this section is governed the use of model aircraft. The pilot of a model aircraft is responsible for operating the vehicle in order to comply with the rules of the air, not to cause risk to persons or property on the ground and other airspace users, maintain obstacle clearance, avoid collisions in flight and give way to all. It is allowed the flight operations up to a maximum height of 150 m.

Reserved airspace is not required for their use (art. 35):

a. In the presence of subsequent maximum requirements: take-off operating mass less than 25 kg; wing surface less than 500 dm^2; total volume of piston engines less than 250 cm^3; or total thrust of the turbine engine less than 25 kg (250 N) or the maximum total power of turboprop engines less than 15 kW.
b. When the aircraft are in free flight or a flight bound circular; or they are hot-air balloons with the total weight of the container of transported gas to the burners not exceeding 5 kg.

c. When the activity is carried out by day and the model aircraft maintains a constant visual contact with the pilot on ground, without optical aids and/or electronic;

When the activity is performed in appropriately selected areas from the model aircraft pilot, in a radius of 200 m. and a height not exceeding 70 m., non-populated, enough apart from buildings, infrastructure and facilities, outside areas of traffic, at a distance of at least 5 km from the perimeter of an airfield without traffic area.

Chapter 3
UAS Photogrammetry

3.1. Introduction

In the last thirty years, there has been a surge of interest in automatic 3D reconstruction from images. The ubiquity of digital compact cameras, smartphones, tablets and the easiness of geotagging and sharing images via internet put them at the core of many services and apps where 3D modelling or the availability of 3D models plays a key role. Though for decades a sizeable part of the Computer Vision (CV) community has been involved in 3D reconstruction from imagery early in the military sector and later in robotics and industrial applications, this new centrality of digital images meant that more and more computer scientists and computer engineers joined the field

Starting from the last decade, there was a dramatic increase in the use of Unmanned Aircraft Systems in Photogrammetry and Remote Sensing (PaRS) for applications such as environmental monitoring, cultural heritage, surveillance and many other.

Today, UASs can be used as a precise, automated and computer-controlled data acquisition and measurement platform, thanks to the recent developments of low-cost sensors such as off-the-shelf digital cameras, GPS/INS (Inertial Navigation System) based stabilized platforms, navigation units and laser scanners.

This chapter focus on the image acquisition and processing pipeline of the UAS photogrammetric workflow and on its role in Geomatics.

3.2. Potential of UAS photogrammetry

In the field of Geomatics, UAV photogrammetry opens various new close range applications, somehow encompassing aerial and terrestrial photogrammetry, but also introduces new (near) real time applications and low-cost alternatives to the classical manned aerial photogrammetry as summarized in Table 3.2.1. Overall, UAS photogrammetry is a cost effective survey technique, delivering consistently high quality results. UAS can fly at very low altitudes acquiring high-resolution images. Gimbals and mounting devices allow for capturing images of objects that are difficult to acquire in traditional aerial surveys. Obvious examples are building facades, dams, rock walls, quarries and cultural heritage ruins. Furthermore, also building elements (belfries, rose windows, roofs) that often cannot be acquired from the ground, are now surveyed at high resolution offering unprecedented completeness of object coverage. UAS imagery from low cost compact cameras, SLR digital cameras or even multispectral sensors, can be employed for classification, DSM and orthophoto production, restoration planning, monitoring. UAS are proving very useful or indeed even invaluable in a post disaster scenario

[9], (think e.g. of L'Aquila earthquake or Fukushima nuclear power plant incident) where most of the difficulties are related to the accessibility and safety.

Figure 3.2.1 – 24th March, 2011 aerial photo taken by a drone and released by AIR PHOTO SERVICE [5], the crippled Fukushima Dai-ichi nuclear power plant. From top to bottom, Unit 1 through Unit 4. (Air Photo Service Co. Ltd., Japan).

If large areas have been affected, manned aerial photogrammetry provides the general picture for overall damage evaluation. However, in most cases the photogrammetric products are not enough detailed and accurate to study the damaged structures. On the other hand, using micro UAVs for surveying in such particular cases can easily bypass many of these problems [61]. There are no accessibility problems for an UAV mainly because of the extreme flying flexibility. Being fully or almost fully remotely controlled they involve little risk for the operators. In addition, drones are well-suited to support post-disaster investigation of damaged buildings. Examples of management of post disaster taking advantage of UAS for quick damage assessment are presented in [21], in post-seismic environment in [9], for quick-response to natural disaster with generation of hazard map in [66] and [132]. Environmental monitoring is another rapidly expanding field of application, where UAVs are used on landslides [77], to control soil erosion [33], rangeland [74], rock glaciers [27], forestry [55], forest fire [80] and highway traffic [106].

UAV photogrammetry can be understood as a mapping method suitable for different accuracy ranges and surveys of areas up to a few square kilometres (Table

3.2.1). Hence, UAS photogrammetry is used in applications like forestry [55], tree classification [49], cultural heritage [105], map production and updating and 3D modelling [102].

UAV images are also often used in combination with terrestrial surveying in order to close gaps in 3D models and create orthoimages [95] and [101].

Table 3.2.1 – Features of aerial, close range and UAV photogrammetry, from [39].

	Aerial	**Close Range**	**UAV**
Planning	Semi-automatic	manual	Automatic-manual
Image acquisition	Assisted/manual	Autonom/assisted/ manual	Autonom/assisted/ manual
Size of area	km^2	mm^2 - m^2	m^2 - km^2
GSD	cm – m	mm - dm	mm - m
Camera viewing direction	Nadiral/oblique	Nadiral/oblique	Nadiral/oblique
Absolute accuracy of auxiliary EO data	cm-dm	cm	cm - m
Image blocks size	10 – 1000	1 - 500	1 - 1000
Applications	Small and medium scale (mapping, forestry, 3d-city modelling)	Cultural heritage and archaeology, 3d modelling of buildings, industrial metrology	Large scale surveys (cultural heritage and archaeology, 3d modelling of buildings, monitoring of hazards, mapping, landscape classification)

Concurrently to improvements of UAVs in Photogrammetry, [39] suggests a review of the categorization scheme of measurement techniques proposed by Luhmann [79], that relates the object size to the expected accuracy. The new scheme, shown in Figure 3.2.2, puts UAS photogrammetry between close-range and aerial photogrammetry, as in Table 3.2.1, for achievable ground resolution, object size, as well as expected accuracy. Indeed, for an accuracy range of about 1-10 cm UAV photogrammetry is placed between terrestrial laser scanning (TLS) and terrestrial photogrammetry. Considering the same object size, UAV accuracy is in between GPS and aerial photogrammetry at around 10^3 mm. Nevertheless, the categorization is insufficient to describe the performance of each system in different conditions; indeed, if also the height of the object is taken into account, some of the cited methods may not cover the entire object with the reported accuracy.

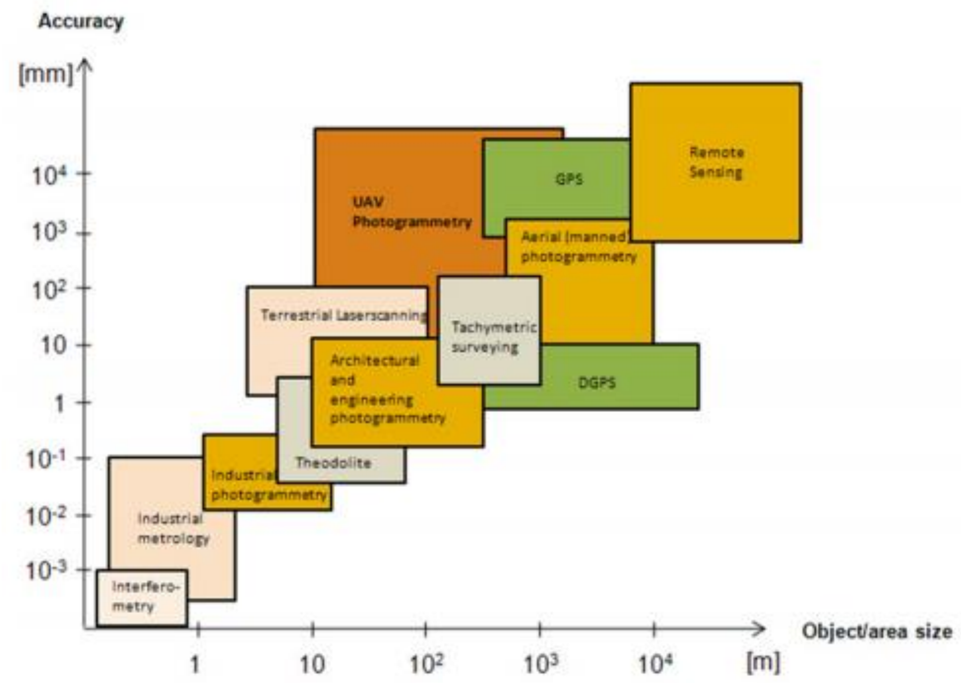

Figure 3.2.2 – The accuracy of measurement methods in relation to the object/area size in [39], a review of [79].

In the following paragraphs, the aspects of the photogrammetric workflow likely to change when drones are used will be discussed. As for terrestrial applications, the scientific interest is highly focused on the automation of the procedure, starting from autonomous flight control [16], up to image orientation, dense matching, DSM and orthoimage generation [59]. The typical acquisition and processing pipeline for UAV images is shown in Figure 3.2.3.

The mission planning considers both the flight parameters (i.e. size of area of interest, ground sample distance, relative flight height, flight lines) and the UAS platform characteristics. The high level of automation and reliability reached by digital photogrammetry allows in most cases for a smooth block orientation. Dense matching provide a high resolution DSM that is the basis for 3D Modelling and orthophotos generation. Accurate results are usually obtained using pre-signalized ground control points (GCPs) measured with GNSS technique and interior orientation (IO) parameters calculated with camera calibration [73].

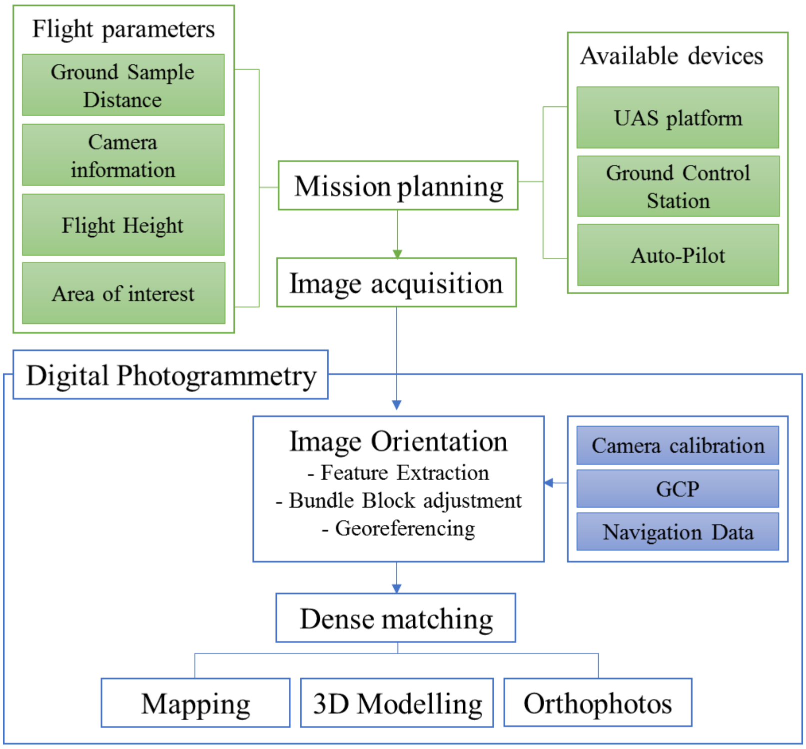

Figure 3.2.3 – Flowchart of a UAS photogrammetric project.

The progress in miniaturisation of computer systems equipped with lightweight operating system as well as positioning and attitude sensors, driven perhaps by the automotive industry, made the basis for the dramatic development of UAS, providing cheap hardware and easy interfacing tools to develop auto-pilot systems. Equipped with digital cameras, UAS overcome some of the limitations of satellite imagery and aerial photography, namely spatial and temporal resolution [102]. With drones, imaging of the area of interest is made independently of the fixed scheduling of most satellite imagery or by the availability of the expensive equipment of aerial photogrammetry. Indeed, the ease of use and low running costs of UASs allow for carrying out frequent missions, providing very high temporal and spatial resolutions datasets in the desired time span.

Furthermore, though the quality of UAS camera optics is not comparable to that of aerial cameras, the lower relative flight height delivers a typical GSD of 3-5 cm against the 10-100 cm of aerial and satellite images. As far as metric accuracy of object restitution is concerned, the potential of UAV blocks far exceeds the requirements of large scale maps (1:2000, 1:1000) either by using the traditional formulae for stereo restitution with analogue cameras or the "GSD rule" used with aerial digital cameras. In this regard therefore, map production at such scales would be inefficient and the tipping point in deciding between aerial or UAS photogrammetry would be the size of the area and the incidence of the fixed costs of a flight. Given their versatility, UAS could reasonably extend the map scale afforded by photogrammetry (and today left to ground topographic survey) to 1:500 and perhaps to larger values; however, how large this market could be is not so clear. UAS are also well placed to fill the need for very high spatial resolution at low cost in remote sensing for agriculture, whenever valuable crop in relatively small plots could benefit from regular checks to increase productivity and fine tune deliver of water, chemicals and harvesting. Some examples of UAV in agriculture are the RPV system named Crop Condor (http://www.calmarlabs.com/condor.html) in US and the unmanned helicopter-based system [6] in Germany. As for mapping, using manned or unmanned aircrafts for agriculture or other remote sensing tasks will depend in most cases on costs rather than technological gaps. In fact, airborne remote sensing from manned aircraft or from satellite imagery initial, operating and maintenance costs are generally larger compared to UAVs, though the productivity is obviously larger. A larger number of sensors is today available for remote sensing on manned aircraft, normally with better performance of those that can be carried by drones; this technology gap could be somehow reduced, however, if a market develops that drives investments on sensor miniaturization.

UAS photogrammetry was born in a mature digital era for hardware as well as for automation of data processing [81]. Quoting Leberl [75], “Since its inception, photogrammetry was driven by the goal of minimizing the number of (film) images for any given project. Every additional image caused additional costs for materials, film development, processing time, and resulted in yet another stereo model to be manually processed.” In traditional stereo photogrammetry a surface point was defined by two optical rays only, providing four equations (Eq. 3.2.1- Eq. 3.2.2) to solve for the three unknown coordinates *X*, *Y*, and *Z*.

$$x_i' = f_x(x_0, y_0, z_0, \omega, \varphi, k, c, x_p, y_p, k_1, k_2, k_3, p_1, p_2, X_i, Y_i, Z_i) \quad \textbf{(3.2.1)}$$

$$y_i' = f_y(x_0, y_0, z_0, \omega, \varphi, k, c, x_p, y_p, k_1, k_2, k_3, p_1, p_2, X_i, Y_i, Z_i) \quad \textbf{(3.2.2)}$$

x_0, y_0, z_0: coordinates of the perspective centre;
ω, φ, k: independent rotations about the x, y, z coordinate axes;
c: focal length;
x_p, y_p: coordinates of the principal point;
k_1, k_2, k_3, p_1, p_2: distortion parameters;
X, Y, Z: ground point coordinates in object space.

Still in the same paper, Leberl [75] summarizes the great potential of automation for photogrammetry and the transition from stereo to multi-image photogrammetry: “These four equations for three unknowns have led to a photogrammetric workflow that hardly satisfied the surveyors rule for reasonable redundancy. The transition to digital sensing did away with the extra cost for extra imagery. Automation does away with extra labour per image. Multi-view geometry does away with the idea that an additional image necessitates additional work with an additional stereo model [63]. Images can now be produced at 80 percent forward overlap, increasing the number of images per object point from two to five, at no additional cost of acquisition. At 90 percent forward overlap, the number of images per object point within a flight line grows to ten. In addition, by an increase of the side-lap from the traditional 20 percent to now 60 percent, the add-on cost will increase only for the additional airtime, but not for the increase in the number of images. The strategy increases the number of images per object point to 10 (at an 80 percent overlap) or even 20 (at a 90 percent overlap). The benefits are numerous: reduced occlusions, higher level of automation, reduced occurrence of blunders/gross errors and therefore less manual editing, and finally an increase of geometric accuracy”.

The discussion above clearly points to a still to be fully explored question on the accuracy and precision of the restitution (basically, of the DSM) when using a multi-image multi rays technique. Though indeed the extreme overlap values proposed above are seldom used in commercial operations by aerial photogrammetry, indeed larger forward and above all larger sidelap are actually employed compare to blocks flown with analogue cameras. The variety of camera format and focal lengths (compare to the uniformity of analogue cameras) makes it difficult to find a standard to predict the accuracy of the restitution, mainly in elevation. However, the transition to larger overlaps and to multi image matching should close the gap between the precision of tie points and the precision of DSM points, with a gain in uniformity over the block. Indeed, due to less sophisticated image shooting and camera stabilization devices, it is customary to adopt large overlaps in UAS blocks. UAS photogrammetry is therefore set to gain particularly from multi-image techniques.

3.3. Flight planning

Though not as important as in aerial photogrammetry, flight planning and its careful execution are a necessary step for obtaining the accuracy and completeness required for the project.

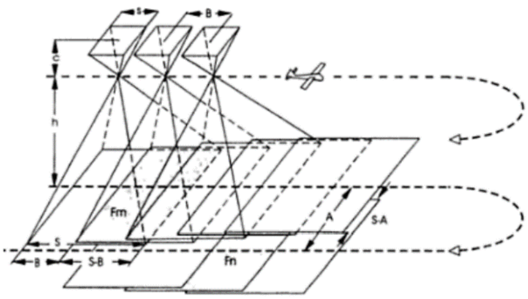

A = Distance between flight lines/stripes
B = Base (between consecutive images)
c = Principal distance
sx, sy = sensor size along and across strip
h = Flying height above ground
Z = Ground height
L = Length of a strip/block
Q = Block width

Figure 3.3.1 – Geometry of the flight plan in flat areas [70].

The most important parameters and formulas for mission planning of an aerial survey can be found in the literature (see e.g. [129] and [70]): they refer to the square format of the analogue film cameras. The main parameters for photogrammetric UAV flight planning according to [39] are listed below:

Photo scale number $$m_b = \frac{h}{c} \quad \textbf{(3.3.1)}$$

Image sides on the ground $$S_x = sx \times m_b \qquad S_y = sy \times m_b \quad \textbf{(3.3.2)}$$

Base-length for 1% overlap $$B = S_x \left(1 - \frac{l}{100}\right) \quad \textbf{(3.3.3)}$$

Distance between strips for q% side-lap $$A = S_y \left(1 - \frac{q}{100}\right) \quad \textbf{(3.3.4)}$$

Area of a stereoscopic model $$F_m = S_y \left(S_x - B\right) \quad \textbf{(3.3.5)}$$

x-parallax accuracy $$\sigma_{p_x} = \sigma_{meas} \times d_{pixel} \quad \textbf{(3.3.6)}$$

Height accuracy $$\sigma_z = m_b \times \frac{h}{B} \times \sigma_{p_x} \quad \textbf{(3.3.7)}$$

As reference, to determine the expected accuracy on the ground height Z, the normal case of stereo-photogrammetry, where the camera axes are perpendicular to the base B and parallel to one another [70] is used. Therefore, Eq. (3.3.7) defines the height accuracy and Eq. ((3.3.6) refers to x-parallax accuracy, computed from variance propagation. The x-parallax accuracy σ_{p_x}depends on pixel size d_{pixel} and on the operator's ability to recognize the same feature on the images σ_{meas} (i.e. in today's digital photogrammetry the image matching accuracy). The choice of its value is consequently demanded from the user and should also depend on the quality of the images: with motion blur or low S/N (Signal to Noise) ratio due to poor sensor quality, higher collimation (matching) errors should be expected. The open issue is to strike a balance between on the one hand the pixel size (some cameras have pixels as small as 1 μm as the Canon Ixus 125 HS) and on the other hand the sub-pixel capability of interest operators to detect homologous points over two or more images. Indeed, σ_{meas} value with feature-based (FB) and area-based (AB) matching reportedly ranges between 0.1-0.5 pixel. However, it is hard to believe that the physical dimension of the cell on the sensor does not influence image quality and in general, that sensor quality does not play a part in matching accuracy. Moreover, it should not be forgotten that modelling of systematic errors should at least match the x-parallax accuracy: therefore, any increase in accuracy should come from both fronts.

To ensure full ground stereo coverage and effective block orientation by Aerial Triangulation (AAT) or Structure from Motion (SfM), blocks are arranged in overlapping image strips. In modern aerial photogrammetry with digital cameras, usually a forward overlap between 60 and 90% and a sidelap between 20 and 60% is chosen. If drones are used, an overlap of 80% in both directions is preferable. The reasons lie in the high wind sensitivity, which causes wind drifts and roll angles far exceeding the 5° limit normally allowed for traditional aerial stereo photogrammetry. Furthermore, most of the current UAVs use a low cost GPS with an accuracy of 3-5 m and are anyway highly sensitive to wind. As a result, it is not sure that every image is taken at the desired point: with base-lengths and distances between strips of a few dozens of meters, this means that actual overlaps might differ from planned by far more than 5%. An overlap of 80% in both directions ensures that a complete 3D model will be obtained even if some images are missing or taken in a wrong place.

Flight planning aims at reducing cost and improving the efficiency of the survey. In analogue photogrammetry, this meant above all to reduce the number of images, so setting the image scale and the overlaps to the minimum necessary. In digital photogrammetry in general and in UAS photogrammetry the cost of additional images is primarily due to longer flight time (for additional strips due to larger-than-usual sidelap only) and processing time. While the latter is a not so important item in the budget of an UAS photogrammetric project, the former indeed is, as far as the flight is carried out by a contractor. It might be therefore striking for practitioners used to the 60%-20% values of analogue photogrammetry to talk of efficiency in flight planning if such large overlaps are used. However, the notion of project efficiency must be enlarged to include image orientation, dense matching, occlusion minimization and completeness maximization. In this light, the number of parameters to optimize is smaller than and to some extent different from those in aerial digital photogrammetry.

Table 3.3.1 – Flight Planning of UAV survey on the Campus of Parma with the same values of flight height, sensor camera, overlap and area of interest, but with short image size along (A) or across (B) flight direction.

Focal length *c* (mm)	16	
Flying Height *h* (m)	100	
Image scale m_b	6250	
d_{pixel} (µm)	4.7	
Area size (m)	Width = 600; Height = 500	
Sensor size (mm)	24 x 16	
Overlap (%)	Forward = 80; Sidelap = 80	
Image footprint	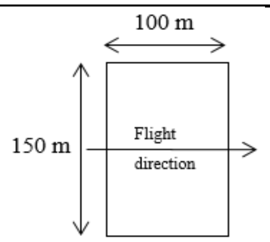	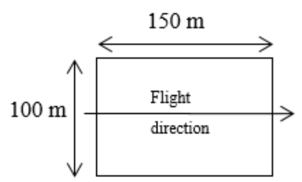
Base-length (m)	20	30
N. images per strip	31	21
Distance between flight lines (m)	30	20
N. strips	13	21
Total images	403	441
	(A)	(B)

For instance, due to restriction on maximum relative flight elevation, the image scale can be controlled only by the choice of the principal distance; as already pointed out, this often means an excess of accuracy with respect to survey requirements. The variety of available cameras as far as sensor size, resolution, pixel size are concerned however, shift part of the optimization to the selection of the appropriate camera-lens combination. In addition, due to the rectangular shape of the sensor, two mounting options are available. Placing the longest side of camera sensor perpendicular to flight direction, as reported in Table 3.3.1, where the same area with identical overlaps and relative flight height is considered, is more convenient in terms of total number of images. This example is taken from the flight planning of the drone survey over the Campus of Parma, which will be discussed in Section 5.2.

Software tools for flight and path planning for UAVs have been developed for military, robotics, computer vision and artificial intelligence applications. Mission tasks from simple recreational use [1] to more serious collision avoidance [20, 92], automated target tracking [87] and “follow me” [134] operations have been implemented. The degree of sophistication goes as far as to coordinate groups of UAS (swarms) dedicated to a specific mission, flying in an environment where static and moving obstacles occur and fast determination of collision-free trajectories [110] is necessary. Handling of interference with other flying objects and obstacles, for long a military or academic exercise is now becoming a key capability, being requested for the certification of UAS for outdoor surveys in critical operations. More on-board sensors and computing power is necessary to manage such safety features and different strategies might be used depending on the characteristics of the environment where the UAS is supposed to operate. Nowadays, waypoint navigation for UAVs is a standard tool [86]: flights are based on defined points in a global coordinate system provided by GNSS.

For photogrammetric applications, UAV mission planning software requires the integration of some additional functions similar to those implemented in standard photogrammetric aerial flight planning tools. In autonomous UAVs flights, a “Start” and a “Home” point have to be defined. The “Start” point is from where the UAS is supposed to start taking images and begin the survey: the mission is set up relative to its coordinates. The “Home” point is the point designated for safety reason where the drone has to go back in case of mission failure (in Figure 3.3.2, it is indicated as “Home”). It is usually the same used for take-off.

Some packages allow, in addition to way points (WP), the definition of lines, paths, boundaries and no-go areas [52]. This is useful for completely autonomous UAV missions, such as in military applications or for reconnaissance flights but is becoming mandatory also for civil mission close to critical areas (see requirement of geofencing capabilities in 2.7.1). Furthermore, almost all recent flight planning systems include parameters like altitude, camera information, GSD, necessary for mission planning.

3.3.1. Ground Control Station: Mission planner

A very active drone community has grown around forums, focus groups and a number of projects pushed by the parallel improvements in computer science, sensor miniaturization and telecommunications have been proposed and carried out. The Dronecode Project [35] is emblematic: it is an open source, collaborative project that puts drone projects under a non-profit structure governed by The Linux Foundation [78]. The result is a common, shared open source platform for UAVs.

Some of the drones flights described in this thesis were planned and controlled with an open source software developed in recent years by this “large community of enthusiasts” [7]: Mission Planner (MP) made by ArduPilot (APM) system [82]. MP is a ground control station for plane, copter and rover. As fundamental pieces in UAS, GCS have evolved over the past decades. GCSs are stationary or transportable hardware/software devices to monitor and command the unmanned aircraft. Although the word ground is inherent to the concept, a drone may actually be operated from ground, sea or air. GCSs are probably as important as the vehicles themselves, as they enable the interface with the ‘‘human intelligence’’ (any change to the UAS route, any error message from the aerial platform and/or any outcome of the payload sensors shall be sent to and inspected at the GCS).

Mission Planner can be used as a configuration utility or as a dynamic control supplement for the autonomous vehicle. MP assists mission planning, manages APM during flights and helps to analyse mission logs afterwards. Available functions are:

- Plan, save and load autonomous missions into the autopilot with point-and-click waypoint entry on Google Earth or other maps.
- Download and analyse mission logs created by owner autopilot.
- Interface with a PC flight simulator to create a full hardware-in-the-loop UAV simulator.

  With telemetry hardware, it is possible to: i) Monitor vehicle status while in operation. ii) Record telemetry logs that contain more information than the on-board autopilot logs. iii) View and analyse the telemetry logs. iiii) Operate your vehicle in first person view.

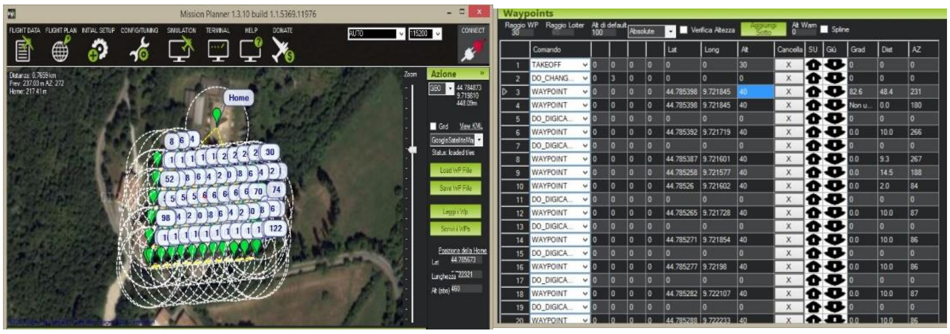

Figure 3.3.2 – Example of flight plan in Mission Planner: on the left the projection of WP on the Google Satellite Map; on the right the command list and the WP coordinates.

3.4. Navigation and orientation systems

The use of an autonomous navigation/positioning system enables most UAVs to follow a predefined flight plan and also to record the actual trajectory for post-mission log checks. The large majority of navigation systems is based on GNSS/INS technology, but alternative solutions integrating other kinds of data (e.g. scans and images) have been implemented, especially for indoor navigation. The user-friendly interfaces and the availability of internet maps and satellite make flight planning rather straightforward in most cases: the autonomous operation mode is therefore the standard for non-recreational use of UAS. Of course, UAVs can also fly under manual control by the pilot but this option is normally exploited when the mission objective and the complexity of the environment to explore are difficult to translate in a predetermined sequence of waypoints (think for instance of inspections of rock faces or of damaged buildings). The need for manual piloting applies also typically to photogrammetric surveys where non-nadiral images are necessary or where the object to survey is developed in elevation as well as in horizontal. In such circumstances, only multi-rotor UAS can be employed.

However, the homogeneity of precision and the degree of completeness of the stereo coverage of an object surveyed photogrammetrically is strongly influenced by the actual flight pattern (Figure 3.4.1). When nadir images and stereo or multi-image coverage of a terrain patch are required, a regular flight pattern with constant overlap parameters is clearly preferable. On the other hand, when the acquisition is executed in the manual mode, the image overlap and the flight lines will turn out to be very irregular in most cases. The on-board navigation system embedded in the auto-pilot, to the contrary, ensures that the acquisition will follow the WPs according to plan, except with strong or irregular wind blows.

a) *b)* *c)*

Figure 3.4.1 – Flight lines carried out in: a) manual mode (image overlap and flight height not respected); b) autonomous mode with low-cost navigation system (irregular image overlap); c) automated mode with low-cost quality navigation system.

UAVs are mostly equipped with a single frequency GNSS receiver, inertial sensors (accelerometer, gyroscopes) and a magnetometer for navigation purposes [133]. The accuracies of such sensor combinations are 2-10 m for the positions and

0.5 – 5 deg for the attitudes. While these accuracies are sufficient for navigation, they are mostly insufficient for directly georeferencing the collected mapping data. That is why the development of a precise direct georeferencing system for UAVs is currently in great demand [11] and actively pursued [97]. One technique, which is well suited to determine precise positions of mobile objects in a global reference frame is RTK-GPS. RTK-GPS is a differential GPS (DGPS) procedure that is based on carrier phase GNSS observations and leads to relative positions between a master and a rover station with centimetre accuracy in real time. The challenge of developing such a system for micro- and mini-sized UAVs is to stay within the space and weight limitations (about 500g) of the platform while keeping hardware and software costs in proportion to the overall ones. Though only a few studies exist by now, dealing with the integration of a RTK-GPS system on micro- or mini-sized UAVs [104, 40], some of the most active UAS manufactures are already selling systems claiming such capabilities as (quite expensive) alternative to the standard navigation-grade devices.

The costs of a pair of geodetic L1/L2 receivers (rover and local reference station) amounts to approximately USD 12,000 to 20,000, but prices are going down with more manufacturers entering the field. Turn-key systems including the GPS processing software are obviously more expensive than the basic kit to assemble. Therefore, dual frequency RTK GNSS receivers are not used in the mass market because they are still too expensive to be commonly used in low-cost solutions that rarely need such accuracy levels and therefore not managed by autopilot systems. However, the availability of RTK positioning and NRTK networks in particular is pushing the technical development to explore also this option, with interest growing towards more accurate navigation capabilities also outside photogrammetry. The goal is to find out whether single frequency GPS receivers are suited for RTK positioning in UAS as well as they turned out in terrestrial surveys [24]. The cost of these instruments ranges between 200 – 1,000 USD. Table 3.4.1 from [119] summarizes the consumer-grade antennas (upper part) and receivers (lower part) available in the market. In blue italic a geodetic-grade antenna-receiver for comparison.

Especially in kinematic applications frequent losses of lock of GPS signal can occur. Hence, a re-initialization of the integer ambiguities in phase measurements is necessary. The time required to estimate reliably the new ambiguity depends on the number and distribution of satellites, on the algorithms implemented and overall on availability of both L1/L2 frequencies. While with dual-frequency receivers less than one minute might be enough, with low cost single frequency receivers the time for a reliable solution is in the order of 10’ and more. This is obviously incompatible with a real time application and for use in direct georeferencing. Thus, the ambiguity resolution for precise positioning of UAVs has to be fast and robust at the same time.

Table 3.4.1 – Characteristics of low-cost antennas (upper) and receivers (lower) (italic: geodetic-grade) from [119].

Vendor	Antenna	Objective	Freq.	Type	Active/ Passive	LNA Gain	LNA NF	Size (mm)	weight (g)	Price	Note
u-blox	ANN-MS	General	L1	Patch	Active	27dB	1.5dB	40ϕ×48×13	105	$31	
Aero Antenna	AT575	General	L1	Patch	Active	12dB	?	53ϕ×13	113	$200	
AntCom	4G15A2-XS-3	Mini-Arinc Airborne	L1	Patch?	Active	?	?	55×86×17	?	$194	
Micro Pulse	2335TB	Vehicle Tracking	L1	Patch	Active	26dB	<2.5dB	65ϕ×12	28	$47	
Pioneer	GPS-M1ZZ Ant	General	L1	Patch	Active	?	?	31×35×12	?	?	
Trimble	Bullet III	General	L1	?	Active	35dB	<3.3dB	78ϕ×66	170	$125	
NovAtel	*GPS-702-GG*	*Geodetic/ Reference*	*L1/L2*	*Pinwheel*	*Active*	*29dB*	*2.0dB*	*185ϕ×69*	*500*	*$995*	Reference

Vendor	Receiver	Objective	Freq.	# of Channel	Max Rate	DGPS	Output	Size (mm)	Price	Note
u-blox	AEK-4T	General/ Timing	L1	16ch	4Hz/ 10Hz *1	SBAS/ RTCM	NMEA/ Binary	17×22×3 (Module)	$179 (Module)	
u-blox	EVK-5H	General	L1	50ch	4Hz/ 10Hz *1	SBAS/ RTCM	NMEA/ Binary *3	17×22×3 (Module)	$99 (Module)	
NovAtel	Superstart II (OEM Board)	Genaral	L1	12ch	1Hz/ 5Hz *2	SBAS/ RTCM	NMEA/ Binary	71×46×13	$165	
Hemisphere	Crescent (OEM Board)	General/ RTK-GPS	L1	12ch	1Hz/ 20Hz *2	SBAS/ RTCM	NMEA/ Binary	71×40×12	$285	
NovAtel	*OEMV-3*	*Geodetic/ Reference*	*L1/L2*	*24ch*	*20Hz*	*SBAS/ RTCM*	*NMEA/ Binary*	*185×160×71*	*$7,995 *4*	Reference

*, *1 Raw Measurement, *2 Optional, *3 F/W ver. 3.00, *4 No RTK Option*

Furthermore, cycle slips in the carrier phases have to be detected and repaired reliably. To improve the performances and to reduce the gap with dual frequency receivers, also the choice of the antennas for the reference and rover receivers is important. As reported in [119], a study on RTK-GPS performance with Low-cost single-frequency GPS receivers, the comparison between geodetic-grade versus consumer-grade antennas with the same receiver, shows large differences, especially for the code multipath (see Figure 3.4.2) that affects the performance of the RTK-GPS initialization. To improve TTFF (time-to-first-fix), it might be effective to replace a low-cost antenna with a geodetic-grade one. On the contrary, differences between geodetic-grade and consumer-grade receivers are in the same order of magnitude for carrier phase multipath as showed in Figure 3.4.3.

Whenever many cycle slips can be expected, as in terrestrial mobile mapping or vehicle navigation, a dual-frequency receiver is still necessary for fast recovery of the integer ambiguity. However, experimental works hints that low-cost single-frequency receivers could be applicable for short baseline RTK-GPS limited at the range of few hundred metres as described in [115]. In the same paper, an example of low-cost RTK GNSS system for Quadrocopter by Microdrones is described.

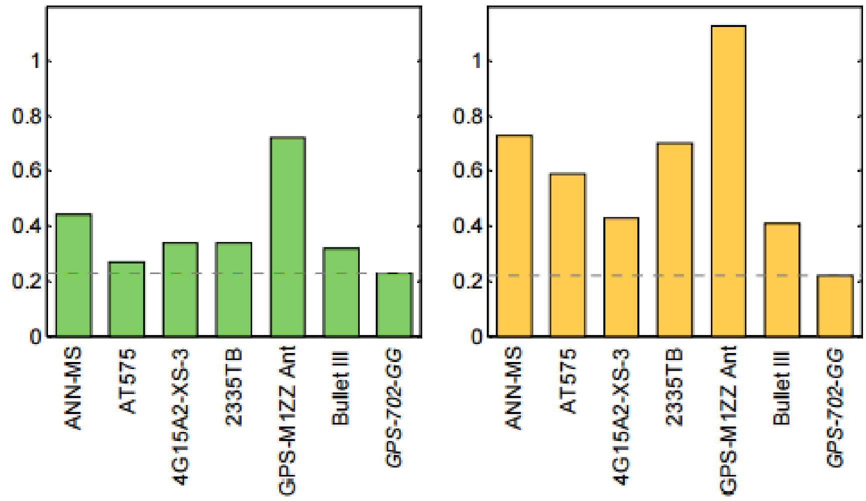

Figure 3.4.2 – Comparison of low-cost antennas with the same geodetic receiver Novatel OEMV-3 in [119]. On the left plot of carrier-phase multipath RMS in cm; on the right plot of code multipath RMS in m.

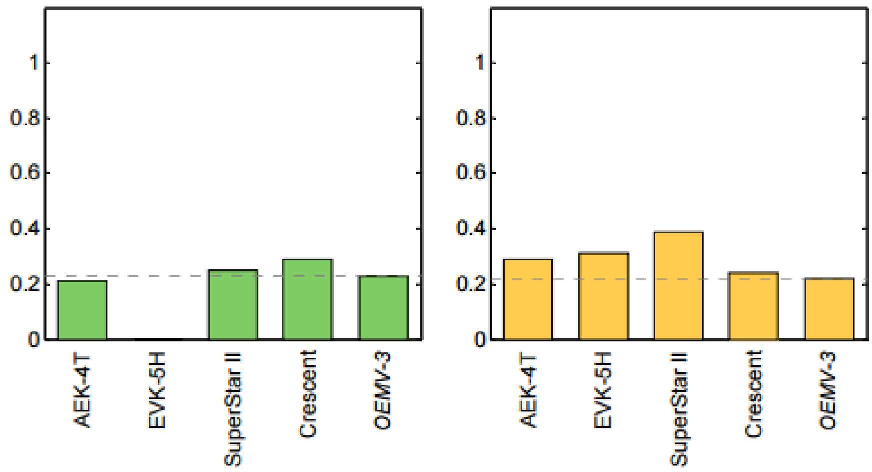

Figure 3.4.3 – Comparison of low-cost receivers with the same geodetic antenna Novatel GPS-702-GG in [119]. On the left plot of carrier-phase multipath RMS in cm; on the right plot of code multipath RMS in m.

An Ublox 6T with a Trimble Bullet III antenna are used and the system is supposed to deliver absolute 3D-positions with a few centimetres accuracy in real-time. The raw data analysis proved a 100% fixed solution of the carrier phases.

On the other hand, that the use of L1-only GPS receivers is still not yet established as a viable solution to UAS RTK positioning is apparent from the project Mikrokopter at the Bochum University of Applied Sciences, which has been running already for some years. First attempts since 2011 by using a L1 single frequency GPS receiver (Ublox LEA-6T) did not obtain clear-cut results supporting the accuracy of this positioning technique. Lately, as reported in [17], a switch to dual frequency has been performed and L1/L2 GPS receivers from Topcon OEM1 and B110 were installed on a Quadrocopter. Processing of RTK positions is performed using the RTKLIB open source package. Independent verification of the trajectory was performed by total station tracking an on-board prism. Though eccentricity between prism and antenna was not explicitly modelled, deviations better than 10 cm were reported for Fixed solutions and better than 50 cm for Float solutions.

It should be noted that, should a low-cost, sufficiently reliable and accurate RTK solution be available for UAS, this would not yet result in direct georeferencing of the images, since the attitude parameters of the images would still be unknown. In other words, also improvement in the IMU which is the core of the INS would be necessary. A recent study from the University of Calgary which is a leader in Inertial Navigation Systems, has tested the performance of inertial navigation aided by GPS single point positioning, differential Real Time Kinematic positioning and additional navigational aiding sensors [84]. Experimental data were acquired using a fixed-wing Penguin B UAV equipped with two different IMUs and an Ublox EVK-6T single frequency GNSS receiver. An additional GNSS-receiver identical to the on-board receiver was placed at the base station throughout the experiments, making RTK positioning available. Computation of the RTK position was done using the open-source program RTKLIB. The UAV flight, lasted overall about 35 minutes, making circles and figures-of-eight at more or less constant elevation. About 12 minutes of static acquisition prior to take-off were necessary to fix the ambiguity; during the actual flight (about 1700 s) the solution was mostly Fixed, though especially on the smallest circles, a large percentage of positions were determined as Float. The acceleration and gyro information from both IMUs were integrated in an Extended Kalman Filter with different aiding information, taking as reference the processing with magnetometer measurements and RTK positions. Then, the performance of the two IMU has been evaluated comparing position and attitudes computed with different aiding information (single point position, RTK position and velocity, RTK position only, etc.) with the reference. The Root Mean Square Error (RMSE) of position and attitude for both IMUs sensors were computed. As it could be expected, the closest results to the reference solution were obtained with aid of RTK position and velocity updates. Though this does not evaluate the intrinsic accuracy of RTK with a single frequency receiver, it points out that complete (position and attitude) direct georeferencing is possible only by integration of carrier phase kinematic positioning and navigation sensors.

There are many commercial software packages for processing of GNSS observations, in most cases developed by the manufacturers of geodetic-grade receivers; as default they require in input proprietary data formats but almost all accept also RINEX (a receiver-independent format). Processing GPS data is not a trivial task, so often only a limited number of options and processing parameters is made available, to relieve the average user from the background necessary for a correct setting. A very different approach is taken, in the spirit of low-cost and open source community, by the authors of RTKLIB [121], a software package for GNSS positioning. With this software, one can process and store raw GPS data on a real-time basis as well as in post-processing. It is well documented and it clearly explains what kind of algorithm are implemented. Its performance has been evaluated in [120, 130] and nowadays it is the leader of open source GPS data processing.

3.5. Data processing

Remotely piloted aircraft systems, being the low-cost alternative to the manned aerial photogrammetry, share the same workflow of digital photogrammetry and deliver basically the same products, as illustrated in Figure 3.2.3 in [34].

Several studies [25, 102] have been performed to evaluate the overall performance of UAS photogrammetry and the attainable accuracy level. They indicate that the automation degree of the data processing pipeline is already well developed as far as non-semantic products (such as DSM and orthophotos) are concerned. Besides, the quality of the products is in most circumstances very good (sometimes even more than required) though improvements are possible. This applies in particular to navigations sensors (i.e. DGPS, RTK GPS and INS) that should allow direct georeferencing of the captured images. Furthermore, DSM generation might be speeded up shifting the dense matching phase to GPUs as suggested in [102].

Much as in aerial photogrammetry, where automatic aerial triangulation [3, 44, 64, 111] is today a standard consolidated technique, so the orientation of UAV blocks should be performed automatically (georeferencing with GCP being the only manual phase). The presence of large image scale differences, illumination changes, occlusions and convergent imagery, especially in non-nadiral unstructured blocks is challenging for tie point extraction algorithms. However, though attempt to orientation might result in a failure using the early AAT techniques implemented in some commercial software, this is not the case with most software packages for

UAS. Indeed, the characteristics of UAS imagery are sometimes much closer to those usually afforded in close-range applications [72] than in aerial photogrammetry. In the nineties, AAT algorithms were designed assuming that interior orientation, radial and decentring distortions were stable and thus manageable by periodic pre-calibration. Block geometry was regular with almost nadir images, constant scale, overlap and attitude along the strips. In addition, also radiometric variations were known to be moderate. Being not true these assumptions in many drone blocks, automated procedures developed by the CV community for terrestrial photogrammetry, capable to handle irregular base-lengths or strong image scale variations and perspective differences have been adopted by UAS photogrammetry. Structure from Motion techniques have improved the automated image matching with feature extraction to facilitate the estimation of exterior orientation parameters. Only implementing CV techniques, software were capable to orient UAS blocks successfully [2, 23, 57, 102, 123], though with this came less control on some processing steps (such as georeferencing and block geometry inner strength) and on the accuracies of computed geometric parameters (i.e. EO parameters, tie points, IO parameters). However, evaluation of the accuracy is essential for photogrammetric purposes. In this respect, there is a lack of information in the current software outputs coming from the CV environment. More intermediate quality-control checks and more interactive editing tools should be introduced. A way to test and compare the capabilities of these new software programs is to output the tie points image coordinates and input them in well-established photogrammetric bundle adjustment programs, in order to assess the accuracy and reliability of block orientation. It would be helpful to plot colour-maps of tie points distribution in order to assess their homogeneity over the block. With this purpose, recent studies have compared the results of CV software with those of photogrammetric software [14, 50, 60, 73, 109]. On the other hand, the "new" mapping community is less sensitive to self-diagnosis tools and intermediate quality control checks and therefore more inclined to the use of fully automated implementations.

3.5.1. Camera calibration

Automatic block orientation is based on the integration of Computer Vision and photogrammetric methods to extract a great number of well-distributed tie points of a block captured with one or more (pre-)calibrated digital cameras.

Camera calibration is an essential component of photogrammetric measurement since the origin and in particular in image metrology. In photogrammetry a camera is calibrated when the principal distance (*f*), the principal point x and y coordinates

(pp_x and pp_y) and the distortion parameters (k_1, k_2, k_3, $p1$, $p2$, where the terms k_i represent coefficients of radial lens distortion and p_i terms represent decentring distortions) are known.

Three options are available to determine the calibration parameters: a) execute a pre-calibration where images are taken as much as possible in the same condition as the actual project; this is done before the flight, mostly using a calibration plate with markers or a test field and estimating the parameters with an extended BBA (Bundle Block Adjustment); b) estimate the parameters with a self-calibration BBA using the images of the actual project; c) a combination of pre-calibration and self-calibration. The first option allows to control and optimize the geometry of the calibration block but requires stability of the camera parameters for use in later projects; the second has the disadvantage that not always the block met such optimal characteristics; the third is actually the preferred one in aerial photogrammetry, also with the new digital cameras [68, 26], to remove systematic errors remaining after in situ (laboratory or test-field) calibration.

The camera calibration algorithms are generally based on a projective (CV) or a perspective (photogrammetry) camera model [98, 116], with the self-calibrating bundle adjustment with additional parameters dating back to 1970 [22] being the most popular. Nowadays, self-calibration is an integral part of block orientation in CV and extensively used also in photogrammetric AAT programs, though not with exactly the same meaning.

In CV self-calibration or auto-calibration means that constraints on the camera parameters or on the scene are used for recovering metric properties of the camera and of the scene from “uncalibrated” images. This process is generally used to upgrade from a projective reconstruction to a metric reconstruction (that is up to an arbitrary Euclidean transformation and arbitrary scale). Three type of constraints are employed (in conjunction or independently) in self-calibration: constraints on the imaged scene, on the camera motion or on the camera intrinsic parameters. Typically, therefore, after the self-calibration the block is still oriented in an arbitrary reference system with arbitrary scale, so is not georeferenced.

In aerial photogrammetry self-calibration means primarily an extended bundle block adjustment where the collinearity equations are complemented by additional parameters to adsorb systematic residual errors from a previous calibration. For a successful calibration, high overlaps, opposing flight directions as well as cross strips are necessary. In addition, unlike calibration of terrestrial cameras in laboratory, where the image network strength can be very high and free-net solution are also acceptable, GCP are normally required to avoid block deformation. Therefore, the bundle adjustment produces a georeferenced block.

Countless calibration techniques have been developed since the Brown model of the seventies (see [99] for a review on CV and photogrammetric techniques). Few papers deal specifically with camera calibration for UAV blocks, where pre-calibration is preferable and should be carried out in a specific test-field that includes depth and elevation changes and cross strips to reduce correlations among IO parameter [102]. Camera calibration from UAV imagery is also presented in [91] where the interior orientation parameters of the digital camera were estimated by two methods using in both cases the PhotoModeler Scanner software. A standard lab calibration based on the PhotoModeler flat pattern and the automatic field calibration routine was executed. The second method used an outdoor test field: 67 targets were placed on a flat surface of 25 x 25 m. Images were collected from a relative height of 50 m. After data processing, residuals of 0.723 and 0.700 pixel for lab and field calibration respectively have been obtained. Furthermore, the accuracy of field calibration was also checked comparing the coordinates obtained with PhotoModeler with GPS measurements of the same targets. The RMS of the discrepancies were in order of 2.6 cm for the altimetry and 2.8 cm for the horizontal coordinates, which translates in a relative accuracy of just 1/1.000.

3.5.2. Image orientation

In Computer Vision, the term Structure from Motion indicates all the techniques that allow the three-dimensional reconstruction of the scene and of the camera motion from a sequence of images. In the last decades, the SfM problem [127] has been thoroughly investigated and today, except in very specific cases, can be considered successfully solved. While in the early 2000s only a few (mainly scientific) software codes implemented Structure from Motion algorithms (e.g. Bundler [113], ATiPE [13], Apero [31], EyeDEA [107], Visual SFM [131]) in the last few years [103] automatic orientation tools were implemented also in several commercial software (PhotoModeler [94], Pix4D [93], Agisoft PhotoScan [4], etc.). The latter usually have an easy-to-use graphical user interface that helps the user inserting the basic processing parameters, organizing the images, showing, and analysing the results. On the other hand, to limit the software complexity, in most cases the user cannot interfere in the orientation workflow (e.g. modifying advanced processing parameter settings).

Almost all Structure from Motion approaches implement a very general relative orientation scheme (i.e. they do not assume that the image geometry should satisfy some particular constraint as other photogrammetric software do – e.g. constant overlaps, pseudo-nadiral images, constant image scale, etc.). This capability is welcome in UAS image block analysis since, sometimes, irregularity in the image block structure can arise, for example due to sudden gusts of wind that change the trajectory and/or, if active stabilization of attitude is not implemented, also the camera pointing.

Moreover, residuals and precisions are generally not available, therefore no thorough evaluation of the results can be carried out. Apart from the identification of the GCPs, no manual intervention is required because automated feature extraction and feature matching produce tens or hundreds of thousands of tie points distributed over the whole block and matches them across several images (i.e. getting close to the nominal multiplicity of each tie point). Automatic methods therefore extract more dense (and however robust) n-ples than an operator can measure by manual collimation in the traditional aerial triangulation.

Robust techniques, named Feature Based Matching (FBM), are employed to find sets of accurate and sub-pixel correspondences between the images: since the introduction of the very effective (and perhaps still top performer) Scale Invariant Feature Transform (SIFT) operator [76], many other were derived. To name a few: Speeded Up Robust Features (SURF) [18], Affine SIFT (ASIFT) [83] and Gradient Location and Orientation Histogram (GLOH) [81]. SIFT detects salient image regions (keypoints) and extracts discriminative yet compact descriptions of their appearance (descriptors). In the first stage, potential interest points are identified by scanning the image over location and scale by constructing a Gaussian pyramid and searching for local peaks (as keypoints) in a series of difference-of-Gaussian (DoG) images. The candidate keypoints are localized to sub-pixel accuracy and eliminated if unstable. Then, orientations for each keypoint based on its local image patch is determined. The assigned orientation, scale and location for each keypoint enables SIFT to construct a keypoint that is invariant to similarity transforms. The final stage builds a local image descriptor for each keypoint, based on the image gradients in its local neighbourhood [76]. Keypoints from multiple views of the same scene can be put in correspondence by comparing their descriptors. This may be used as a basis for a three-dimensional reconstruction of the scene.

In the automatic orientation, the image coordinates are searched to find and label multiple correspondences across images with the generation of the visibility map, namely a connection matrix between images for an initial network geometry analysis (see Figure 3.5.1).

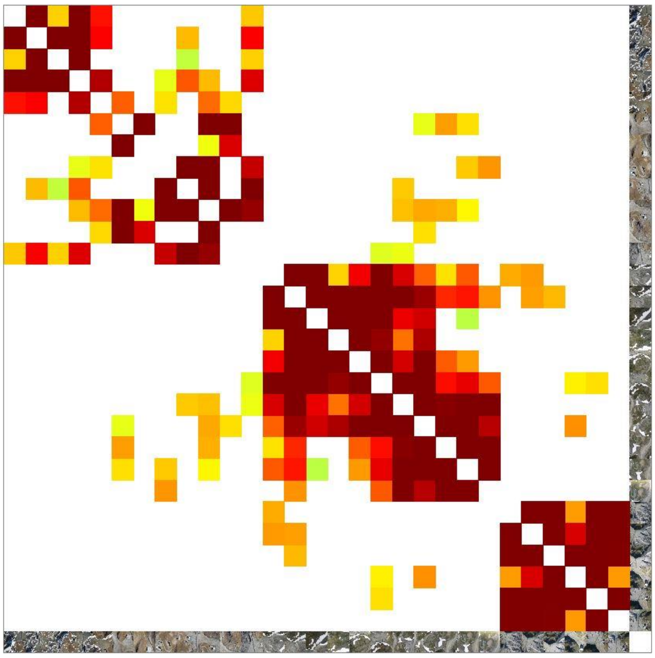

Figure 3.5.1 – Colour map of connection matrix between images of a UAS block: the brown to white colour scale indicates a decreasing number of correspondences (from high to none).

Homologous points are found by comparing the descriptor obtained previously in the detection. The comparison can be executed with different methods:

i. *exhaustive search* that is computationally very expensive since it is a linear search, which is quadratic in the number of interest points per image (for each point in the source image, one needs to search through all points in the target image);
ii. *approximate search* making use of tree search structures.

In the latter strategy, approximate nearest neighbour (ANN), presented in [8], is usually employed together with kD-trees [19] since it reduces the search time of a single feature query from linear to logarithmic. In [12] results of the implemented exhaustive and approximate strategies to compare feature descriptors and extract homologous points are reported in terms of matched features number and processing time. Both automated strategies for the comparison of the feature descriptors retrieve a sufficient number of image correspondences but mismatches still occur. To remove these mismatches geometrical constraints (e.g. relative orientation enforced with the epipolar constraint) are used. In particular, after the matching stage the putative correspondences will form the basis for camera pose estimation with the computation of essential (E) or fundamental (F) matrix. Through a robust estimation procedures, candidate matches are rejected as outliers if they do not satisfy the constraint. The robust fitting is usually done with RANSAC [41] where the E or F candidate matrix are computed at each iteration (for each random sample of correspondences).

Once the correspondences between image pairs are robustly extracted, they are linked across the images using graph matching. Based on the observation that not all input images has the same importance for the network, the full match graph is reduced to a skeletal graph [114]. The idea is to use only the images in the skeletal graph for an initial 3D reconstruction, and register the remaining images to the initial 3D model in a second step. This means a linear computational cost with respect to the number of images. Turning to the visibility map is helpful to slim the computational cost for the image sequence, especially for unordered sets of images.

In the last step, image coordinates are refined to improve their accuracy and to recover camera parameters (e.g., exterior orientation elements and principal distance) through a BBA. This minimization problem can be formulated as a non-linear least squares problem and solved with the Levenberg-Marquardt algorithm [113] (mostly used in CV) or by the Gauss-Newton method (normally preferred in Photogrammetry).

To reference the ground point coordinates and the Exterior Orientation parameters to a real-world system, either the camera positions or the positions of ground control points (GCP) are measured in the field [e.g. by DGPS]. Use of the GNSS/INS data collected during the flight can help the automate tie point extraction. As already stated, the accuracy of such navigation data is normally not good enough to allow direct geo-referencing of UAV imagery. However, if quick delivery of results is more important than metric accuracy and there is no time or it is difficult to measure GCPs, as it might happen in mapping during emergency response, navigation data can be used for roughly georeferencing the block.

As outlined in the previous section, direct georeferencing of UAS imagery would be a great improvement that would increase the attractiveness of UAS photogrammetry. Think for instance of the cases where it is not possible to place GCPs in the area of interest, especially in the case of remote or inaccessible areas, such as rock faces or landslides. To this aim, it is clear that the major step as far as position is concerned is an RTK (or an equivalent post-processed kinematic) GPS solution using carrier phase differences. What kind of improvement would be required for IMU measurements (today typically made with cheap Micro Electro Mechanical Systems (MEMS) sensors) should be investigated. Given the low relative flying elevation of UAS, the accuracy would be a fraction of that necessary for aerial photogrammetry and much could also depend on the formulation and implementation of the Extended Kalman Filter. However, taking into account that automatic block orientation can be safely be given for granted in almost all circumstances, GPS-assisted aerial triangulation [2, 43, 65] might well be enough. The integration of GPS antenna positions in the bundle block adjustment, named Photo-GPS in its terrestrial version [45], has been used for some time in aerial photogrammetry, before aided Inertial Navigation Systems became accurate enough for direct georeferencing. The use of GPS-assisted aerial triangulation is discussed in Section 4.5, using numerical simulations to evaluate the influence of random and gross errors on the accuracy of tie points.

Ground Control Points have been used to georeference and control aerial photogrammetric block for decades; a large body of empirical and theoretical studies were devoted to study their influence on the block precision and to optimize their number and distribution in standard rectangular block with 60%-20% overlap [70]. Likewise, the reliability theory was applied to find the optimal distribution and number of tie point measurement capable to ensure gross error detection with given probability [71]. This body of knowledge was summarized in the bundle block adjustment by least squares, that provided the covariance matrix of the unknown parameters and of the residuals for hypothesis testing and that is the core of block orientation in photogrammetry and therefore of any photogrammetric BBA program.

It should be noted, however, that software programs for image orientation developed in a CV background the BBA is mostly performed without introducing GCP i.e. in the so-called free-net mode. Block georeferencing is obtained by applying a simple Helmert transformation based on the GCP from the arbitrary reference of the BBA to the object reference system. This of course underestimates the block deformations that might arise from weaknesses of the image network as well as systematic image errors, neglecting the experience accumulated with aerial blocks.

Both SfM and traditional Photogrammetry use the bundle adjustment to obtain the orientation in Euclidean geometry. They differ in whether the control data are within the BA process (as in photogrammetry [71]), or after BA in the form of a separate coordinate transformation (as in the SfM approach). In the first case, control measurements are within the bundle adjustment, so they represent ‘external’ observation to the image set that must be satisfied in the process of adjustment. Likewise, features on images and their corresponding matches represent ‘internal’ observation to the image set, which also need to be satisfied. Thus, the traditional photogrammetric approach, including control measurements in the bundle adjustment represents a minimization under independent inner and external constraints, which, together, determine the shape, scale and orientation of a 3D model [69]. On the contrary, the SfM approach use fewer control points since the 3D model is built with inner constraints only. Therefore control data are used to scale and orient the model in a global reference system, but do not contribute to decrease (control) any distortion of the model shape. The influence of block georeferencing through free-net adjustment and Helmert transformation on the accuracy degradation and on the residual deformations in UAS photogrammetric blocks is examined in depth in Chapter 4 through a series of Monte Carlo numerical simulations.

3.5.3. Dense image matching and 3D reconstruction

The 3D reconstruction from imagery is today primarily intended as the generation of a dense point clouds for 3D modelling and orthophoto generation. Once the block orientation parameters have been determined in the BBA, dense image matching techniques are applied to densify the initial object surface description given by the tie points.

In general, a dense image matching procedure aims at the exploitation of the entire information in the captured images, by systematically scanning a reference image (master) and looking for correspondences in the search image, rather than just looking for sparse and well-distinguished features points, as it is the case in image orientation. In computer vision, image matching is often called the stereo correspondence problem [118]. Image matching requires the establishment of correspondences between primitives extracted from two or more images, along with the determination of the 3D coordinates of matched feature points by a collinearity or projective model. In image space, this process produces a disparity map that assigns relative depths to each pixel of an image. The corresponding outcome in object space is the 3D point cloud. Considering an image pair, the disparity (or parallax, that is, horizontal discrepancy) is inversely proportional to the camera-to-object distance.

The distinction of image matching algorithms refers to the utilised primitives, namely, image intensity pattern as Area Based Matching (ABM) or to features leading to Feature Based Matching [100]. FBM is often used as an alternative method or combined with ABM. Compared to ABM, FBM techniques are less sensitive to image noise, more flexible with respect to surface discontinuities, and require less approximate values. The accuracy of FBM is limited by the accuracy of the feature extraction process. Furthermore, since the extracted features are sparse and irregularly distributed, the matching results are sparse point clouds and post-processing procedures like interpolation need to be performed.

ABM, also called signal-based matching, is the more traditional approach. It is justified by the continuity assumption, which asserts that at a certain level of resolution where image matching is performed, most of the image window depicts a portion of a continuous and planar surface element. Therefore, adjacent pixels in the image window will generally represent contiguous points in object space. In ABM, each point to be matched is the centre of a small window of pixels (patch) in a reference image (template) which is statistically compared with an equally sized window of pixels in another (master) image. The measure of match is either a difference metric that is minimized, such as RMS difference, or more commonly a similarity measure that is maximized. ABM is usually based on local square or rectangular windows. In its oldest form, area-based image matching was performed with cross-correlation and the correlation coefficient as a similarity measure. Cross-correlation works fast and well if the patches contain enough signal without too much high-frequency content (noise) and if geometrical and radiometric distortions are minimal. To overcome these problems, image reshaping parameters and radiometric corrections were considered, leading to the well-known nonlinear least squares matching (LSM) estimation procedure [56]. The location and shape of the matched window is estimated with respect to some initial values and computed until the grey-level differences between the deformed patch and the template one reach a minimum. Multiphoto geometrically constrained (MPGCs) matching [10] introduced additional constraints into the image matching and the surface reconstruction process.

ABM, especially the LSM method with its subpixel capability, has a very high accuracy potential (up to 1/50 pixel) if well textured image patches are used. Disadvantages of ABM are the need for small search range for successful matching, the large data volume which must be handled and, in the case of LSM, the requirement of good initial values for the unknown parameters, although this is not the case for other techniques such as graph-cut [112]. Problems occur in areas with occlusions, areas with a lack of or repetitive texture, or if the surface does not correspond to the assumed model (e.g., planarity of the matched local surface patch).

The image-matching problem is nowadays solved using stereopairs (stereomatching) [67, 59] or via identification of correspondences in multiple images (multi-view stereo – MVS) as in [30, 48, 51, 100, 122].

On the basis of the correspondences research technique, according to [118] the dense image matching distinguished in local or global methods. The local method searches correspondences points in a small area of the two images, depending on the algorithms, some methods use a function of distance or similarity applied to a small window of points, others consider the single point, still others a set of points.

Instead global methods consider the problem of finding the correspondence as a minimization problem of an energy function overall, based on the entire image. Usually the algorithms global consider the whole image as a graph and use approximate strategies to minimize the energy function, since an exhaustive search of the minimum would be too onerous from the computational point of view. The quality of results obtainable with global methods is usually higher than that which the algorithms of local type one, even if the latter are decidedly more simple from the point of view algorithmic and more efficient in terms of execution time. Furthermore, local methods, by definition, can easily be optimized for parallel processing, becoming even more efficient on some hardware architectures.

The point clouds, generated by local or global method, need to be afterwards structured and interpolated, maybe simplified and finally textured for photo-realistic visualization [85]. Dense point clouds are generally preferred in case of terrain/surface reconstruction (e.g. archaeological excavation, forestry area, etc.); while a reduction of dense point cloud in a sparse cloud which is afterward turned into simple polygonal mesh is preferred when modelling man-made objects like buildings or for photo-realistic visualization.

For the creation of orthoimages, a dense point cloud is mandatory in order to achieve precise ortho-rectification and the complete removal of terrain distortions. Due to the high density of the produced point clouds, the orthoimage generation is simply based on an orthographic projection of the results. The orthoimage resolution is calculated according to the 3D point cloud density and to the ground resolution of the aerial image.

Chapter 4
A simulation study on georeferencing UAV blocks

4.1. Introduction

Though embraced also by small surveying and photogrammetric companies, the use of UAV systems as a photogrammetric data acquisition platform is also fast spreading outside the traditional domain of well-regulated and established aerial photogrammetry: many companies offering UAV surveys are founded by young information technology, telecommunication or computer science engineers, with very little or no background in mapping and a rather strong one in CV.

While in aerial photogrammetry the nature of the cartographic products and the prescriptions in tenders where tightly dependent on map scale and therefore well established, UAV photogrammetry is not primarily devoted to map making (though the relative size of this topic on UAV applications might be growing). Constraints on maximum flight altitude above ground means that the image scale range is limited and that relative image scale variation might be larger than in most aerial images, at least in mountain environment or in city centres (provided this will be allowed). This does not amount to any fundamental change with respect to aerial photogrammetry, however focussing on UAV photogrammetry characteristics is worth, to develop or to reengineer methods and techniques for block orientation to improve or ensure survey quality and cost effectiveness. In particular, given the incorporation of SfM techniques in the block orientation pipeline, it is interesting to verify whether the aerial photogrammetry rules for block planning and orientation still apply. This means to investigate the influence of automatic tie point extraction and of the large overlaps between strips used in drone blocks, as to evaluate the accuracies of block adjustment. A second topic is the performance of techniques for block georeferencing, namely Ground Control Points, on one hand and GPS-Assisted Aerial Triangulation or Direct Georeferencing, exploiting methods and navigation instruments suitable for this purpose, on the other hand.

This Chapter devotes one section to each of the above mentioned issues, that are examined by means of using a series of Monte Carlo (MC) simulations, namely:

a) Accuracy of different procedures for BBA using GCP;
b) Accuracy of GPS-Assisted Aerial Triangulation.
c) Robustness and reliability of UAV blocks with respect to gross errors in on-board GPS positioning.

The simulations are carried out on two basic block shapes: a square block in a) and a rectangular block in b) and c).

4.2. BBA procedures for UAV blocks with GCP

Today every program package for UAV photogrammetry uses algorithms of automatic orientation built around SfM. The flow-chart of these programs, either born in CV or in a photogrammetric environment, is essentially identical. However, three main differences can be highlighted:

- the use of self-calibration (see Section 3.5.1);
- the solution of the least squares BBA normal equation system that is performed typically with the Gauss-Newton method in photogrammetry and with Levenberg-Marquart method in CV;
- the way block georeferencing and block control are enforced.

Block georeferencing and block control are performed in photogrammetric adjustment programs with the inclusion in the collinearity equation system of the BBA of the GCP information, so that GCP control the extent of the block deformation. To the contrary, CV software typically first executes the BBA in an arbitrary reference system (a sort of Free-Net adjustment [54]); then a rigid 3D Helmert transformation between the arbitrary system and the mapping system is computed using the GCP as double points; finally, the Helmert transformation is applied to the coordinates of the tie points (TP) and to the EO parameters. In either cases, photogrammetry or CV, georeferencing is also possible using information from the telemetry data of drone flight, should they have adequate accuracy. In particular, the projection centres can be related to GPS antenna positions and included in the BBA as in GPS-Assisted Aerial Triangulation, or telemetry data referred to projection centres can be used in CV to estimate the Helmert transformation.

Therefore, the CV BBA does not include the information on GCP in the minimization of the bundle. This means that any deformations related to the accumulation of random errors or to the presence of systematic errors are not checked, i.e. maintained within a certain limit. The subsequent similarity transformation certainly will be able to absorb part of deformations but may not be as effective as the photogrammetric procedure. In fact, the magnitude of such deformations, although generally neglected, depends on many parameters and can be ten times or more large than the ground sample distance as reported in [87]. Major deformations could arise with a weak or a ill block geometry design, as for examples elongated objects imaged in a single strip (roads, river banks, walls or dykes), or even in scenes with large planimetric dimensions but a small depth. This weakness can be contrasted by acquiring images at least in three parallel strips in order to constrain the rotation around the mean strip axis, and/or to use high forward and side overlap or to set a well distributed GCP network on the object. In fact, as well documented in [70], block accuracy and deformation control are a function of the number and distribution of GCP for nadiral aerial photogrammetry, as several studies performed with analogue square-format cameras blocks.

With different relative flight height, low quality digital compact cameras with different sensor formats, high forward and side overlaps, algorithms for automatic orientation and different BBA techniques (from CV and from photogrammetry, using GCP or GPS data on board) the world of UAV surveys is quite complex. It is therefore more difficult than it used to be in the past with analogue aerial cameras to optimize design of block parameters. Hence, the main interest is to understand the consequences of the transition from manual to automatic orientation (i.e. from Von Gruber points to uniformly distributed tie points) and the effect of the overlap percentages actually used with UAV on error propagation from the measures to the tie point ground coordinates in the BBA. Due to the importance of the transition from georeferencing with GCP to georeferencing with GPS on board, also highlighting the differences in accuracy and rigidity of blocks oriented with GPS on board is of interest.

Therefore, error propagation on tie points has been studied employing different georeferencing techniques for UAS photogrammetric blocks: GCP, free-net adjustment and GPS-assisted adjustment. To this aim, rather than a simple covariance propagation, Monte-Carlo simulations were used that consider, however, only the effect of random errors.

Effects of systematic errors have therefore not been taken into consideration in this work, to focus on georeferencing techniques. This does not mean that they can be neglected, in close-range photogrammetric blocks [28] as well as in UAV photogrammetric blocks. A recent study [69] indicates that the likelihood of systematic DEM error in UAV surveys can be reduced with some operational precautions. If using an accurate pre-calibrated camera, then self-calibration is not required and systematic errors should be negligible; if self-calibration is necessary, systematic error can be significantly reduced through the collection of oblique imagery that could reduce DEM deformation by one to two orders of magnitude.

4.3. Synthetic block generation and Monte-Carlo simulations

A .NET framework was developed in order to create a new or insert data from an existing photogrammetric block, run the MC simulations and perform data analysis. In Figure 4.3.1, the Monte Carlo simulations flowchart is shown.

In case of generation of a new block, the image block characteristics are specified using a fairly simple and intuitive configuration file where the user can describe the block structure (e.g., a single normal strip, a circular block with all of the images targeting a specific point or an area, a hemispherical distribution of camera stations, an unordered distribution of stations, a combination of above, etc. and the related forward and side overlap). Different object shapes can be defined procedurally or using a discrete set of 3D points: the points are then projected on the image frame and used as tie-points. Using a specified camera model, the pixel coordinates at which each 3D point would be observed in each image are then calculated, with small pseudo random noise added to account for measurement error. Errors in pixel coordinates were generated from a normal distribution with zero mean and a 0.5 pixel standard deviation, a magnitude representative of the precision of commonly achieved by image feature detectors in SfM software [14].

Thus, in every simulation sample, the same tie points are used and a new set of errors added.

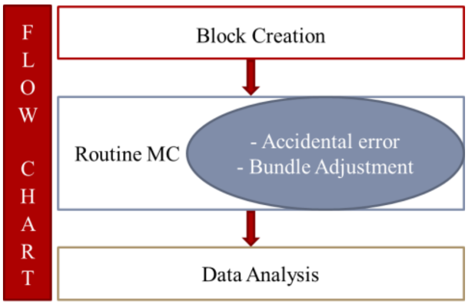

Figure 4.3.1 – Monte Carlo Simulation Flowchart.

The user can also specify how the ground control is provided (e.g., using a set of GCP, or using a free net bundle block adjustment [90], or constraining the camera poses and locations, GPS data, etc.). As previously discussed, various software packages address the reference system definition in different ways: CV-oriented packages use the set of GCP to estimate a seven-parameter transformation; others perform a free-net adjustment with additional constraints. Photogrammetric packages usually implement GCP constraints in the BBA.

A routine performs the inner cycle of the MC simulations adding the errors, executing the bundle adjustment and collecting the orientation solution and the estimated object structure (coordinates of tie points) of each iteration. The MC framework can be interfaced to several BBA routines. In particular, the CALGE BBA module [42], a widely tested scientific package, was considered the most versatile and efficient for the variety of block configurations in the different case studies. The simulations thus represent synthetic data processed with the same algorithms and the same workflow as real blocks.

At each iteration, the adjusted tie point coordinates are compared to the reference ones (error free) and the statistics are output for the data analysis, in tabular and graphic form.

Though a parametric study according to variables that might describe different forms of block would have been of interest, to limit the computing time it has been decided to study only one block type for each simulation:

a) a square block, shown in Figure 4.3.2, considered representative of generic UAV blocks, used for the comparison between BBA procedures in photogrammetry and CV, hereafter MC 1;

b) a rectangular block, shown in Figure 4.3.3, considered representative of a weak geometry for GPS-Assisted Aerial Triangulation, used for the error propagation from the GPS positions to the TP coordinates, hereafter called MC 2;

c) the same rectangular block MC 2, to study the precision of tie points as a function of on-board GPS precisions as well as the vulnerability to gross errors in the on-board GPS positions.

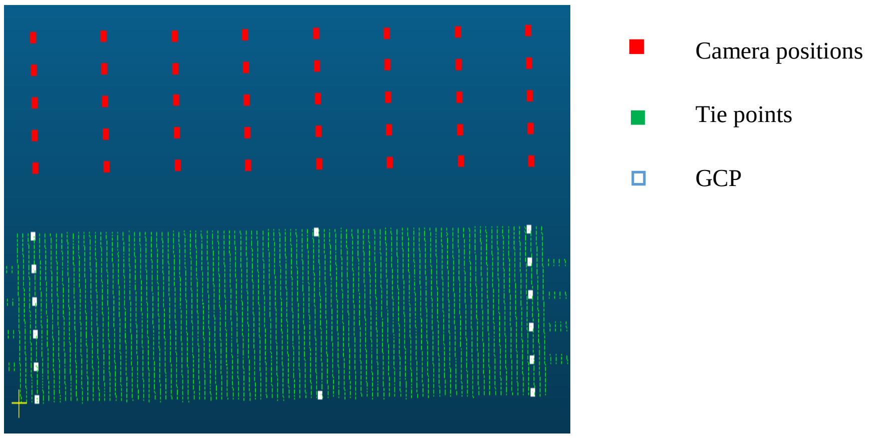

Figure 4.3.2 – Perspective view of the camera positions (in red), tie points (in green) and GCP (in white) for block MC 1.

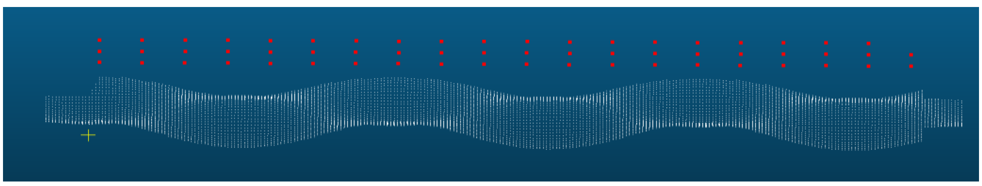

Figure 4.3.3 – Perspective view of the camera positions (in red) and of the terrain (in white) for block MC 2.

4.4. Simulation MC 1: accuracy of different BBA procedures

The simulation MC 1 aims to estimate the accuracy of the tie points obtained by the photogrammetric method against those obtained with the CV method, i.e. using GCP or using free-net adjustment with and without the 3D Helmert transformation estimation.

Furthermore, to investigate the influence of different levels of overlap between images and the multiplicity of tie points, two different configurations were created for the reference blocks, keeping as common parameters: 100 m relative flight height, a flat terrains area of 420 × 420 metres and the OI parameters. Also a common camera with a 4000 × 3000 sensor with 5 μm/pixel size and a 20 mm lens was hypothesized.

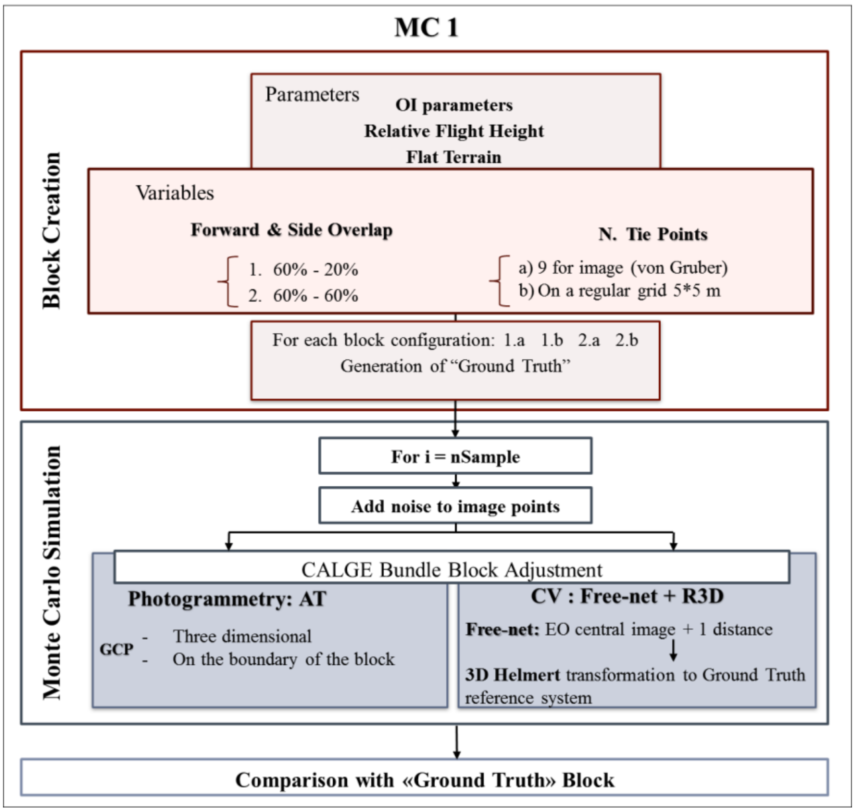

Figure 4.4.1 – Scheme of MC 1 simulation: parameters and variables of "Block creation", "Monte Carlo Simulation" with noise to image points of each sample and different techniques of BBA and the last "Comparison" step.

To discriminate the influence of overlap and of tie point density, as shown in Figure 4.4.1, forward was fixed to 60% while 1: side overlap of 20% and 2: side overlap of 60% were taken into consideration. Two distributions of tie points were considered: a) 9 points per image as with manual collimations on von Gruber bands in analog-analytical photogrammetry and b) points distributed on a 5 × 5 m regular grid (as in digital photogrammetry and CV). Combining the variables, four reference blocks were obtained: 1.a, 1.b, 2.a e 2.b. Maintaining the same object size, different levels of overlap produce different number of strips and images per strips, see Figure 4.4.2.

Each block was run for 2000 samples, with photogrammetric and CV adjustment. The first type of adjustment uses three-dimensional GCP located on the boundary of the block, according to aerial blocks rules. The second one executes a free-net adjustment constraining the position and the rotations of block central image and the distance between two ground points along a block diagonal, in an arbitrary reference system. Notice that the arbitrary reference is indeed compatible with the reference system (map system), since the EO elements of the central image are fixed to the true values in such system and likewise the scale is fixed 1:1 with the map system. Then a 3D Helmert transformation is estimated between the adjusted (erroneous) GCP coordinates in the arbitrary system and those in the reference (error-free) system (map system).

The features of the reference blocks run in MC 1 are summarized in Table 4.4.1, where for each case of study the number of photos, strips and tie points forming the blocks as well as the overlap and the BBA technique are reported.

Table 4.4.1 – Feature of blocks run in MC 1.

TEST	**Case**	**N. photos**	**N. strips**	**Forward Side Overlap (%) (%)**	**N. TP**	**BBA**	**N. Sample**
Photogrammetry vs. CV	1.a	40	5	60-20	134	Free-net	2000
					134	Free-net + R3D	2000
					134	GCP	2000
	1.b	40	5	60-20	8857	Free-net	2000
					8853	GCP	2000
	2.a	72	9	60-60	166	Free-net	2000
					166	Free-net + R3D	2000
					166	GCP	2000
	2.b	72	9	60-60	10251	Free-net	2000
					10233	GCP	2000

The 1.b and 2.b cases (60-20% and 60-60% overlap with high density of tie points) were oriented with GCP and with free-net adjustment only (without the 3D Helmert transformation). Indeed, because the high multiplicity of tie-points

produces errors comparable with the theoretical precisions, computing the transformation would not add any improvement.

It is interesting to note the variations of tie points number in case of von Gruber or regular grid, more evident in the subsequent Figure 4.4.2. It shows the block geometry of the 4 reference blocks as a function of number and distribution of tie points (black dots) and of levels of forward and side overlaps. As visible the GCP, green triangles, are located on the block boundary. The number of photos (represented by camera positions in blue squares) increases with increasing side overlap.

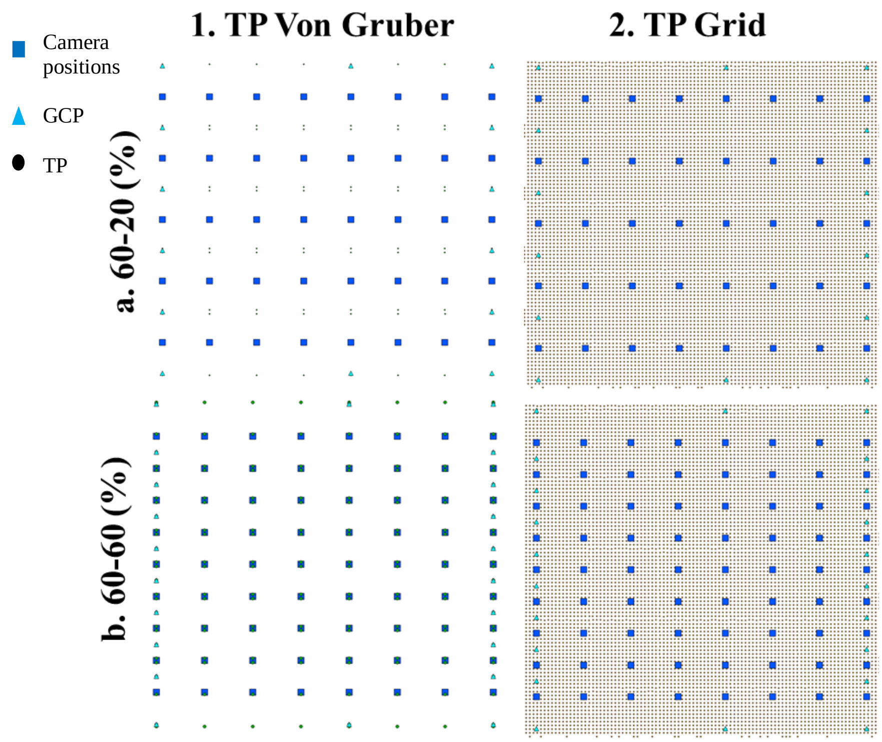

Figure 4.4.2 – Block geometry of reference blocks: 1.a, 1.b, 2.a, 2.b. The camera positions (blue square), tie points (black dots) and GCP (green triangles) are indicated.

4.4.1. Analysis of the results

The MC 1 simulation results are reported in Table 4.4.2 as mean square errors of the ground coordinates. It is immediately clear that photogrammetry behaves the same way with a few or with many tie points; moreover, errors are always smaller than those of CV. In particular, with 60-60% overlap and many tie points, the best result is obtained with 1 cm in planar coordinates and 2 cm in Z.

In the CV method, by applying the Helmert transformation, the largest part of the deformations is absorbed. In fact, considering the 2.b case (60-60% overlap and von Gruber tie points) the mean square errors in Z improves by 3 cm and at the same time evens out mean errors in planimetric coordinates to 2 cm.

On the other hand, with few tie points and 60-20% overlap (1.a case), even applying the Helmert transformation errors in Z remain relevant (16 cm) while the mean square errors in planimetric coordinates are in order of 3 cm.

On the contrary, with a dense grid of tie points, the deformations though present are limited both in case of 60-20% and in case of 60-60% overlap. Therefore, the block with many tie points were only adjusted in free-net.

Table 4.4.2 – Mean square errors (MSE) of the ground coordinates of the MC 1 simulations: in the upper part (blue rows) BBA with GCP, in the lower part (grey rows) results for the CV method before and after Helmert transformation (R3D).

Mean σ_{Dx}, σ_{Dy}, σ_{Dz}		**Forward Side Overlap (%)**	**von Gruber TP**					**TP Grid**				
			Case	**N. TP**	**σ_{Dx} (m)**	**σ_{Dy} (m)**	**σ_{Dz} (m)**	**Case**	**N. TP**	**σ_{Dx} (m)**	**σ_{Dy} (m)**	**σ_{Dz} (m)**
AT	**GCP**	60-20	1.a	134	0.01	0.01	0.03	1.b	8853	0.01	0.01	0.03
		60-60	2.a	166	0.01	0.01	0.03	2.b	10233	0.01	0.01	0.02
CV	**FREENET**	60-20	1.a	134	0.09	0.08	0.22	1.b	8857	0.02	0.02	0.04
		60-60	2.a	166	0.04	0.03	0.07	2.b	10251	0.01	0.01	0.03
	FREENET + R3D	60-20	1.a	134	0.03	0.03	0.16					
		60-60	2.a	166	0.02	0.02	0.04					

It is also interesting to look at the distribution of the error over the tie points. Here, however, the graphical representation must be different for case a and b. Indeed, considering the low number of tie points using only von Gruber bands, plotting the distribution of mean error in a continuous colour map would simply depict the chosen interpolation function, not real mean square errors due to excessive spacing of data. Hence, the colour maps of the coordinates mean square error were generated only for the blocks with many tie points.

Figure 4.4.3 and Figure 4.4.4 show the distribution of mean errors in Z with tie points distributed on a regular grid. Figure 4.4.3 shows the 1.b case with 60-20% overlap: on the left, the block oriented in free-net adjustment, on the right, the same block oriented with GCP. Instead, Figure 4.4.4 shows case 2.b with 60-60% overlap: on the left, the block oriented in free-net adjustment, on the right, the same block oriented with GCP.

Usually where there is higher multiplicity, namely in the areas of higher overlap, errors are lower. This means that indeed multi-ray points, as it should be, are actually better at avoiding random error combinations that affect the position all in the same direction (i.e. the probability to get a “nasty” error sample gets actually lower the larger the point multiplicity). This is an important indication (though a theoretically well known) that multi-image aerial photogrammetry, as far as random errors are concerned, has a still largely untapped potential.

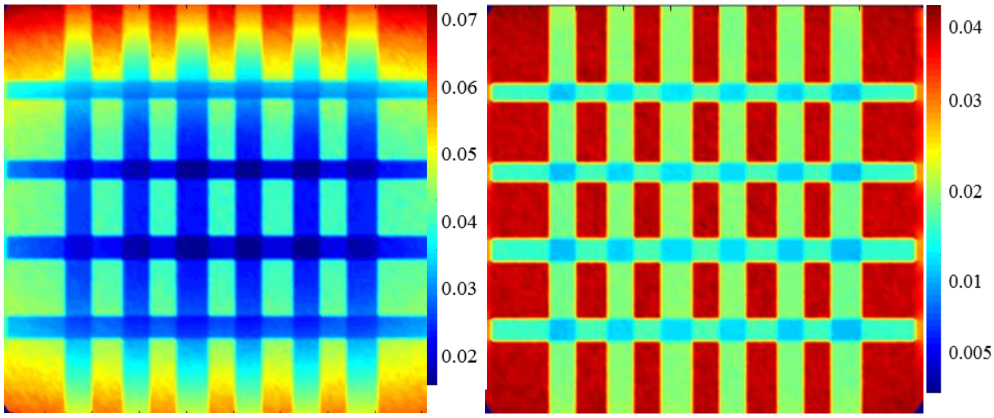

20% sidelap, Free-net *20% sidelap, GCP*

Figure 4.4.3 – Case 1.b: 60-20% overlap, tie point on a regular grid block oriented in free-net adjustment (on the left) and with GCP (on the right). Color map of the mean error distribution in Z. Note: color scales are different.

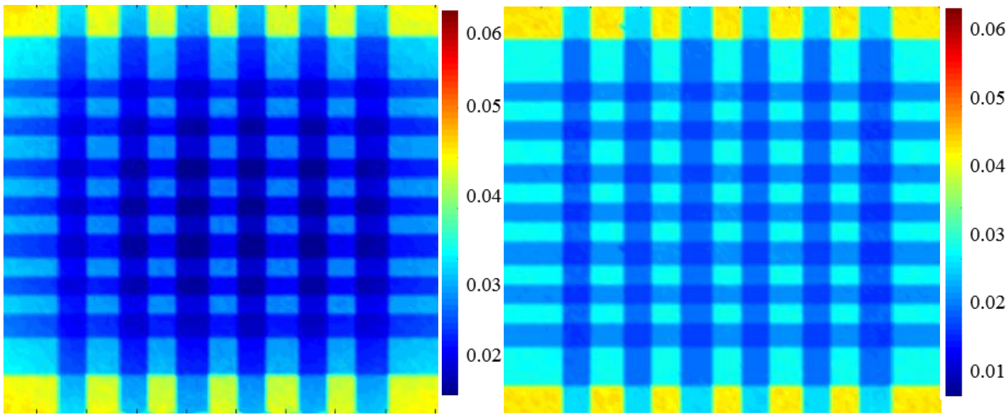

60% sidelap, Free-net *60% sidelap, GCP*

Figure 4.4.4 – Case 2.b: 60-60% overlap, tie point on a regular grid block oriented in free-net adjustment (on the left) and with GCP (on the right). Color map of the mean error distribution in Z. Note: color scales are (slightly) different.

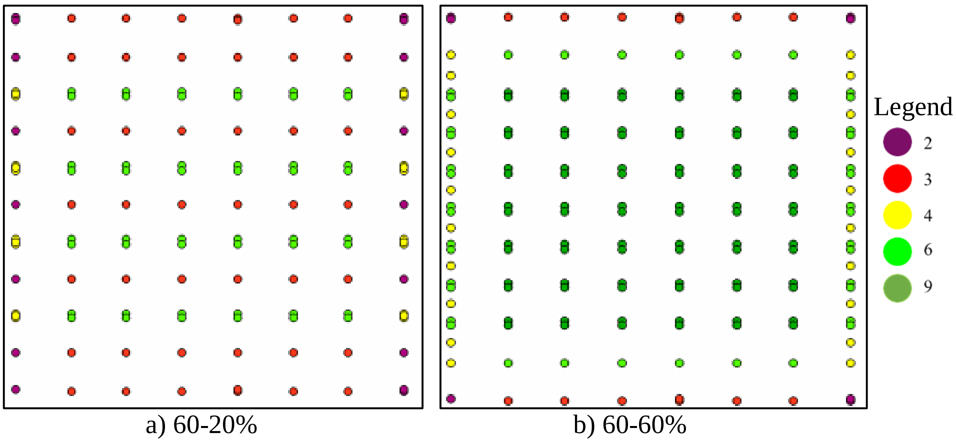

Figure 4.4.5 – Plot of tie point multiplicity on von Gruber bands: a) 60-20% overlap; b) 60-60% overlap. As shown in Legend the lower number is 2, indicated in purple, the higher number is 9, indicated in dark green.

The Figure 4.4.5 shows the multiplicity of von Gruber tie points in color maps respectively with 60-20% (left) and 60-60% (right) overlap. As expected, points located on the boundary of the blocks have a lowest multeplicity (2); on the other hand, the multeplicity increases gradually in the center of the block (up to 9 for the 60-60% overlap).

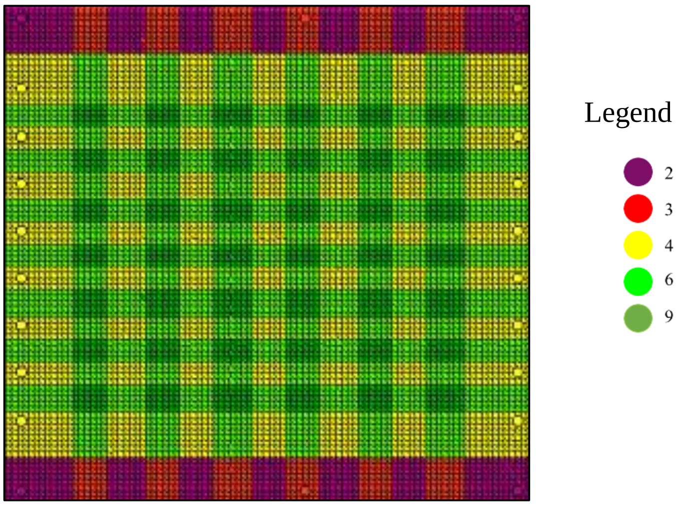

Figure 4.4.6 – Plot of multiplicity of tie points on a grid: in the case of 60-60% overlap. The lowest value is 2 (purple colour), the highest is 9 (dark green colour).

Figure 4.4.6 shows the color map of the multiplicity of tie points distributed on a grid in the 60-60% block. As expected, points located on the upper and lower boundary of the blocks have the lowest multeplicity (2), purple in the legend; on the other hand, the multeplicity increases gradually in the center of the block (with values of 9 for the 60-60% overlap). The identical pattern of this figure compare to the color map of the Z mean error of Figure 4.4.4. Clearly shows that the higher accuracy observed in the high overlap areas is due to higher multiplicity.

In conclusion, higher accuracy are obtained using GCP and forward and side overlap of 60-60%. The higher accuracy on Z is assured using the GCP orientation in whatever block configuration. On the contrary, the accuracy degrades strongly if few points are collimated, the overlaps are low and no GCP are used in the orientation.

Solutions with GCP and with CV methods show comparable values using many tie points, long as they are collimated on all images.

High multiplicity of tie points increases the precision of the bundle adjustment and provides greater rigidity to the block against random error unfavourable accumulation.

These results are in agreement with the Rosnell and Honkavaara experience [108], where a simulation study, based on experimental data, reveals that increasing the forward overlap from 80% to 90% clearly improved the accuracy of orientation parameters and point determination. Decreasing the number of GCPs decreased the accuracy. Furthermore, because of the data processing of UAS imagery, the results of the UAV-carried small-format camera were comparable to a large-format photogrammetric camera in relative point densities for automatically measured point clouds.

4.5. Georeferencing with GPS on board

The georeferencing with GPS on board, the so-called GPS-assisted aerial triangulation [124, 26], is another method to define the coordinate datum and control a photogrammetric block, as it has already been discussed in Section 3.4.2.

It is a topical theme for UAS photogrammetry: the capability to use the GPS positions at shooting time of images for georeferencing block is a useful solution from the point of view of time and cost of the survey, especially for periodic control surveys. In fact, georeferencing in a given reference system is normally required in surveys or, as in periodic control surveys, an arbitrary but stable reference system is required. Thus, a surveying campaign for the measurements of GCP with GPS or total stations is usually executed, possibly implying the materialization and maintenance of the GCP or of the reference stations. Manual collimation of the control points on the images is necessary for block adjustment: this is today the only manual operation of the orientation pipeline. However, it is not always possible to place the GCP in the area of interest, especially in the case of remote or inaccessible areas, such as rock glaciers, landslides, etc. Using GPS RTK measurements of on-board navigation instruments pursues the goal of direct georeferencing or at least of GPS-assisted aerial triangulation. Indeed, given the performance of SfM, getting rid of Aerial Triangulation is not really so important in the economy of a photogrammetric project. So, unless a real-time solution is needed, direct orientation as opposed to indirect GPS-assisted AT, as Friess demonstrated already in 1986 [47] does not bring significant advantages in terms of accuracy on ground. Progress in GPS receivers miniaturization and possibly a larger market for L1/L2 that might further reduce costs both mark a steady move towards this georeferencing technique to become a standard.

Operationally, at each shooting, the antenna position is recorded by the receiver. It is not necessary to obtain GPS positions for each camera station, though this would increase the reliability of GPS and the overall block control. The GPS receiver operates in kinematic mode. If images are acquired in motion, however, as in most UAV, the shooting time must be recorded and the position interpolated over time. In both cases, to use this information in the bundle block adjustment, the mathematical model of the collinearity equations has to be extended to account for the offset between the camera centre and the antenna. The GPS position is referred to the antenna phase centre or to the antenna mount point. Being the camera centre fixed with respect to the antenna, the offset is constant and can be determined by calibration. The GPS data collected by the receiver can processed according to available instrumentation. RTK mode with respect to a locally set master station or to a network (NRTK mode) allows immediate verification of the quality of positioning. Otherwise, kinematic post processing with respect to a nearby master or to a Virtual Reference Station (VRS) with Virtual Rinex (VRX) data generated within a network of GPS permanent stations can be used. A RTK network allows using just a single GPS receiver (the rover). Moreover, the survey is not bounded by the distance to the master. The VRX files [58] can be processed with any GPS software. A calibration is necessary to determine the relative position between camera and antenna to insert the camera positions in the bundle block adjustment [46].

The automation potential of this technique is high, if a specific software pipeline is set up. The bundle block adjustment would then follow GPS data processing and the automatic generation of tie points by SfM algorithms without need for manual collimations.

If GCP are not used, however, the stability of the reference system in periodic surveys depends on the accuracy of GPS measurements and on the spatial distribution of the camera stations. With objects mainly developed in height or in width (i.e. building façades, walls, fronts of landslide), the shooting of two or more strips at different elevations or at different distances from the object is recommended. As a rule of thumb, an accuracy of kinematic GPS surveys in the 1-2 cm range can be achieved; sub-centimetre accuracies, if necessary, are much harder to guarantee.

Georeferencing with GPS on board consists of including in the mathematical model of the collinearity equations (Eq. 3.2.1 – Eq. 3.2.2), adding the observation equation relating camera centre and antenna phase centre position [43]:

$$X_a = X_0 + R_c^G\, e + S + Dt \quad \textbf{(4.1.)}$$

Where X_a antenna phase centre;

X_0 camera perspective centre;

R_c^G image attitude matrix (from camera to object system);

e eccentricity vector, expressed in the camera system;

S, D shift and drift parameters;

t the shooting time of the image.

Drift parameters are supposed to mitigate systematic discrepancies between the GPS and photogrammetric solutions on a block basis or on a strip-by-strip basis.

In this work the shift and drift parameters are not included in the mathematical model when GPS-assisted aerial triangulation accuracy was evaluated.

In the equation (4.1) the offset vector e is known by calibration while the perspective center and the attitude matrix R_c^G are unknown. The precision of the antenna position is in principle available from the GPS data processing. Individual weights can be assigned to camera stations accounting for the actual PDOP values. However, these estimates are often unrealistically good. A way to tackle this difficulty is to rescale the precision estimate to a realistic magnitude based on practical experience of kinematic GPS surveys. Another possibility is assigning the same precision to every station, again based on practical experience; this however ignores the fact that satellite configuration changes and cycle slips due to obstructions may affect the actual precision (as well as the accuracy) from one station to the next during the survey. This is indeed mostly a characteristic of ground kinematic GPS surveys, where just moving a few meters might lead to loss of lock to one or more satellites, with strong variations of the PDOP, due to obstacles. However, this might apply to UAV as well, at least during turns for fixed wings.

In the block adjustment SfM algorithms provide the tie points and their accuracy. On the other hand, the GPS provides the positions of the antenna-camera stations and their accuracy as well as the reference system of the block. Thus, the GPS data substitute for GCP in georeferencing. However, in general, the antenna positions cannot be considered error-free or sometimes even as accurate as photogrammetry. To achieve cm-level accuracy in a GPS kinematic survey it is critical to fix the so-called integer ambiguity [45]. In turn, this capability depends on satellite configuration, receiver hardware and software and environment conditions. A poor PDOP, just a few satellites tracked, frequent changes in satellite constellation make it difficult to estimate with enough confidence the integer value. So do radio interference, multipath, obstacles to satellite view in the near and far range such as buildings or mountain slopes. In such circumstances, the hardware and software characteristics of the receiver can make the difference. For the above mentioned reasons, therefore, GPS positions must be treated as additional observations and not as ordinary control points.

To investigate the accuracy requirements to the GPS positions and their vulnerability to gross errors, a second series of Monte Carlo simulations, denominated MC 2, was executed. In the following MC 2 simulation will be presented and discussed together with tests on the precisions of tie point coordinates as a function of GPS position errors, including gross errors, for GPS-assisted Aerial Triangulation.

4.6. Simulation MC 2: accuracy of GPS-Assisted Aerial Triangulation

The simulation MC 2 aims to estimate the accuracy of tie points in a block oriented by GPS-assisted aerial triangulation. As previously pointed out, it involves an elongated rectangular block (see Figure 4.3.3), that represents a case with a weak geometry for the adjustment with the GPS data on board. The terrain simulated with a sinusoidal shape with an amplitude of 10% of the relative height flight (100 m) on a regular 5 × 5 m grid.

The features of the simulation are shown in Figure 4.6.1. In this case, in addition to tie point image coordinates, also GPS positions are affected by noise in each iteration of the MC routines. Here GPS positions are the only useful information for georeferencing.

A single strip, as is the case of surveys of river beds or map production for road projects, cannot be oriented by GPS on board only. In fact, in this case the rotation of the entire strip around the direction of flight is ill-defined. To avoid this, if measuring GPC is ruled out, the alternative is to enlarge the block by flying two additional parallel strip, one above and one below, with a convenient side overlap. This latter option has been adopted for the simulation, with a 60% sidelap. The area of interest of the simulation is 1.2 km long and 200 m wide. Hence, with a 60% forward overlap, the reference block is composed by 60 images on 3 strips. The inner orientation parameters are the same as the previous simulation MC 1. As for the average errors of the GPS, 3 cm on planimetric coordinates and 5 cm on elevations were assigned. How good RTK position accuracy might be is for obvious reasons difficult to verify in dynamic conditions. Therefore, these conservative values, that are widely obtainable with good satellite configurations in kinematic surveys on the ground, have been selected for random error generation.

As previously, errors are computed by comparison of the estimated tie point coordinates of each iteration with those of the reference block. The MC cycle has been repeated 5000 times.

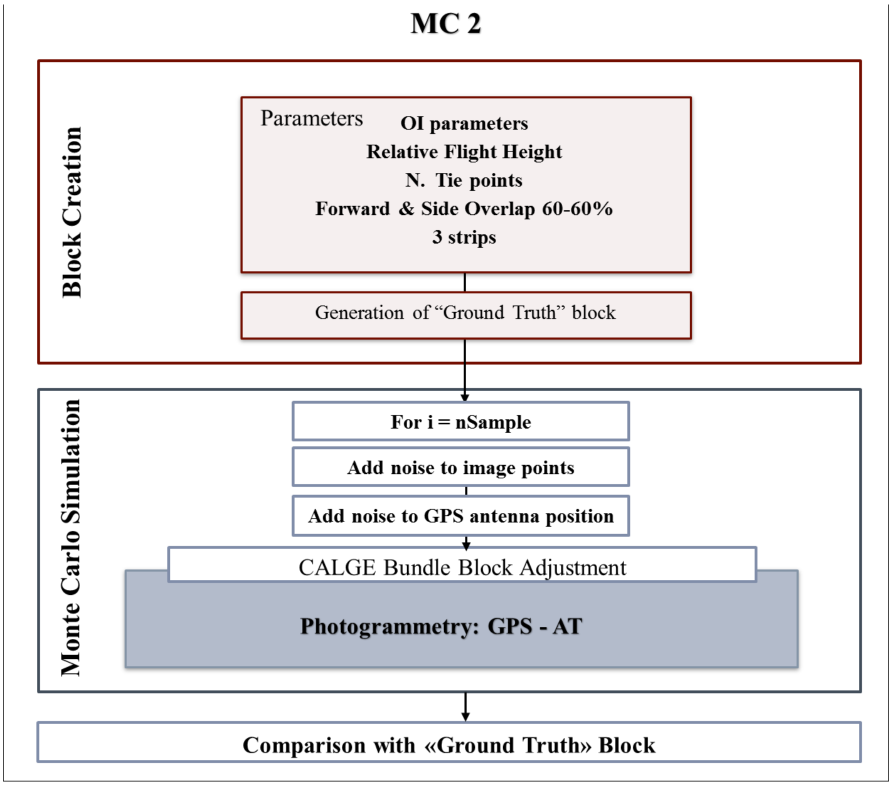

Figure 4.6.1 – Scheme of MC 2 simulation with parameters of "Block creation" step, "Monte Carlo Simulation" with noise added to image points and GPS antenna positions for orientation using GPS-AT and the last "Comparison" step.

4.6.1. Analysis of the results

The MC 2 simulation results are reported in Table 4.6.1 as minimum, maximum and mean square errors of the ground coordinates for the 5000 blocks oriented.

It should be noticed that these values account for both the image and the GPS position errors, so they look indeed quite good. Again, it should be stressed that this applies to tie points with a good average multiplicity, at least in the central strip. If we compare the mean square errors of ground coordinates of Table 4.6.1 with the theoretical precision (i.e. the precision from the estimated covariance matrix of the l.s. BBA) of a UAV block adjusted with ground control points we find a good agreement.

Table 4.6.1 – Minimum, maximum and mean square errors of the ground coordinates of the MC 2 simulations.

	N. of Samples	min	MAX	mean
$\boldsymbol{\sigma_{Dx}}$ (m)	5000	0.009	0.054	0.014
$\boldsymbol{\sigma_{Dy}}$ (m)	5000	0.018	0.038	0.025
$\boldsymbol{\sigma_{Dz}}$ (m)	5000	0.013	0.079	0.030

Table 4.6.2 reports such precisions for the square block of MC 1: the agreement is very good, except for the y coordinate, which is less precise in the three-strip rectangular block. This can be expected, since the Y direction is still affected by the residual ill-geometry of the block, not completely corrected by the two external strips. However, this means that a UAV block controlled by GPS on board with cm level precision delivers ground coordinates with cm level precision on a par with blocks controlled by GCP.

Table 4.6.2 – Theoretical precisions of ground points in square blocks oriented with GCP.

Theoretical precisions	RMS
σ_X (m)	0.014
σ_Y (m)	0.010
σ_Z (m)	0.029

Figure 4.6.2 shows the colour map of the mean square error distribution for each ground coordinate. It is apparent that the central strip, where point multiplicity reaches 9 has the best precision and is the most uniform; on the contrary, the lateral strips suffer some border effect. Therefore, employing 3 strips delivers more homogeneity to the central strip, the one that actually covers the area of interest.

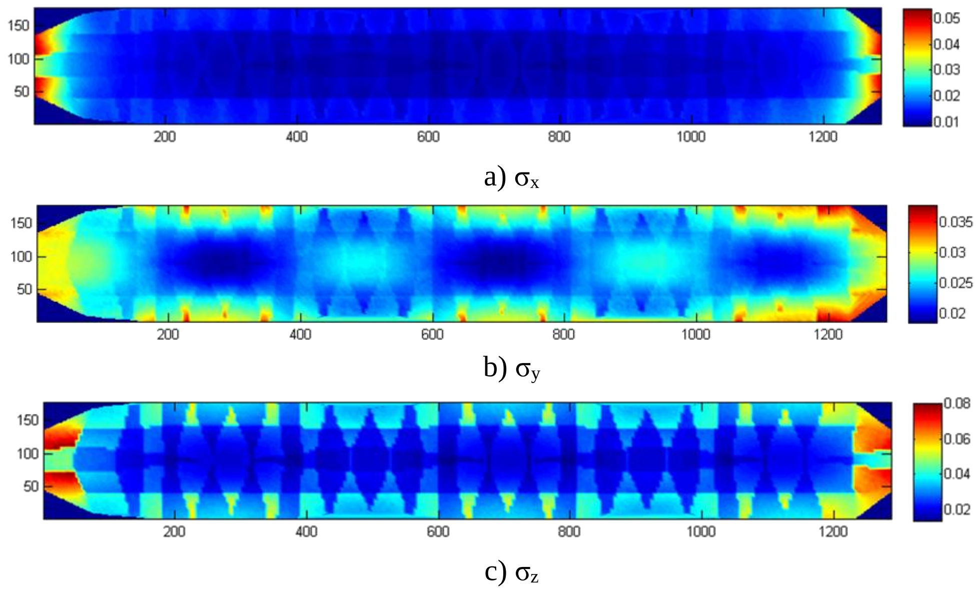

Figure 4.6.2 – Color map of the mean square error distribution of ground coordinates of the MC 2: a) σ_x, b) σ_y, c) σ_z.

4.7. Required precisions of GPS and sensitivity to gross errors in GPS positions

The Monte Carlo simulations allowed to account for random errors on block georeferencing with GPS on board. However, two questions are still worth investigating: which category of receiver is required to achieve an assigned precision on the ground coordinates? How much might gross errors (of constant type or of time-variant type) affect the BBA results? How effective is gross error detection in such cases?

To study both issues, one of the three-strips blocks of the previous simulations, containing random errors both on image coordinates and GPS data, was used.

4.7.1. GPS data precision requirements

If soon GPS on board will replace GCP on ground as a mean to georeference UAV blocks, it is worth to find out whether this is going to happen with a loss of precision for ground coordinates (the remarks on Section 4.6.1 hint that this should not be the case). A related question might be what is the ceiling in precision we can get: today improvements can be achieved increasing the GCP density and precision; is this possible with GPS on board as well?

To have reference values of precision (computed from the covariance matrix of the BBA), the block of 3 strips has been oriented first with 3 pairs of GCP located in pairs at the strip ends and in the middle of the block. Then a new block orientation, with GPS data only, has been performed using GPS precisions of 3 cm for planimetric and 5 cm for altimetric coordinates (as in the simulations).

Table 4.7.1 and Table 4.7.2 show the average (RMS) theoretical precisions of adjusted ground coordinates, respectively for georeferencing with GCP and with GPS. The mean values are quite similar, i.e. the quality of block control is equivalent. A partial exception is the Y coordinate, which is better in the case of adjustment with ground control because the GCP can compensate for the weakness (asymmetry) of the block geometry in this direction. Thus, the solutions are almost equivalent: the GPS assisted AT works well thanks to high side overlap (60%) and the two lateral strips that join the central one. It should be noticed, however, that the estimated precision for the GCP case have been computed assuming the GCP coordinates error-free. With static GPS measurements (not really the norm with UAV blocks) a GCP accuracy of 1 cm can be assumed. Therefore treating GCP coordinates as error-free might be justified only for GSD larger than 5-6 cm.

Table 4.7.1 – Orientation with GCP: Theoretical precisions on ground coordinates.

Theoretical precisions	RMS	MAX
X (m)	0.014	0.051
Y (m)	0.013	0.027
Z (m)	0.033	0.078

Table 4.7.2 – GPS assisted aerial triangulation (σ_x,σ_y :3 cm, σ_z:5 cm): Theoretical precisions on ground coordinates.

Theoretical precisions	RMS	MAX
X (m)	0.015	0.054
Y (m)	0.025	0.038
Z (m)	0.032	0.079

The other question is what is the relationship between the GPS data precision and the ground coordinate precision. As a matter of fact, given the difficulty to reliable estimate GPS precision, this point highlights a potential weakness of GPS-assisted AT, i.e. the dependence of the solution on the weights assigned to GPS observations. To find out, the three-strip block has been adjusted varying GPS precision (see Table 4.7.3, the light blue rows) to reach a comparable Y precision with that of GCP adjustment. Starting with values as 5 cm in Z and 2.5 cm in X and Y, the GPS precisions are improved up to 3 cm in Z and 1.5 cm X and Y.

As it can be seen, even with these last precisions (values that are not so easy to guarantee even with geodetic receivers) a precision comparable to the GCP solution in Y direction cannot be obtained. This implies that if there are asymmetries in the coordinate precision due to block shape, they cannot easily be solved by on board GPS data.

Conversely, supposing to use e.g. lower quality L1 only receivers, if lower precisions (from 70 mm up to 150 mm in Z) the precisions on the ground coordinates get obviously worse, though they still remain interesting in absolute terms for many applications. The real limit of the L1 receivers is, however, the time required to fix the integer ambiguity in the case of cycle slips, which can be of several minutes and therefore incompatible with the duration of drones flight, unless the possibility of cycle slip occurring during the flight is ruled out in some way.

Table 4.7.3 – Precisions on ground coordinates using different precision of GPS data w.r.t. control with GCP: in light blue the Geodetic category (σ_z: 30-50 mm) is indicated; in green the Low-Cost category (σ_z from 150mm) is indicated.

		Geodetic Receiver			Low-Cost Receiver			
6 GCP	**σ_z GPS (mm)**	**30**	**40**	**50**	**70**	**80**	**100**	**150**
	$\sigma_{x,y}$ GPS (mm)	**15**	**20**	**25**	**35**	**40**	**50**	**75**
13.99	σ_x (mm)	13.32	13.98	14.68	16.16	16.93	18.51	22.57
13.28	σ_y (mm)	17.99	21.2	24.66	32.01	35.83	43.61	63.54
33.09	σ_z (mm)	29.24	30.4	31.78	35.03	36.84	40.74	51.54

Ultimately, to achieve the same value precision of tie points with ground control, the precision of GPS data required is normally achievable only with receivers of geodetic (of good quality).

Another interesting point from Table 4.7.3 is that the estimated precision of ground coordinates changes slowly with varying GPS data precision, though with different paces for the different coordinates. Indeed, in X and Z direction the loss of accuracy is about 70% of the best value; in Y direction the effect is stronger (about 250%) because the weakness in that direction increases with less tight control “from above”.

4.7.2. Vulnerability to gross errors

The incorrect fixing of the integer ambiguity, an event that might well happens in RTK positioning, as well as or the sudden change of constellation in view produce systematic errors in the trajectory. Such errors can be modelled by constant shifts or as time-dependent incremental error (drifts) as in (Eq. 4.1.), where normally these parameters are applied on a strip-by-strip basis.

On one hand, it is important to evaluate the block robustness in such circumstances; on the other hand, it is interesting to know what entity of errors is correctly pinpointed by the data snooping, i.e. the test on normalized residuals.

Several tests were run with the CALGE BBA module in order to estimate the influence of these errors on the block adjustment. Shift and drift errors of different size were applied to the central or to one of the lateral strips of the block (3 strips, 60-60% forward and side overlap, GPS precisions of $\sigma_{x,y}$:3 cm, σ_z:5 cm).

No rejection of outliers has been performed: therefore, the corrections to the coordinates represent the effect of the random and gross errors introduced, unless otherwise specified.

4.7.2.1. Shift errors

As far as shift errors are concerned, the Table 4.7.4 resumes the error input to the coordinate of the antenna centres of the central strip (left) and of the lateral strip (right).

Table 4.7.4 – List of combination of Shift errors on antenna coordinates input in the GPS-assisted AT. Central strip errors (left); lateral strip errors (right).

	Central strip			**Lateral strip**		
	DX	**DY**	**DZ**	**DX**	**DY**	**DZ**
CASE	**(m)**	**(m)**	**(m)**	**(m)**	**(m)**	**(m)**
1	0.08	0.08	0.08	0.08	0.08	0.08
2	0.10	0.10	0.10	0.10	0.10	0.10
3	0.10	0.10	0.15	0.10	0.10	0.15
4	0.12	0.12	0.12	0.12	0.12	0.12
5	0.12	0.12	0.15	0.12	0.12	0.15
6	0.15	0.02	0.15	0.15	0.02	0.15
7	0.20	0.20	0.20	0.20	0.20	0.20
8	0.20	-0.20	0.20	0.20	-0.20	0.20
9	-0.15	-0.15	-0.15	-0.15	-0.15	-0.15
10	-0.20	0.20	-0.20	-0.20	0.20	-0.20
11	0.15	0.20	0.20	0.15	0.20	0.20
12	0.25	0.25	0.25	0.25	0.25	0.25
13	-0.25	-0.25	-0.25	-0.25	-0.25	-0.25
14	-0.25	-0.20	0.20	-0.25	-0.20	0.20
15	-0.20	-0.25	0.20	-0.20	-0.25	0.20
16	-0.25	-0.25	-0.30	-0.25	-0.25	-0.30
17	0.30	0.30	0.30	0.30	0.30	0.30
18	-0.30	-0.25	-0.30	-0.30	-0.25	-0.30
19	-0.30	-0.25	0.30	-0.30	-0.25	0.30
20	0.30	0.25	-0.25	0.30	0.25	-0.25

In the 20 combinations, Shift errors were increased in size from about 3 times to about 10 times the standard deviation of “correct” GPS observations and varied in sign.

The results of these 20 simulations show the same behaviour. In general, the shift errors imposed on the lateral strip produce more corrections on the ground points in respect of those produced by errors on the central strip. Furthermore, higher input errors produce higher corrections on the ground. In particular, the tie point coordinate most affected is predictably the Z coordinate.

For a better understanding of the specific effect of each shift error component, additional simulations were run introducing only a shift error in each coordinate (see Table 4.7.5). As before, error of different size (2 σ, 3 σ, 4 σ) where applied in cases 21 to 29.

Table 4.7.5 – List of Shift errors imposed on the central (left) and on the lateral strip (right) antenna coordinates of the reference block.

	Central strip			**Lateral strip**		
	DX (m)	**DY (m)**	**DZ (m)**	**DX (m)**	**DY (m)**	**DZ (m)**
21	0.06	0	0	0.06	0	0
22	0	0.06	0	0	0.06	0
23	0	0	0.10	0	0	0.10
24	0.09	0	0	0.09	0	0
25	0	0.09	0	0	0.09	0
26	0	0	0.15	0	0	0.15
27	0.12	0	0	0.12	0	0
28	0	0.12	0	0	0.12	0
29	0	0	0.20	0	0	0.20
30	0.20	0	0	0.20	0	0
31	0	0.20	0	0	0.20	0

As in previous cases, the errors imposed on the lateral strip produce larger deviations on the ground point coordinates with respect to those produced by errors on the central strip, see Table 4.7.6 and Table 4.7.7.

Table 4.7.6 – Statistics of Ground coordinates corrections for the simulation cases 21-29 of shift error on the Central strip of the block.

Error value	2 σ		3 σ		4 σ	
Case	**21**		**24**		**27**	
	Mean (m)	**σ** (m)	**Mean** (m)	**σ** (m)	**Mean** (m)	**σ** (m)
DX	0.019	0.021	0.029	0.021	0.039	0.021
DY	-0.033	0.024	-0.033	0.024	-0.033	0.024
DZ	-0.001	0.056	-0.001	0.056	-0.001	0.056
Case	**22**		**25**		**28**	
	Mean (m)	**σ** (m)	**Mean** (m)	**σ** (m)	**Mean** (m)	**σ** (m)
DX	-0.001	0.021	-0.001	0.021	-0.001	0.021
DY	-0.013	0.023	-0.003	0.023	0.008	0.023
DZ	-0.001	0.056	-0.001	0.056	-0.001	0.056
Case	**23**		**26**		**29**	
	Mean (m)	**σ** (m)	**Mean** (m)	**σ** (m)	**Mean** (m)	**σ** (m)
DX	-0.001	0.021	-0.001	0.021	-0.001	0.021
DY	-0.033	0.024	-0.033	0.024	-0.033	0.024
DZ	0.032	0.056	0.049	0.056	0.066	0.056

Table 4.7.7 – Statistics of Ground coordinates corrections for the simulation cases 21-29 of shift error on the Lateral strip of the block.

Error value	2 σ		3 σ		4 σ	
Case	**21**		**24**		**27**	
	Mean (m)	**σ** (m)	**Mean** (m)	**σ** (m)	**Mean** (m)	**σ** (m)
DX	0.019	0.021	0.029	0.021	0.039	0.021
DY	-0.033	0.027	-0.033	0.029	-0.033	0.032
DZ	-0.001	0.056	-0.001	0.057	-0.001	0.057
Case	**22**		**25**		**28**	
	Mean (m)	**σ** (m)	**Mean** (m)	**σ** (m)	**Mean** (m)	**σ** (m)
DX	-0.001	0.020	-0.001	0.020	-0.001	0.020
DY	-0.013	0.024	-0.004	0.024	0.006	0.024
DZ	-0.003	0.056	-0.004	0.056	-0.004	0.056
Case	**23**		**26**		**29**	
	Mean (m)	**σ** (m)	**Mean** (m)	**σ** (m)	**Mean** (m)	**σ** (m)
DX	-0.001	0.021	-0.001	0.021	-0.001	0.021
DY	0.093	0.024	0.156	0.026	0.219	0.029
DZ	0.031	0.084	0.047	0.109	0.063	0.137

As evident in the statistics reported in the above tables, the adjusted block seems to be in most cases just shifted: indeed, the standard deviations of the corrections are the same in both cases. The only exception found is when the shift error is imposed to the Z coordinate of the Lateral strip. In fact, focusing on the 23, 26 and 29 cases of the lateral strip, we see larger dispersion of the errors, particularly in Z (up to 13.7 cm) and larger values of mean error, particularly in Y coordinates. This behaviour is likely due to the ill-geometry of the block.

A final set of simulations were run with 20 cm shift errors imposed on one coordinate at once on the Lateral strip. The results of the adjustments are shown in Table 4.7.8.

Table 4.7.8 – Statistics of Ground coordinates corrections for the simulation cases with 20 cm shift error on the Lateral strip of the block.

Error value	Shift DX 20 cm		Shift DY 20 cm		Shift DZ 20 cm	
Case	30		31		29	
	Mean (m)	σ (m)	Mean (m)	σ (m)	Mean (m)	σ (m)
DX	0.063	0.021	-0.003	0.022	-0.001	0.021
DY	-0.033	0.043	0.033	0.024	0.219	0.029
DZ	0.001	0.058	-0.004	0.056	0.063	0.137

Large shift errors of 20 cm on coordinates of lateral strip do not seem catastrophic in cases 30 and 31 on X and Y coordinates; even in the Z case, the X coordinate seem unaffected. To highlight the net error effect of GPS shift errors more clearly, differences between the adjusted ground coordinates with 20 cm shift errors in one coordinate at once with the reference block affected by random error only were computed. This is equivalent to run a simulation with image and GPS measurement without random errors and with gross errors only. The results are shown in Table 4.7.9 respectively with yellow, green and blue. This comparison with the reference block allows to quantify the only shift errors component because the random error component is removed.

Table 4.7.9 – Effect of shift error only on tie point coordinates.

Error value	Shift DX 20 cm		Shift DY 20 cm		Shift DZ 20 cm	
	Mean (m)	σ (m)	Mean (m)	σ (m)	Mean (m)	σ (m)
DX	-0.064	0.007	0.003	0.016	0.001	0.021
DY	0.000	0.033	-0.066	0.004	-0.253	0.024
DZ	-0.003	0.014	0.003	0.012	-0.064	0.124

For the X and Y coordinates, the 20 cm error in the GPS data is reflected in a translational motion of the block by about 1/3 of the error (6.6 cm) in the direction of the coordinate affected, with almost no other effects of deformation of the block (as can be seen from the fact that the standard deviation of the corrections is negligible and unchanged). This does not apply to the error in Z, where, in addition to the 1/3 shift along Z, also the Y coordinate is affected significantly (more than 25 cm). Moreover, also the standard deviation of the correction in Z increases to 12 cm, i.e. a deformation occurs.

4.7.2.2. Drift errors

As far as the simulation of drift errors is concerned, on the basis of the previous results, just an incremental error from 0.09 to 0.30 m on one coordinate at a time were considered for the lateral strip only. The results show the same behaviour of the previous shift error simulations: errors in GPS Z coordinate result in large errors in Z and Y on the ground as visible comparing Table 4.7.8 and Table 4.7.10.

Table 4.7.10 – Statistics of ground coordinates corrections for the simulation cases with 20 cm drift error on the Lateral strip of the block.

Error value	Drift DX 20 cm		Drift DY 20 cm		Drift DZ 20 cm	
	Mean (m)	**σ** (m)	**Mean** (m)	**σ** (m)	**Mean** (m)	**σ** (m)
DX	0.064	0.025	0.000	0.021	0.005	0.021
DY	-0.034	0.043	0.032	0.030	0.214	0.029
DZ	-0.007	0.058	-0.006	0.056	0.062	0.136

As previously, to highlight the effect of the drift errors only, differences on ground coordinates were referred to the block with random errors only (see Table 4.7.11).

Table 4.7.11 – Effect of drift error only on tie point coordinates.

Error value	Drift DX 20 cm		Drift DY 20 cm		Drift DZ 20 cm	
	Mean (m)	**σ** (m)	**Mean** (m)	**σ** (m)	**Mean** (m)	**σ** (m)
DX	-0.065	0.022	-0.001	0.013	-0.006	0.001
DY	0.000	0.033	-0.065	0.021	-0.247	0.024
DZ	0.006	0.012	0.005	0.007	-0.063	0.124

The error in the GPS data is reflected in a translational motion of the block in the direction of the coordinate concerned for about 1/3 of the average drift error (6.6 cm) with no other effects of deformation of the block (as can be seen from the fact that the standard deviation of the corrections is negligible and unchanged).

This does not apply to the error in Z, where, in addition to the 1/3 shift along Z, also the Y coordinate is affected significantly (more than 25 cm). Moreover, also the standard deviation of the correction in Z increases to 12 cm, i.e. a deformation occurs.

Chapter 5
Empirical accuracy test of UAV photogrammetric surveys

5.1. Introduction

With the growing use of UAS platform for aerial photogrammetry, it is interesting to figure out the level of accuracy obtainable with UAS-platforms. Specifically, the aim of the work is determinate the accuracy of different georeferencing technique:

i. Using GCP, in order to estimate the influence of different GCP configurations on the accuracy of block orientation;
ii. Using GPS-on board, to assess the performance of RTK GPS acquisition mode.

In this Chapter, two empirical studies on the potentiality of UAS photogrammetry are presented, which have been performed at the Campus of Parma University with the realization of a test-field surveyed by two flights and the experimental flight using a drone RTK-equipped at the rock glacier of Gran Sommetta.

The test area, the acquisition of ground data used as control and checkpoints and the execution of two flights will be described. Then, the georeferencing and its accuracy will be discussed.

5.2. Campus: Motivations and objectives

The growing use of UAS platform for aerial photogrammetry comes with a new family, highly automated, processing software capable to deal with the characteristics of these blocks of images. It is of interest to photogrammetrist and professionals, therefore, to find out whether the image orientation algorithms and the DSM generation methods implemented in such software are reliable and the DSMs and orthophotos are accurate. On a more general basis, it is interesting to figure out whether it is still worth applying the standard rules of aerial photogrammetry to the case of drones, achieving the same inner strength and the same accuracies as well. With such goals in mind, a test area has been set up at the University Campus in Parma. A large number of ground points has been measured on natural as well as signalized points, to provide a comprehensive test field, to check the accuracy performance of different UAS systems. In the test area, points both at ground level and features on the buildings roofs were measured, in order to obtain a distributed support also altimetrically. Control points were set on different types of surfaces (buildings, asphalt, target, fields of grass and bumps).

5.2.1. Study area

Few technical prescriptions and operation guidelines for UAS surveys are available. Likewise, few analyses exist on the costs of UAS cartographic surveys based on their extension, in order to find the tipping point from conventional airborne photogrammetry and UAS photogrammetry. As the area of interest increases in size so does the time necessary to complete the survey, due to the short operating time range of the majority of these devices (except, perhaps, the fuel-powered ones that are however less and less used in these applications) and to the low flying speed achievable by rotor based ones; more spare batteries and on-site recharging become necessary; this makes the ground operations more and more expensive. At the same time, in many countries, national UAS flight regulations limit the area that can be covered with a single operation: for example, in Italy, ENAC[5] imposes that the pilot maintains a strictly visual line of sight of the UAS flight, and the flying area is smaller than 500×500 m^2. Moreover, with large blocks, considering that currently the navigation solution of most commercial UAS is not enough accurate to provide direct orientation, a ground survey should provide an appropriate number of GCPs to ensure block control.

Figure 5.2.1 – The area used for the case studies. In light yellow the 140 m high flight zone, in blue the 70 m flight zone. Yellow, blue and red dots show the GCPs used respectively for both case studies, only for the 140 m flight and only for the 70 m flight.

[5] The reference is to the first ENAC Regulation of 17 December 2013 since the work was realized in winter 2013.

For these reasons, the survey was restricted to an area of about 500 × 500 m^2; this size might well represent a case where a cartographic update procedure performed with the use of UAS systems can efficiently substitute for a traditional photogrammetric flight or a ground survey. The area covers part of the Campus of Parma University, for a total of about 23000 m^2 and consists of parking lots, green areas, sporting facilities as well as buildings of various heights (from 6 to 35 m).

The area shows both an urban and/or a countryside or suburbs scenario.

Two different case studies are presented: the first, implementing a 140 m height flight (Italian regulations limit to 150 m the maximum flight altitude for UAS commercial systems) with a GSD of 4 cm, spanning the whole area; the second, with a 70 m altitude (2 cm GSD), limited to a 5000 m^2 region where most buildings are located (see Figure 5.2.1).

5.2.2. UAS survey

The employed drone is a Falcon 8 optacopter, produced by the German company AscTec (see 2.6.3 for specifications). The drone has a fairly good flying autonomy being able, with common payload, to fly up to 20 minutes in automatic way. Nonetheless, for the larger of the two areas, four subsequent flights were required while the smaller had to be divided in 2 subzones, due to the peculiar execution of the flight plan implemented in the navigation software. Rather than shooting with the platform in motion, the navigation software of the Falcon drives the UAS to each waypoint, where it hovers while shooting the image.

The Falcon flew with a pre-planned flight whose strips run parallel to the shorter side of the areas. In order to avoid holes and guarantee an overabundant stereoscopic coverage, the longitudinal overlap was fixed to 80% and the side one to 40%. As will be further explained in the next sections, one of the most critical aspect involving this kind of survey is that not always the estimated overlap is observed (even with a carefully designed flight plan), especially in urban environments where abrupt height changes have to be expected. Given the on-board camera characteristics and mounting (see below), the camera station waypoints were planned according to a base length of about 13 m for the 70 m flight and about 25 m for the 140 m flight. A total of 104 images were obtained for the smaller area, divided in 8 strips (4 strips for each subzone), and 128 for the larger area in 16 strips (see Table 5.2.1 and Table 5.2.2).

The camera installed on the UAS is a compact Sony NEX-5 (Sensor APS CMOS Exmor™) with a resolution of 14.2 Mpixel, image frame 21.6 × 14.4 mm, pixel size 4.7 micrometres and a fixed focal length of 16.3 mm. To reduce the payload, the camera is powered by the battery pack of the UAS. This complicated a little the calibration of the optics, since also the image acquisition for the calibration must be performed with the camera connected to the UAS, unless the gimbal stage is dismounted and all electrical connections from the camera are removed. An analytical calibration, estimating the lens distortion and the interior parameters of the camera, using a calibration panel and a bundle adjustment procedure was performed. A self-calibration using the flight image block can be used as well, in particular if cross strips are provided since, with this kind of block geometry, the calibration outcome is usually reliable and accurate. Nonetheless a specific calibration procedure, with proper geometry configuration (convergent images, also rotating the camera around its optical axis [72] can reduce or remove unwanted correlations between interior and exterior parameters.

Table 5.2.1 – UAS flight plan characteristics at 140 m.

Flight at 140 m						
GSD	**Overlap**	**Sidelap**	**Ground overlap**	**Ground sidelap**	**N. strip**	**N. images**
(cm)	(%)	(%)	(m)	(m)	-	-
4.1	80	40	100.5	75.5	4 × 4	128
Image Footprint		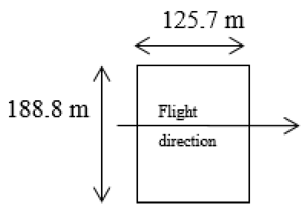			**Image scale** 1:8750	

Table 5.2.2 – UAS flight plan characteristics at 70 m.

Flight at 70 m						
GSD	**Overlap**	**Sidelap**	**Ground overlap**	**Ground Sidelap**	**N. strip**	**N. images**
(cm)	(%)	(%)	(m)	(m)	-	-
2.1	80	40	50.3	37.8	4 × 2	104
Image Footprint		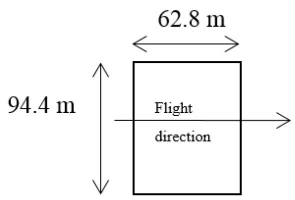			**Image scale** 1:4300	

5.2.3. Ground data acquisition

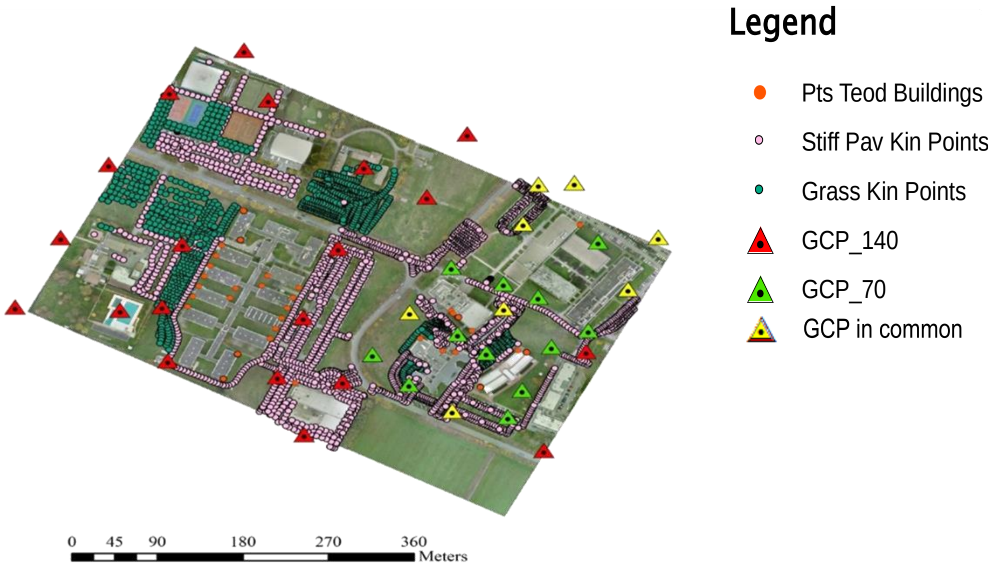

Figure 5.2.2 – GCP and CP distribution and categorization over the area of interest.

Different kinds of ground targets were designed, realized and located with a homogeneous distribution (Figure 5.2.2) all around the study area, to evaluate which one allows the best performance (especially in terms of identification and collimation easiness and accuracy) and to provide Ground Control Points and Check Points:

a) Markers made using A3 or A4 paper sheets glued to black painted cardboards fixed to the ground, on the buildings and on survey points of the topographic network of the campus (Figure 5.2.3);
b) Markers made by metal sheets painted in a black and white checker pattern;
c) Natural/existing features, such as road signs, manholes, edges of buildings and tracks in parking or sport facilities.

Figure 5.2.3 – Types of marker for Ground Control and Check Points.

An existing topographic network has been exploited in order to determine new GCPs and CPs.

Points at ground level were surveyed with GPS receivers Leica 1230 and Leica SR500 in static mode, with the rover occupying every point from 8 to 15 minutes with average PDOP values of 2 and maximum of 3. On the other hand, points on rooftop corners or markers on building roofs were surveyed with a Topcon IS203 total station, the former using the reflector-less rangefinder, the latter with a prism pole centred on the target. Points with markers were stationed at least twice to guarantee that the final dataset was error-gross free. For both the total station and the GPS survey, repeated measurements shows that an accuracy of 1÷2 cm can be expected.

To check the DSM accuracy, points were measured on terrain break lines and on parking lots, pavements and fields, roughly on a grid with a spacing of 4-5 m. Overall 3585 points distributed all over the Campus study area (1340 in the area covered by the 70 m flight) were measured with GPS "stop and go", occupying each point from 2 to 10 seconds.

The GCPs, as traditional photogrammetric survey guidelines prescribe, are located on the border of the area of interest, at least one every three 60% overlap stereo-models (i.e. one GCP every five images). As a result, there were 28 GCPs for the flight at 140 m, and 20 for the flight at 70 m.

5.2.4. Data processing

The photogrammetric survey was realized on the basis of traditional aerial photogrammetry rules in order to check that at least the same level of accuracy can be obtained with UAS-platforms. The reference accuracy in planning the survey was mapping at 1:1000 map scale, where a tolerance (2σ) of 40 cm for horizontal and vertical components is foreseen.

The most important procedure in the photogrammetric pipeline, that can influence critically the final restitution accuracy, is represented by the image block orientation. Using a small frame camera and considering the high number of frames that a common UAS block can have (the usually higher overlap and the small area covered by a single image can produce blocks with several hundred or thousands of images even for small areas), unwanted block deformations might arise. At the same time, a sufficient number of GCP (not to mention CP), cannot always be provided to improve the block rigidity.

The automatic orientation procedure, exploiting the overabundant longitudinal and side overlap, should limit or remove such potential weakness by increasing the number and quality of the tie points. AgiSoft PhotoScan, a widely diffused software package was used. The software has a very simple and straightforward workflow that makes it ideal for non-specialist users. Though it provides very limited reports on block quality, state of the art results are delivered at a very affordable price. Due to commercial reasons very few information about the used algorithms are available: some details can be recovered from the PhotoScan User forum [4] where Agisoft states that the software uses a SIFT-like algorithm for point extraction and matching and solves for interior and exterior orientation parameters using a greedy algorithm followed by a more traditional bundle adjustment refinement. The PhotoScan package, as a matter of fact, shows very limited information, and the quality analysis had to be performed in another software environment.

In virtually every program of SfM, the block orientation is complemented by a self-calibrating bundle adjustment in a projective or metric frame. In PhotoScan the user can insert his own calibration parameters and keep them fixed in the bundle adjustment or let PhotoScan to self-calibrate. In the orientation procedure this second possibility has been exploited, providing as initial values those obtained by the analytical calibration of the camera, executed just after the flight, using PhotoModeler.

Table 5.2.3 – Inner orientation parameters of the self and analytical calibration.

Inner orientation parameters	**PhotoScan – Self Calibration**			**Photomodeler**
	140 m flight 28 GCP	**140 m flight 9 GCP**	**70 m flight 9 GCP**	**Analytical Calibration**
Focal lens (mm)	16.286	16.283	16.386	16.341
PPx (mm)	11.955	11.952	11.961	12.015
PPy (mm)	8.043	8.047	8.057	7.973
K1 (mm^{-2})	2.54E-04	2.55E-04	2.56E-04	2.94E-04
K2 (mm^{-4})	-1.41E-06	-1.42E-06	-1.44E-06	-1.57E-06
K3 (mm^{-6})	-2.13E-11	-5.52E-12	1.11E-10	0.00E+00

As will be shown in the next sections, the two blocks have been oriented with more than a GCP configuration. Table 5.2.3 lists the values of the inner orientation parameters of the analytical calibration and the self-calibrated values: the two procedures produce very similar parameters; due to the lack of cross strips in the block, however, some residual correlation effects led probably to the small discrepancy in the PPx and PPy values in the two solutions.

Before the automatic orientation procedure starts, it is usually convenient to insert and collimate on the images all the GCPs.

5.2.4.1. Flight at 140 m

The flight at 140 m was planned using the normal case of stereo-photogrammetry: given the characteristics of the camera and the image scale the expected accuracy was 11.5 cm for σ_z calculated for a 60% overlap. As already said, the flight was realized with 80% forward overlap, 40% sidelap and arrangement of the GCPs one every three 60% models.

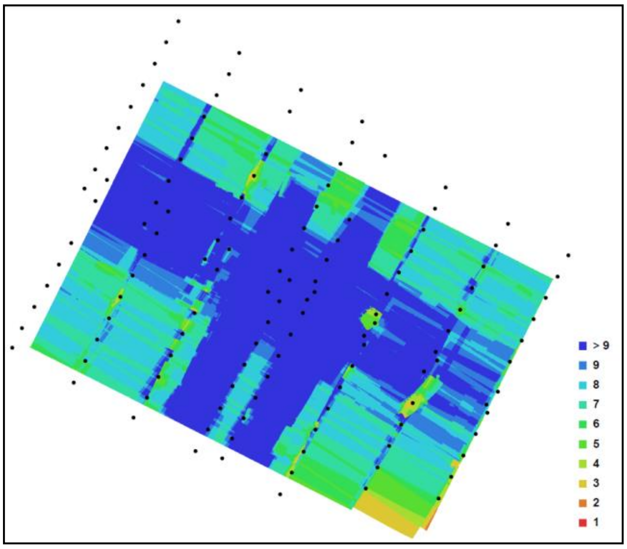

Figure 5.2.4 – Image overlap and camera locations of 140 m flight.

Figure 5.2.4 shows the overlap between the frames and the camera locations as well.

Some difficulties were found as a consequence of the presence of high buildings (up to 35 m) and the consequent variation of image scale produced sudden, localized, variation of the actual overlap. Even if an 80% overlap was enforced, some areas of the building top were hardly visible in at least two images or occluded.

The analysis for the flight 140 was performed considering different bundle block configurations:

a) Using only 9 GCPs distributed on the ground along the border and one in the centre of the area (Figure 5.2.5).
b) Using all 28 GCPs distributed on the ground.
c) Using all 28 GCPs distributed on the ground and 7 GCPs on the buildings from 25 to 32 meters high.

The goal is to study the restitution accuracy according to the distribution and number of GCPs in the BBA, to find out whether less GCPs might be used, reducing overall surveying costs and get a confirmation of the simulations results of Chapter 4.

The accuracy for each configuration was evaluated comparing the coordinates of CPs that have been estimated in the photogrammetric bundle adjustments with those measured with total station and GPS. The RMSE (Root Mean Square Error) of the differences was calculated for each GCP configuration, considering the whole CP dataset or collecting separated statistics of those on buildings and on the ground. The statistics are summarized in Table 5.2.4 with the number of CPs used.

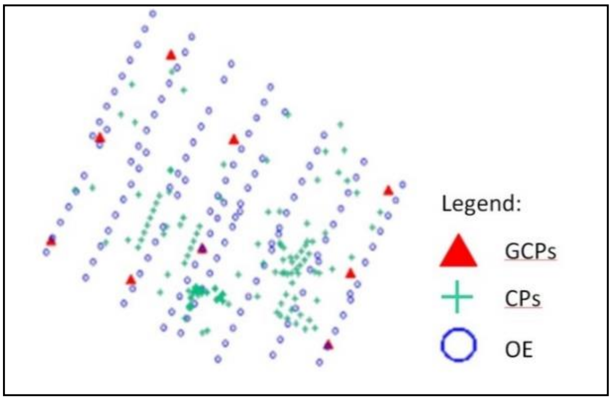

Figure 5.2.5 – Distribution of 9 GCPs for the block orientation in the a) version.

The a) configuration shows the highest RMSE for Z coordinates both of CPs on buildings as well as those on the ground.

In case b) the inclusion of more GCPs improves of ca. 4 cm the accuracy of Z coordinates.

The c) is the most complete scenario, including all GCPs on the ground and also 7 on the highest buildings (ca. 30 meters). There is a further increase of Z accuracy; it is worth noting that the improvement is mainly related to CPs on buildings, while the accuracy of CPs on the ground remains basically the same of case b). This suggests that constraining GCPs on buildings improves the solution, obtaining height accuracy values of the same order regardless of the point height. Anyway, the small GSD and, likely, the image quality not so clearly inferior to professional-grade cameras, allow to achieve better than expected accuracies even in case a). It should be mentioned, however, that CP were collimated in more than two images, so an accuracy better than the normal case is foreseen.

Therefore, on the basis of discrepancies at CP, the solution using only 9 well distributed GCP is still adequate for cartographic update purposes at this scale.

Table 5.2.4 – Flight 140: coordinates difference value in the three configuration of UAS block on all CPs, on buildings and on the ground.

Flight 140 - RMSE on the CPs												
	All CPs				CPs on buildings				CPs on the ground			
Block version	**N. CP**	**DX**	**DY**	**DZ**	**N. CP**	**DX**	**DY**	**DZ**	**N. CP**	**DX**	**DY**	**DZ**
		(cm)	**(cm)**	**(cm)**		**(cm)**	**(cm)**	**(cm)**		**(cm)**	**(cm)**	**(cm)**
a) 9 GCP	127	5.6	4.6	9.2	34	7.4	4.6	9.4	93	5.1	4.7	9.1
b) 28 GCP	108	4.8	4.8	5.2	34	5.5	4.3	6.4	74	4.5	4.9	4.5
c) 28+ 7GCP	101	4.6	4.7	4.5	27	5.1	4.1	5.3	74	4.4	4.9	4.3

5.2.4.2. Flight at 70 m

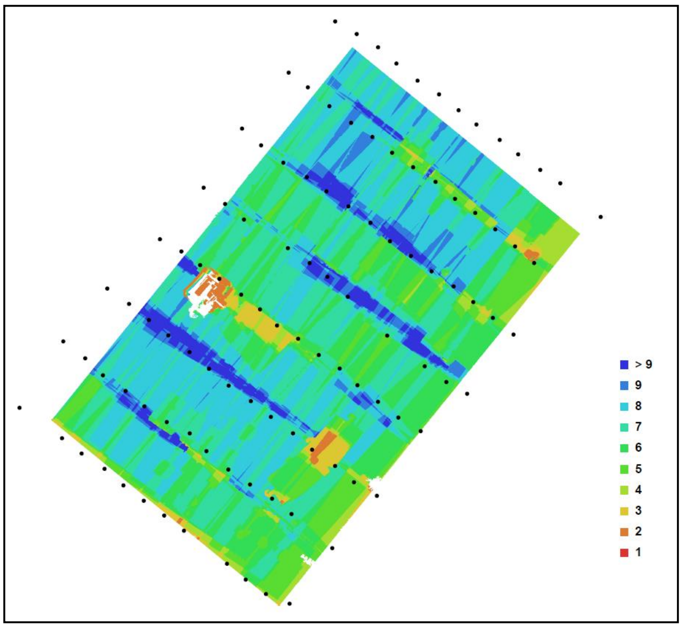

Figure 5.2.6 – Image overlap and camera locations of 70 m flight

The flight at 70 m was planned according to the same criteria as the previous flight. Given the characteristics of the camera and image scale (Table 5.2.2), the expected accuracy was fixed at 5.7 cm for σ_z. Figure 5.2.6 shows the overlap between the frames and the camera locations as well. The block was oriented using 20 GCP.

The statistics of RMSE of differences are shown in Table 5.2.5. The RMSE of differences shows values in X and Y comparable to the GSD and twice the GSD for the Z coordinates. The errors of CPs on building are larger than the ground level ones (especially the coordinates Y and Z are affected) as expected since in this case higher level GCP are missing. Finally, the RMSE residual on all CPs is always smaller than the expected accuracy (Table 5.2.5).

Table 5.2.5 – Flight 70: RMSE of total CPs, of CPs on buildings and on the grounds.

Flight 70: RMSE on the CPs									
Block version	**All CPs: 39**			**CPs on buildings (10)**			**CPs on the ground (29)**		
	DX (cm)	**DY (cm)**	**DZ (cm)**	**DX (cm)**	**DY (cm)**	**DZ (cm)**	**DX (cm)**	**DY (cm)**	**DZ (cm)**
20 GCP	2.1	4.7	5.6	2.2	11.1	8.6	2.0	2.1	4.9

5.2.5. Digital Surface Model production

The DSMs of both areas were created using PhotoScan as well. With a grid step of 8 cm. At this stage the level of automation of the software is quite impressive (though, for very large blocks, a huge amount of memory and processing power is required): regardless of the number of images, their spatial distribution and the shape of the object, the software executes in a fully automatic way the 3D reconstruction. If the scene depicted is 2.5D, an ad- hoc algorithm (called Height-field) grants better results with (usually) less outliers, higher processing speed and lower memory requirements. Also in this case, though, the user-manual, the scientific literature and the topics discussed in the user forum lack real information on the algorithms and techniques implemented in this stage by the software. Apparently (see for instance [4]) except for a “Fast” reconstruction method selectable by the user before the image matching process starts, that uses a multi-view approach, the depth map calculation is performed pair-wise (probably using all possible overlapping image pairs) and merging the results in a single 3D model.

5.2.5.1. Products and Results

Three 3D models have been produced; the first two from the 140 m flight oriented first with 28 GCP and then with 9 GCP only; the third from the 70 m flight oriented with 20 GCP. Some problems, partly related to the sudden change in image scale and partly to the quite complex roof structure, showed up on high-rise buildings roofs.

The validation was performed comparing the models with the GPS (on fields and paved surfaces) and total station (on buildings) survey data.

The models were imported in ArcGis as raster, setting an interpolation resolution of 20 cm, a compromise between maintaining the details obtained with the GSD of UAS survey and the memory size of the model.

The difference between DTM and CPs was calculated using ArcGis "Spatial Analyst Tool" that permits to interpolate the raster at the measured GPS points and extract tables of discrepancies.

For each dataset, the mean and the RMS of differences were calculated. The errors were classified according to the different ground surface:

a) details: i.e. well recognizable points as road signs, manholes and tracks of playing fields (72 GPS points);
b) CPs on the buildings (7 survey points);
c) lawns (1242 GPS points);
d) embankment (61 GPS points);
e) paved roads and parking lots (2056 GPS points).

The results are summarized in Table 5.2.6 for the 140 m flight.

Table 5.2.6 – Differences in elevation between the DSM 140 (version block with 28 GCPs and 9 GCPs) and CPs.

		DSM 140m Flight 28 GCPs		DSM 140m Flight 9 GCPs	
Ground surface classification	**N. CP**	**$Mean_{DZ}$ (m)**	**$RMSE_{DZ}$ (m)**	**$Mean_{DZ}$ (m)**	**$RMSE_{DZ}$ (m)**
Details	72	0.049	0.081	-0.047	0.073
CPs on buildings	7	0.032	0.074	-0.055	0.084
Grass fields	1242	0.073	0.086	0.029	0.079
Embankment	61	0.089	0.147	0.073	0.132
Paved areas	2056	0.019	0.077	-0.057	0.084
Total	3438	0.040	0.081	-0.023	0.056

As a general remark the model accuracy is not much influenced by the surface type, though one would expect the grass to be more difficult than paved surfaces; indeed at the time of the flight (December 2013) the grass cover is not as thick and dense as in springtime. The only noticeable difference is on the embankments where residuals are larger, perhaps due to the smoothing of the 20 cm grid size. Moreover, the mean is positive and larger than in other surfaces for lawns and embankments; a possible explanation if that the tip of the pole rests on the ground surface, while the photogrammetric restitution is somehow intermediate between the ground and the grass top.

Comparing the results of the different block versions, in the configuration with 28 GCPs discrepancies are smaller for CPs on building and paved areas while they get worse in the grassy areas and for points of the class "details". Mean values are always positive values for the DSM oriented with 28 GCPs while with 9 GCPs most are negative. Considering that the differences were always calculated as DSM value minus GPS value, therefore the DSM with 9 GCPs reconstructs an elevation profile lower than those with 28 GCPs, most likely due to a slightly different block orientation form the BBA.

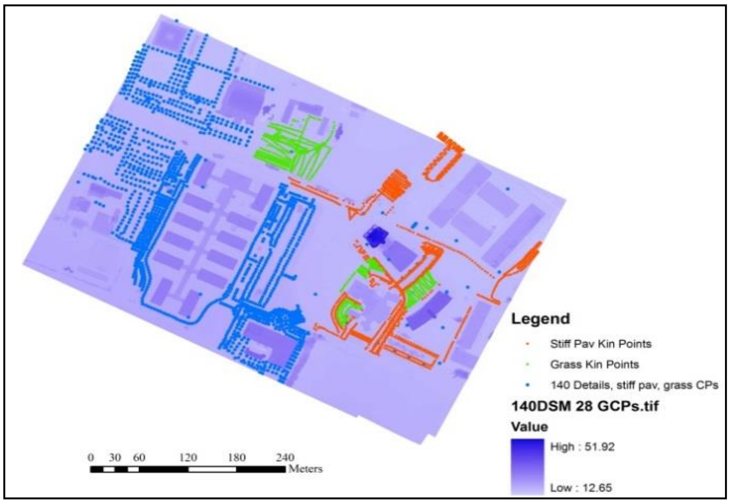

Figure 5.2.7 – DSM of flight at 140 m and GPS survey points location.

Figure 5.2.8 shows the differences between the two DSM of the 140 m flight in the range between 0.2 m and -0.2 m (larger differences occur at building edges and trees, but they are due to the rasterization process).

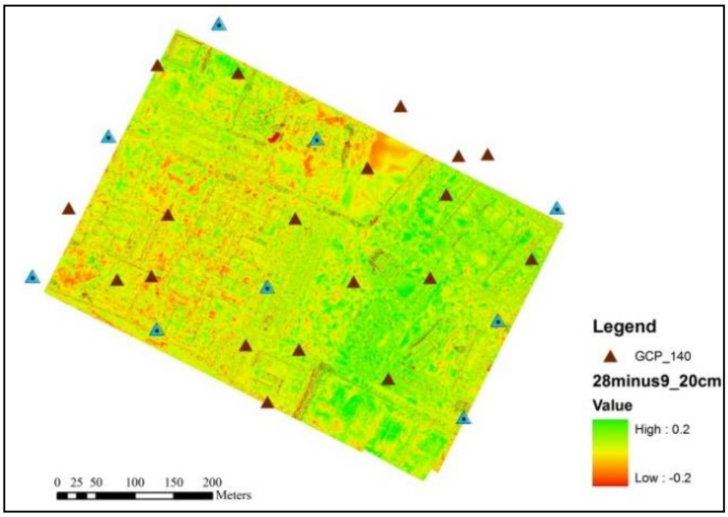

Figure 5.2.8 – Raster at 20 cm resolution of the differences between the 140 m flight DSM with 28 GCPs (brown and light blue triangles) and 9 GCPs (light blue triangles).

A deformation between the two models is clearly visible: on the right side of the area one DSM is lower than the other, while, on the left side the two models are on average in better agreement. This deformation is not related to the kind of terrain nor to its shape: in fact, both sides include grassy fields, paved areas and buildings. Thus, different GCP distribution can introduce block deformation during the bundle adjustment, though this was not noticed from the CPs discrepancy analysis.

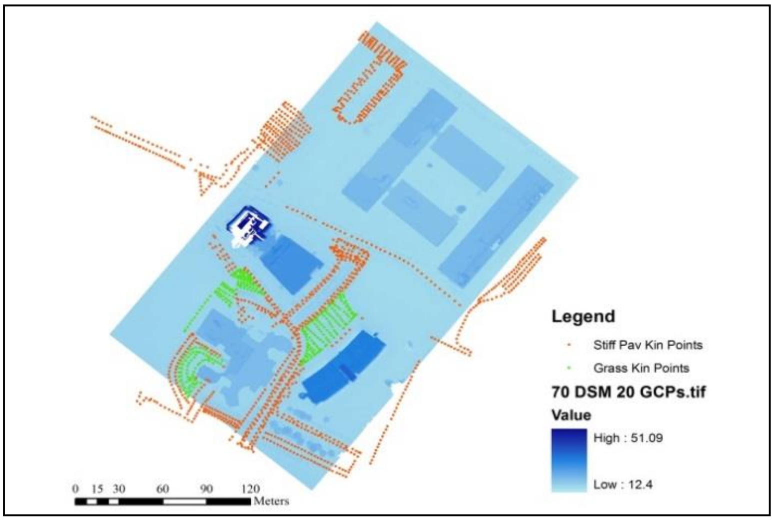

Figure 5.2.9 – DSM of 70 m flight and GPS survey locations.

For the 70 m flight less statistics were collected since the area is smaller and just one GCP configuration was considered. Moreover, due to insufficient overlap (Figure 5.2.6), it was not possible to reconstruct the roof of the higher buildings (Figure 5.2.9). For the same reason no comparisons of CP on building tops were performed. The comparison results for the different types of point is shown in the Table 5.2.7. As for the 140 flight, accuracies are worse in grassy areas.

Table 5.2.7 – Differences between Kinematic GPS and DSM 70 with 20 GCPs.

DSM Flight at 70 m 20 GCPs			
Ground surface classification	**N. CP**	**Mean$_{DZ}$ (m)**	**RMSE$_{DZ}$ (m)**
Grass fields	340	0.087	0.135
Paved areas	873	0.011	0.069
Total	1213	0.032	0.088

5.2.5.2.Differences between 140 m flight and 70 m flight DSM

Since the 140 m flight covers also the area of the 70 m flight, a comparison has been carried out between the two DSM. Since the flights were performed at different times of the day, the difference DSM shows scene changes as well as discrepancies in unchanged areas. Figure 9 shows part of a building and a parking area in the eastern side of the surveyed area: Figure 9a) and 9b) show respectively the 140 m and 70 m DSM; Figure 9c) the difference DSM. Car parked during the 140 m flight but not during the 70 m flight are green coloured. When the same parking lot has been occupied by different car models in the two flights it appears red. An inconsistency between the DSM appears in the reconstruction of the building.

Overall, the differences over the whole area (not shown) are in the order of the elevation accuracy; however, areas with larger discrepancies (up to 20 cm) appear on some of the buildings.

a) Detail of 140 m flight DSM.

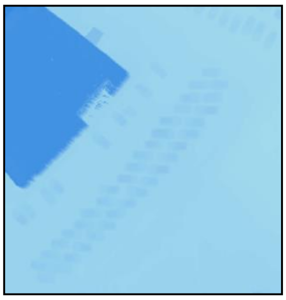

b) Detail of 70 m flight DSM.

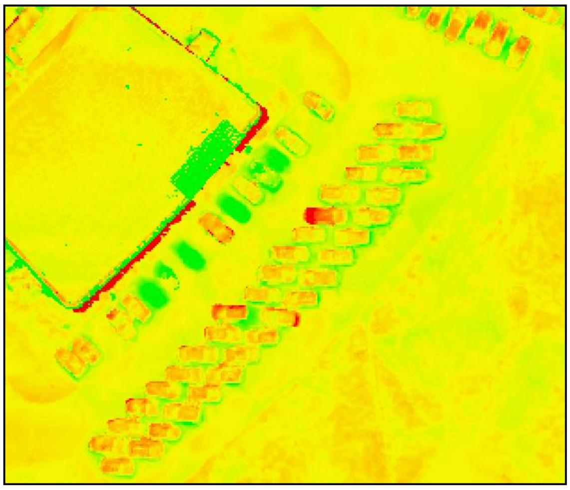

c) Detail of difference DSM.

Figure 5.2.10 – Detail of the difference between the DSMs of the 140 m and 70 m flight (raster at 20 cm resolution).

Two orthophotos (one for the 140 m flight and one for the 70 m) were produced with PhotoScan at 10 cm resolution. They show the problems encountered in the generation of the digital models: in particular for the higher buildings the lack of

3D data due to small overlap required manual operator intervention. These issues are particularly evident in the case of the 70 m flight, where perspective effects and sudden image scale changes are larger than in the other case. To solve or mitigate these problems the 140 m DSM has been used to patch up unreconstructed zones and meshed up with the 70 m DSM. Even if the planned overlap (80%) was bigger than necessary, image scale changes were not managed by feature extraction and restitution failed in those critical areas. On the other hand the manual restitution, which is always possible on condition that stereo coverage is provided, is not supported by appropriate tools in the software.

In the end, as far as urban environment is concerned, the likelihood of occlusions is very high in dense historical centres and increases with low flying heights; sudden and large depth changes occur. Unless the flight altitude limitations imposed by the national regulation are broadened, few solutions can be used:

a) Further increase the forward overlap;
b) Fly additional strips from other directions or increase the sidelap for parallel strips.

This makes obviously the survey more expensive and processing more time consuming.

5.2.6. Conclusions

UAS photogrammetric surveys can supply DSM over sizeable areas within accuracy tolerances of large-scale maps. The RMSE on CP suggests that this should also be the case with vector data plotting. The area range where UAS can be an economically viable solution to map updating or to mapping for specific purposes, however, should be further investigated.

Less GCP density than used in aerial photogrammetry may lead to block deformations, mainly in height. In such cases, cross strips might help and Check Points are needed to verify absence of block deformation; due to the small size of the areas, additional measurements does not substantially increase survey costs.

Increasing the number of GCP from 9 to 28 in the 140 flight improves the accuracy, but only for the altimetric coordinates. Using GCPs also on top of buildings slightly improves the elevation accuracy. In absolute terms, the RMSE on check points is about 5 cm in all coordinates when using dense control. Since UAS surveys have normally a very small GSD and the quality of consumer-grade compact camera has greatly improved in the last few years, even few GCPs (e.g. 9 GCP for a 500×500 m^2 area) are enough for map update.

A DSM was generated for the 70 m flight; for the 140 m, two models (one from a block adjusted with 9 GCP and the other with 28 GCP) were generated. The validation of the 3D models performed with GPS check points showed that for both flights the RMSE is slightly better for points on paved areas with respect to points in grass. However, small discrepancies were found in a relative comparison between the 3D models.

Both models look fairly complete, except for parts of the roof of high rise buildings (one particularly demanding indeed). Flying at low altitude makes it difficult to handle abrupt changes in elevation due to high rise buildings (though an increase in accuracy is apparent on the planimetric coordinates). It is an operative problem that was not expected during the flight planning. Ironically, the image acquisition on predefined waypoints, as in modern aerial photogrammetry with digital flight plan, in this case might have exacerbated the problem. Indeed many UAS still shoot at the maximum frame rate allowed by the camera, providing excess images that should be later discarded or kept in the block, with an increase of the processing time

Thanks to the small GSD, scene changes in elevation can be captured with great detail from DSM difference.

5.3. Accuracy assessment of a block oriented with GPS-assisted AT

A few manufacturers of UAS offer RTK on board. As discussed in Chapter 3, if the accuracy of blocks georeferenced with RTK turns out to be of the same order as those with GCP, UAS photogrammetry would get an even larger push.

Through a collaboration with ARPA Valle d’Aosta, an eBee RTK by SenseFly [38] was used to survey the rock glacier Gran Sommetta (see a detailed description in 6.3). The area is periodically surveyed with UAS photogrammetry since 2012, using signalized GCP measured at each campaign for block adjustment. Independent information is therefore available to check the restitution accuracy of UAS blocks adjusted using GPS on board. In the specific case, since the survey campaigns are executed to control the glacier movements, it is not technically correct to get rid entirely of the GCP. Indeed, as in any monitoring network, stable points should fix the reference system and should be measured at each campaign repetition. Their updated coordinates should be used to compute a Helmert transformation to register every campaign on the first one (or, alternatively, to check whether some point assumed stable has been in fact displaced). In this test case, therefore, the adjusted coordinates of the RTK-oriented block were referred to one of the stable GCP outside the glacier. This is also useful to get rid of possible errors in ambiguity fixing during the flight. While for DSM generation or mapping purposes this would not generally be necessary, it is anyway a best practice. The additional effort required, unless the survey area is far away from the GPS master station (which is normally not the case is flight prescriptions are followed) is minimal: just fly over the GPS master station and put a clearly visible target on ground.

5.3.1.Study area and data acquisition

As mentioned in the results of the GPS–assisted Aerial triangulation simulations, the GPS receiver quality has to be geodetic and the photogrammetric block must have high forward and side overlaps. For all these reasons, the experimental flight was carried by means the eBee RTK (see 2.6.5 for details) an UAS equipped with a double frequency RTK receiver. The images were acquired with forward overlap of 85% and a sidelap of 80% at a relative flying height of 140 m with a GSD of 4 cm. The on board camera is a Sony Cyber-shot DSC-WX220 of 18 MPixel of resolution, focal length of 4.45 mm, image frame 6 × 5 mm and pixel size of 1.22 micrometres. The number of images acquired and used in the bundle block adjustment is 280. The flight parameters are summarised in Table 5.3.1.

Table 5.3.1 – Summary of the eBee RTK flight parameters.

Date	September 2015
N° images used	280
Side overlap	80%
Forward overlap	85%
GSD	4 cm

The eBee RTK technology is based on the ground control station sending corrections in real time to the on board receiver, in order to correct image geotags in flight. In the Sommetta survey, the ground control station received the corrections from a GPS master station set on a known position near the glacier.

Furthermore, 16 signalized GCPs distributed on the edges of the rock glacier (see Figure 5.3.1) were measured with a GNSS receiver GEOMAX Zenith 20 Series in RTK mode. The expected precisions in XY coordinates are 1-2 cm and 2-3 cm in Z. The location of these points, used in previous monitoring campaign, where planned and optimized for the SwingletCAM platform and flight plan normally used. As the orthoimage of the eBee block (Figure 5.3.1) shows, the new block is larger than the previous ones and covers also a large area north of the glacier. Since the GCP are located in the central and southern part of the block, the analysis will be carried out mainly within the area enclosed by the GCP.

The GCPs and the eBee RTK imagery were acquired at different epochs, on August and on September 2015 respectively. After comparison of the September

GCP coordinates with those in previous campaigns, three of the GCPs were discarded because their positions changed by more than 20 cm. The remaining 13 points were found stable at the cm level and used as check points to verify the restitution accuracy of the RTK-oriented block.

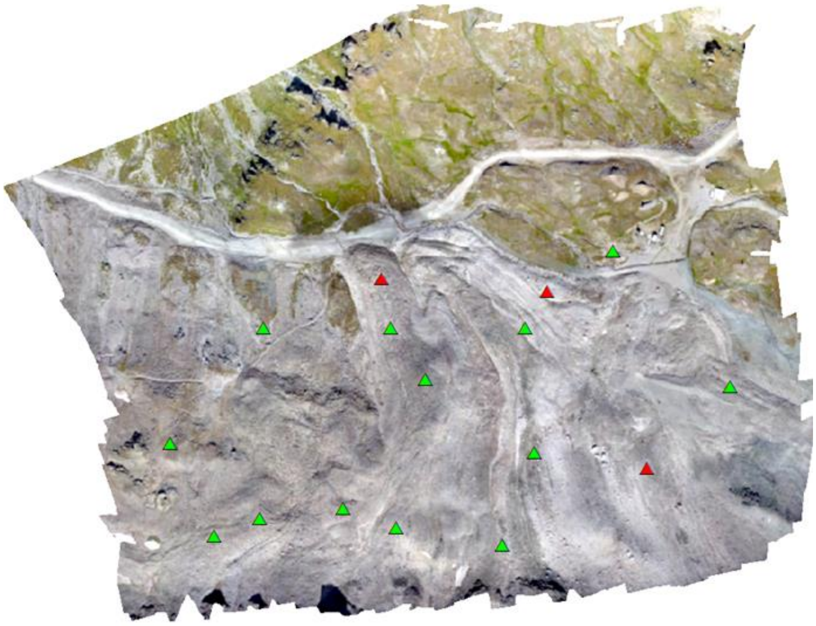

Figure 5.3.1 – Location of 16 Ground Control Points: in green the 13 points used as check points for the RTK- oriented block.

5.3.2. Block orientation

The bundle block adjustment of the UAS survey was performed with the commercial software Agisoft PhotoScan.

Since the images were taken with consumer grade compact cameras, whose optics are usually not very stable, a self-calibration procedure was used in the image orientation process.

Using the same tie points, three different block adjustment were performed:

- with observed camera Projection Centres (PC) from the RTK GPS measurements, using all or just half of the GPS camera stations;
- with all the available GCP.

The automatic tie point extraction processing stage did not perform very homogeneously as can be seen in Figure 5.3.2 and Figure 5.3.3: in the north-western part of the block, even if the image ground coverage is 9, tie points density is considerably lower than elsewhere.

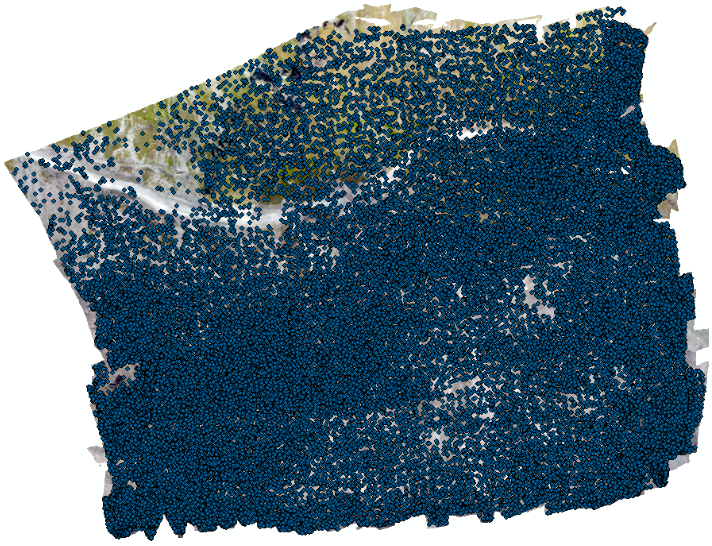

Figure 5.3.2 – Tie points extracted for the GCP and GPS oriented blocks.

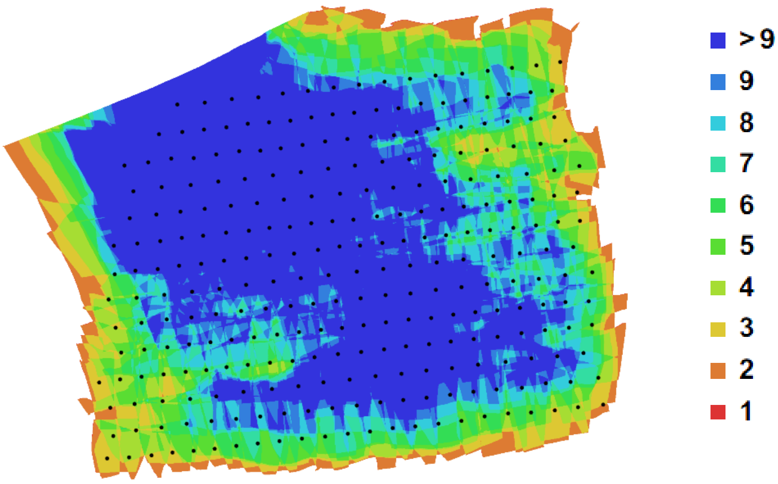

Figure 5.3.3 – Camera location and image ground coverage of the block.

PhotoScan reads the camera locations and orientations throughout the image geotags; each exterior orientation parameter can be assigned an individual weight. The PC precisions were set to 10 cm in all coordinates while the orientation angles from the autopilot were set basically as free unknowns, with a precision of 2°.

Figure 5.3.4 shows graphically the residuals on the PC, i.e. the differences between the adjusted and the measured position of each camera station. Table 5.3.2

reports the statistics of such residuals. Positive values larger than 3 σ are localized in the middle of the southern part of the block; since estimated standard deviations of the residuals σ_v are not provided, it is not possible to test whether they can be classified as gross errors. On the other hand, the standard deviation of the residuals is very close to the measurement precision assigned to the PC coordinates.

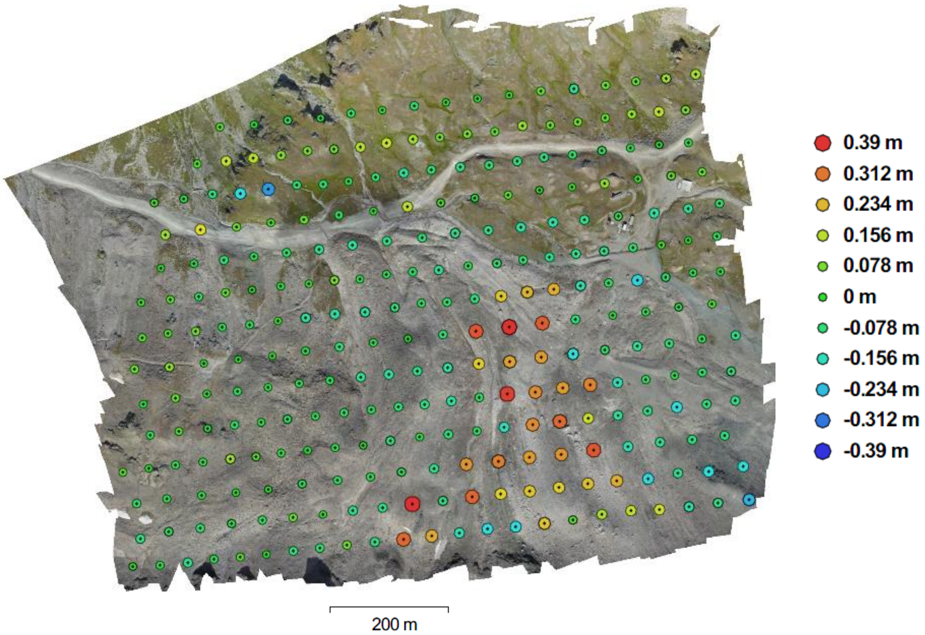

Figure 5.3.4 – Residuals on camera locations (black dots). Z residuals are represented by the ellipse colour. X, Y residuals are represented by the ellipse semi-axes.

Notice that the average of the residual is null in all coordinates: the mean position of the block defined by the RTK measurements is therefore kept unchanged. This suggests that the block might be oriented with a free-net constraint on the PC coordinates (no information is provided in the program manual).

Table 5.3.2 – Statistics of the residuals on the Projection Centres for the block georeferenced with all RTK GPS camera location.

280 PC	vX	vY	vZ
Mean (m)	0.000	0.000	0.000
St. Dev. (m)	0.107	0.109	0.128
Max (m)	0.291	0.371	0.394
Min (m)	-0.399	-0.448	-0.261

After the adjustment, the 13 check points were collimated to determine their coordinates from the RTK block restitution. According to the time-registration procedure of periodic surveys described in Section 5.3, their coordinates (and the whole block) were shifted in order to have zero discrepancy on the selected reference GCP (point number 219).

The accuracy of GPS-assisted triangulation was evaluated comparing the coordinates of CPs estimated in the photogrammetric bundle adjustments with those measured with GPS. The RMSE of the differences is reported in Table 5.3.3.

Table 5.3.3 – Statistics of the errors (discrepancies) at the 12 CP for the block georeferenced with all GPS-determined camera stations.

12 CP	DX (m)	DY (m)	DZ (m)
201	-0.093	0.046	0.008
203	-0.035	0.020	0.076
204	-0.008	-0.003	-0.047
205	-0.019	0.017	-0.006
206	0.008	-0.034	-0.035
207	0.021	-0.048	-0.096
209	-0.005	-0.002	-0.125
210	-0.049	0.026	-0.133
213	0.004	-0.030	0.013
216	0.049	0.000	-0.075
217	0.034	0.044	-0.034
218	0.033	0.033	-0.001
Mean	**-0.005**	**0.006**	**-0.038**
St. Dev.	**0.040**	**0.031**	**0.061**
RMSE	**0.040**	**0.031**	**0.072**

Though the number of CP available is limited (and therefore so is the confidence on the outcome significance), the RMSE obtained is in the order of a few cm, with elevations less accurate than horizontal coordinates. With respect to the simulation results in Chapter 4, the accuracy is perhaps lower, even accounting for the higher relative flight elevation and lower a-priori GPS precision. However, the empirical accuracy is in the order of the GSD, and practically the same as the 140 m test flight on Campus (Table 5.2.4).

As far as the goal of tracking glacier motion is concerned, being the expected displacement well above a decimetre per month in summer time, georeferencing with GPS-on board seems to be a serious alternative to the repeated survey of all GCP at every campaign. Efforts to consolidate the confidence on such results and an analysis of the conditions that guarantees such accuracy should therefore be continued.

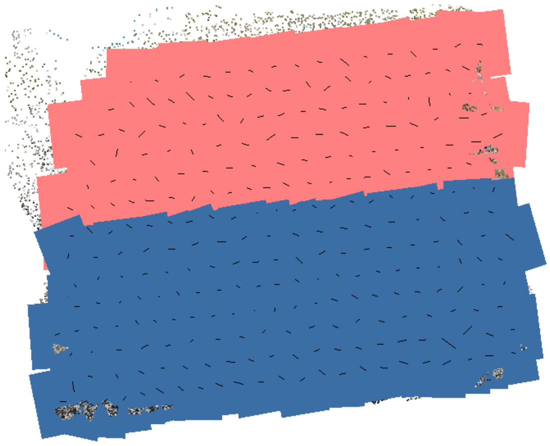

Figure 5.3.5 – The RTK GPS Camera location, in pink the cameras fixed for georeferencing the block.

The block has been also oriented using only half of the RTK GPS camera locations, to find out the accuracy loss due to loss of signal for the RTK correction, disturbances or any other reason that may affect the quality of part of the GPS data. As shown in Figure 5.3.5, only the cameras located in the northern side (pink) were fixed, as before assigning an a-priori 10 cm precision to the coordinates.

Table 5.3.4 – Statistics of the errors (discrepancies) at the 12 CP for the block georeferenced with half GPS-determined camera stations.

12 CP	X	Y	Z
201	0.021	-0.026	-0.017
203	-0.132	-0.013	0.128
204	-0.139	-0.101	0.015
205	-0.102	-0.128	0.078
206	-0.093	-0.084	0.063
207	-0.048	-0.065	-0.059
209	0.058	-0.151	-0.099
210	0.086	-0.164	-0.107
213	0.118	0.123	-0.151
216	0.033	-0.105	-0.014
217	0.029	-0.092	0.119
Mean (m)	**-0.014**	**-0.071**	**0.002**
St. Dev. (m)	**0.087**	**0.077**	**0.092**
RMSE (m)	**0.088**	**0.105**	**0.092**

As can be expected, the statistics are now worse especially for the horizontal coordinates. In particular, there is a noticeable shift of the Y coordinates that are obviously the most affected due to strip geometry. Also the standard deviations (see Table 5.3.4) are larger: about 8 cm in X and Y (twice as before) and 9 cm in Z.

Overall, the accuracy loss of the horizontal coordinates is quite significant in relative terms (100% worse) while elevation is less affected.

Finally, the block has been adjusted also in the traditional way using all the 13 GCPs on the images, in order to allow for the comparison of products of restitution.

5.3.3.Digital Surface Model production

Though the check provided by the comparison of CP coordinates is an indication of the accuracy on ground of blocks oriented with GPS, it is also interesting, for the purpose of terrain displacement analysis, to check the differences between the DSM obtained from the two different block orientations. Three dense point clouds obtained by the three previously oriented blocks were also generated in PhotoScan with a grid step of 16 cm. The produced DSMs regards the whole area framed by UAS imagery; however, the comparison is of particular interest on the rock-glacier body. For the comparison, the original DSMs were interpolated as raster with cell size of 0.5 m over the whole area and over the glacier body.

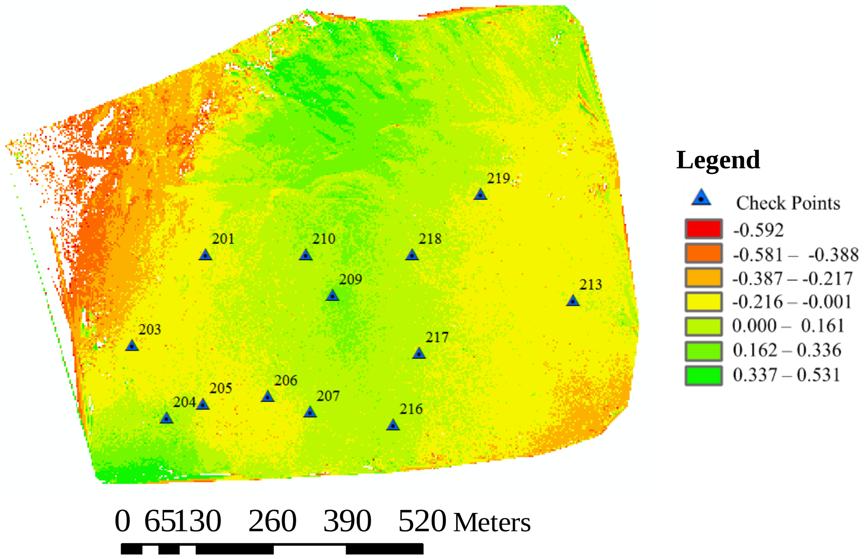

Figure 5.3.6 – Colour map at 0.5 m resolution of the differences (m) between the GCP DSM and the all GPS DSM with location of Check Points (blue triangles).

Figure 5.3.6 shows the raster of Z differences between the GCP DSM and the DSM obtained with all camera positions, with a colour scale with class intervals multiples of the Std. Dev. σ of the differences. The value range is about ± 50 cm, with a standard deviation of 16 cm as reported in Table 5.3.5. The GPS DSM is lower than the GCP DSM in the central part of the area, while it is higher at the West and East sides. The statistics are clearly affected by the large differences in the northern part of the area, where feature extraction works badly and no GCPs are located, see Figure 5.3.1 and Figure 5.3.2.

Table 5.3.5 – Differences between raster DSMs from GCP and GPS on board (all and half camera stations)

	GCP DSM - ALL RTK GPS DSM	**GCP DSM - HALF RTK GPS DSM**
	Mean$_{DZ}$	**Mean$_{DZ}$**
St. Dev. (m)	0.159	0.159

Furthermore, the good accordance is supported by the accuracy evaluation of raster differences on Check points; as reported in Table 5.3.6, the mean value of Z differences is 10.5 cm, a value similar to those calculated for the BBA. It is slightly larger, likely due to the discretization of the raster cell size of 0.5 m.

Table 5.3.6 – Differences between the DSM raster differences at 0.5 m resolution and the error on the 12 Check Points (all and half camera stations).

	ALL RTK GPS DSM – 12 CP	**HALF RTK GPS DSM – 12 CP**
	Mean$_{DZ}$	**Mean$_{DZ}$**
Mean (m)	0.029	-0.009
St. Dev. (m)	0.105	0.115

On the contrary, the central part of the area (Figure 5.3.7), thanks to a higher number of tie points, shows a better agreement, with Z differences in the range between -20 and + 26 cm and a standard deviation of 7 cm, in full agreement with the discrepancies on Check Points.

The GPS DSM is lower than the GCP DSM in the central part of the area, while it is higher at the West and East sides, with a clearly systematic behaviour (the difference surface looks correlated to the terrain topography).

The reason for these systematic differences is not yet clear. In all the three block adjustments, self-calibration has been used. The comparison between the plots of the residual image errors and between the estimated IO and distortion parameters in the PhotoScan adjustment report (Figure 5.3.8) shows that systematic residuals in the order of about half pixel occur in the central part of the image while larger ones occur on the left bottom corner. However, the pattern is pretty much the same in all cases. The IO parameters show only quite small variations (K1 and K2 values being an exception) between the GPS and the GCP adjustments.

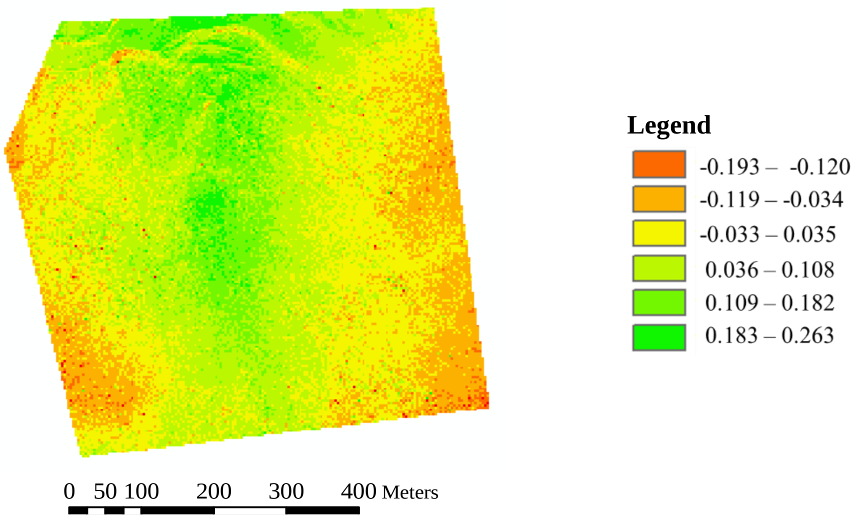

Figure 5.3.7 – Raster at 0.5 m resolution of the differences (m) between the GCP and all GPS DSMs DSMs in the active glacier area.

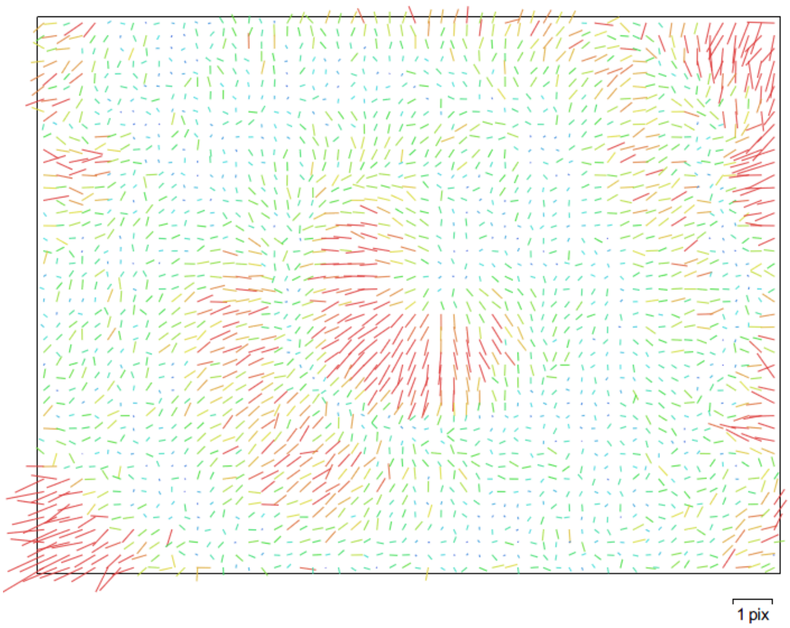

Figure 5.3.8 – Image residuals from the self-calibrating BBA.

The half GPS DSM has been compared with the GCP DSM (see Figure 5.3.9). The standard deviation of the mean Z differences is 16 cm as reported in Table 5.3.5. Instead, the Z differences with respect to the check points, reported in Table 5.3.6, is 11.2 cm.

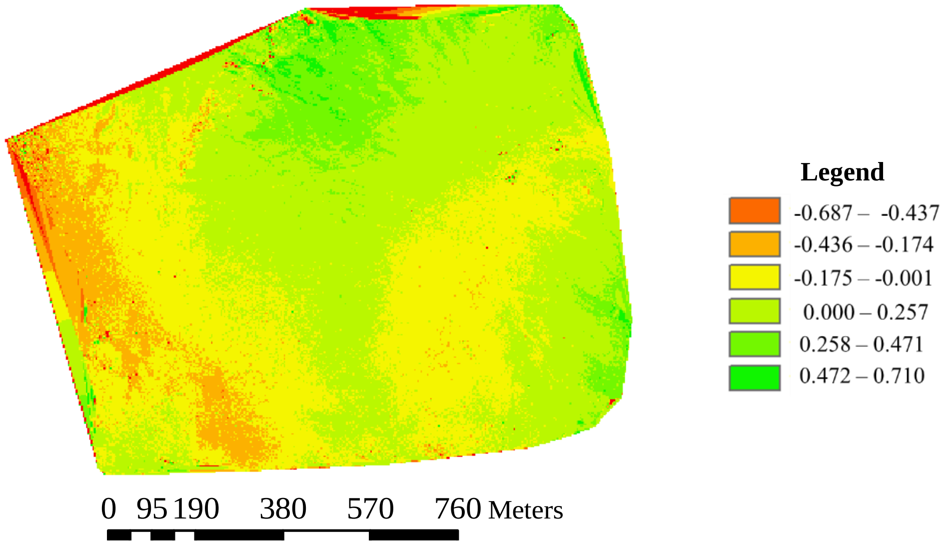

Figure 5.3.9 – Raster at 0.5 m resolution of the differences (m) between the GCP and half GPS DSMs.

The direct comparison between the full dense point clouds of GCP DSM and of the DSM with all GPS camera stations has been obtained by minimizing the distance with respect to all the coordinates (see Table 5.3.7). Notice that two point clouds are aligned in the minimization, therefore the mean is practically zero and the standard deviation is lower than that of the raster differences.

Table 5.3.7 – Differences between GCP and GPS on board point clouds.

	GCP-RTK coordinates
Mean (m)	-0.004
St. Dev. (m)	0.136
RMSE (m)	0.136

Figure 5.3.10 shows an enlargement of the colour map differences on the glacier body area.

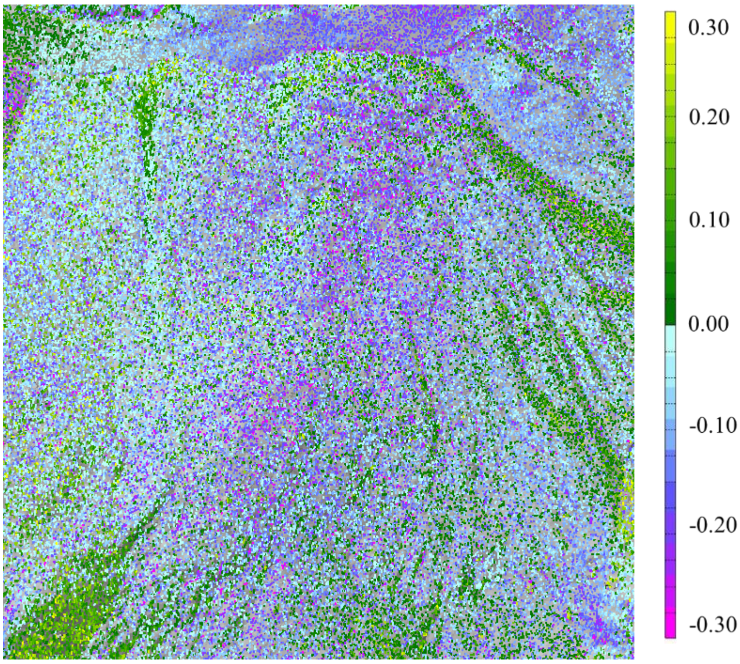

Figure 5.3.10 – Differences between point clouds oriented with GCP (reference data) and GPS on-board on the active glacier area.

5.3.4. Conclusions

The empirical accuracy test on GPS-assisted orientation of the block shows a good agreement between the block oriented with GCPs and that with all GPS RTK camera locations. In fact, the RMSE on CP are in order of the GSD for XY coordinates and 1.5 times larger for the Z coordinate.

These promising results are partially confirmed when the digital surface models of the blocks are compared. Indeed the agreement is full in the central area, just where the glacier movement occur and the tie point density is very high (see Figure 5.3.2) though a systematic trend is evident in the plots of the differences.

On the other hand, as already remarked above, the GCP block accuracy on the northern part is obviously worse than in the central and southern part, due to lack of GCP and (on the West side) of too few tie points. Therefore, in such area, the GCP DSM cannot be taken as reference.

Chapter 6
Application of UAS photogrammetry

6.1. Introduction

This Chapter gathers three case studies representative of UAS photogrammetry applications: two surveys for civil and environmental monitoring for volume and displacement measurement and one survey of a cultural heritage and archaeological site.

The first UAS survey regards the assessment of the volume of a gravel deposit by using different software packages; the second survey focuses on evaluation of Gran Sommetta rock glacier displacements due to climate change effects by periodic UAS survey campaigns.

Lastly, the cultural heritage application focused on the 3D reconstruction of the archaeological roman site of Veleia Romana using integrated techniques of survey.

From here on, the experimental investigations are identified with the name of the site.

6.2. Gossolengo

The use of UAS volume estimation in quarry monitoring is growing since it allows almost completely automatic periodic inspections of the volumes of materials (gravel, sand, etc.) extracted to be carried out. UAVs turn out to be a helpful instrument for identifying both quarries opened without permission as well as the extractions of quantities of materials larger than allowed. In this context, recent studies have been carried out using fixed–wing [126] and rotary-wing aircraft [53].

In fact, UAV platforms in many cases represent the right compromise between economy, precision requirements and point density for the generation of a digital model of the surface. Furthermore, with their features (non-invasive remote control and aerial prospective) UAV platforms are ideal for the ultimate goal, especially in a quarry, where mining activities is always on, since the survey do not hinder the working progress.

As several software packages are available for processing, it is worth to find out the degree of agreement of volume estimation from UAV imagery. To this aim different photogrammetric (both commercial and in-house) and CV software have been used. The results are discussed in order to identify the most efficient procedures in terms of processing time and achievable accuracies. The influence of different GCP configurations is discussed too. The case study is the result of a collaboration with the DICA of the Polytechnic of Milan.

6.2.1. Study area and data acquisition

The study area is located in Gossolengo, near Piacenza; it is a heap of gravel of rectangular shape, extended for ca. 7000 m^2 and with a height of roughly 8 m (Figure 6.2.1).

In July 2013 the heap has been surveyed with a multi-rotor HexaKopter (see 2.6.1) that flew by following a pre-set flight planning, whilst was remotely piloted by an operator during landing and take-off. The flight trajectory is shown in Figure 6.2.2. The on-board compact camera Nikon J1, with a resolution of 10 Mpixel, image frame 13 × 9 mm, pixel size 3.4 micrometres and a fixed focal length of 10 mm, automatically acquired imagery at a flight height of roughly 30 m, with high values of forward and side overlaps (in the order, more than 80% and 50%). Thus, the block was composed of 101 images in four strips, with GSD equal to 1 cm.

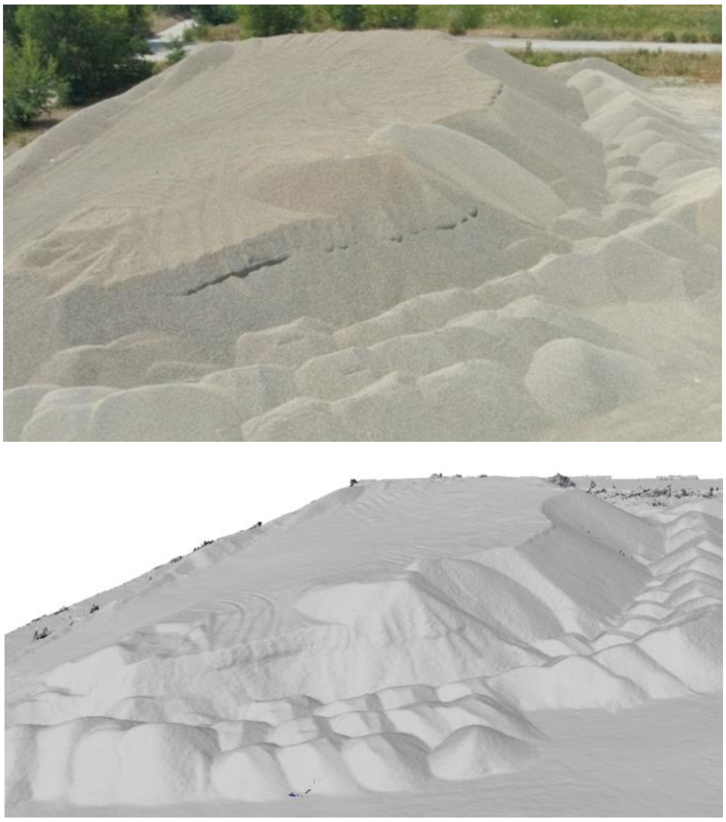

Figure 6.2.1 – Volume estimation of gravel heap: images acquired by HexaKopter in a preliminary phase of flight (upper); 3D model reconstruction of the quarry (lower).

Figure 6.2.2 – Flight lines performed during the survey.

Twenty-one pre-signalised GCPs of two different types were used (Figure 6.2.3):

a) b/w square panels with side of 30 cm and triangular pattern;
b) white square panels with side of 40 cm, black background and marked centre.

Figure 6.2.3 – Types of marker for Ground Control Points.

The GCPs were homogeneously distributed in the area, placing some of them also on the top of the pile; a subset was then used as check points. The coordinates were measured by means of a GNSS receiver Trimble 5700 in NRTK survey (using the ItalPos network), with horizontal and vertical accuracies equal to 2-3 cm and 5 cm, respectively. In this case, the very small GSD implies that photogrammetry's inner precision is better than GCP precision.

This survey method is a compromise between acquisition time of measurements and their accuracies. Thus, it was preferred over others more accurate methods, since it was congruent with the test goals: these were not only the estimation of the materials volume but also the development and test of a workflow suitable for monitoring.

Camera calibration was performed taking images of a b/w planar calibration grid of known geometric properties from different positions and camera orientations and employed to estimate the parameters of a Brown model [22] in PhotoModeler Scanner (see Table 6.2.1; more information in the next subsection).

Table 6.2.1 – Calibration parameters estimated by PhotoModeler Scanner V.7.2012.2.1.

Nikon J1	
Focal length (mm)	10.4706
Principal Point XP (mm)	6.6738
Principal Point YP (mm)	4.5339
Radial distortion k1	$8.45 \cdot 10^{-4}$
Radial distortion k2	$7.82 \cdot 10^{-5}$
Decentring distortion p1	$2.29 \cdot 10^{-6}$
Decentring distortion p2	$3.33 \cdot 10^{-5}$

6.2.2. Block orientation

The acquired images were processed with different categories of software packages:

- commercial photogrammetric software;
- scientific photogrammetric software;
- commercial Computer Vision software.

The first two groups include programs which implement a traditional photogrammetric workflow: camera calibration, GCPs and CPs selection, TPs search (automatic or manual), BBA with or without self-calibration refinement and, lastly, generation of derived products such as DSMs and orthophotos. Exterior orientation parameters and ground point coordinates are usually estimated together with the related accuracies. Some difficulties can arise during the image georeferencing, especially when image positions and attitudes are far from those commonly obtained in aerial photogrammetric surveys. In this regard, PhotoModeler Scanner V.7.2012.2.1 (PM) and the scientific software EyeDEA [107] were used.

Instead, 3D modelling software packages fall within the third group: they carry out the image relative orientation together with the self-calibration, in an arbitrary reference system. The latter is often obtained using a minimum constraint, coming from the approximate orientation provided by the UAS on-board positioning system. Tie points extraction and outliers rejection are completely automated steps. Then, collimation of GCP enables the computation of a Helmert transformation in a specific reference system. However, as discussed in Section 0, digital models of the objects and orthophotos are generated with less control on some steps (e.g. georeferencing) and on the accuracies of the computed parameters. In this software category Agisoft PhotoScan Professional V.0.9.0 was used.

The workflow used in all programs was composed of the same steps: camera calibration, TPs extraction, bundle block adjustment (BBA) and generation of DSMs. However, some little changes were made in accordance to the programs peculiarities, as explained below.

6.2.2.1. Tie points extraction

EyeDEA is a scientific in-house program, developed in our Department, which implements the SURF operator for tie point extraction. Like any other interest operator, SURF can identify a large number of matches, some with erroneous correspondences. For this reason, EyeDEA applies a robust error rejection procedure: the essential matrix E [63] is used to define the constraint between two sets of image coordinates. However, the epipolar constraint is not sufficient to discriminate wrong matches between two points located on the epipolar line. Therefore, EyeDEA implements also the trifocal tensor: the RANSAC paradigm is run after each geometric control to guarantee a higher percentage of inliers. EyeDEA proceeds by successive image triplets: thus, the homologous points are seen, on average, only on three frames.

EyeDEA works on undistorted images: to this purpose, the software "DistRemover" (another Department software development) makes use of the model and parameters estimated by the camera calibration procedure of PhotoModeler, in order to remove deformations from imagery. Since this step is essential in EyeDEA, it was decided to feed the same calibration parameters of Table 6.2.1 to all programs. In addition, a pre-processing to improve contrast was performed prior to the TPs identification, due to the gravel texture. To this end, the adaptive Wallis filter [128], which improves features definition, was applied through the in-house scientific software "WallisFilter". As EyeDEA has been designed for image sequences, it works on triplets of subsequent images, tie points were extracted also along the transverse direction in order to strengthen the connections between strips. 2751 were the homologous points.

PhotoModeler Scanner allows the user to accomplish fully automated projects. It performs feature detection, image matching and orientation in a free-network mode and, in a second phase, the block can be constrained by means of GCPs. A rigorous photogrammetric approach can be used to minimize the block deformation throughout the bundle block adjustment. The PM proper tool (Smart Project) automatically identified 3138 TP.

Agisoft PhotoScan (PS) was used with the PM calibration parameters. Since PS identified a large amount of points, it was decided to decimate them by maintaining the multiplicity as high as possible (664 TP).

In order to compare the three datasets by the same parameters, the EyeDEA and PS homologous points were imported in PhotoModeler.

Table 6.2.2 – Parameters of the three dataset: EyeDEA, PM and PS.

	EyeDEA			PM			PS		
σ_0	1.23			1.19			1.11		
N° images used	101			101			101		
N° Tie Points	2751			3138			664		
	min	**Max**	**media**	**min**	**Max**	**media**	**min**	**Max**	**media**
Tie points for image	19	246	153	22	428	294	6	238	102
N° Rays for point	3	21	6	2	17	3	2	21	15
Intersection Angle	5	72	30	2	60	16	23	73	59

In Table 6.2.2 the number of rays for point is the multiplicity, namely how many times the same point is seen on images. Instead, intersection angle refers to the angle between two rays that intersect the same 3D point. PM has the greatest mean value of extracted TP for image, but the PS dataset reaches the best results regarding the multiplicity and the intersection angle. These are equal to 15 and 59 respectively, which means twice the analogous values of EyeDEA and more than three times the PM ones. This result may be due to the PS search strategy that is done in all the images at the same time. EyeDEA ensures a minimum multiplicity (equal to three) and a discreet intersection angle, as the features research is accomplished on triplet of images. PM achieved the highest number of TPs but on average, with a low multiplicity and a reduced angle.

6.2.2.2. Block orientation

With the aim to check the influence of GCPs number and distribution on BBA outcomes, two different GCP configurations were run in each software package:

1. Using 10 GCPs, on the ground and on the quarry, with 11 CP for check;
2. Using 6 GCPs (all located around the pile) and 15 CP for check.

The second configuration was chosen since it might not be feasible to reach the top of the pile to measure GCP: hence, it is interesting to assess how much a reduced distribution of GCP may affect the volume estimation. Since EyeDEA performs only the tie point extraction, the bundle adjustment was performed in PM.

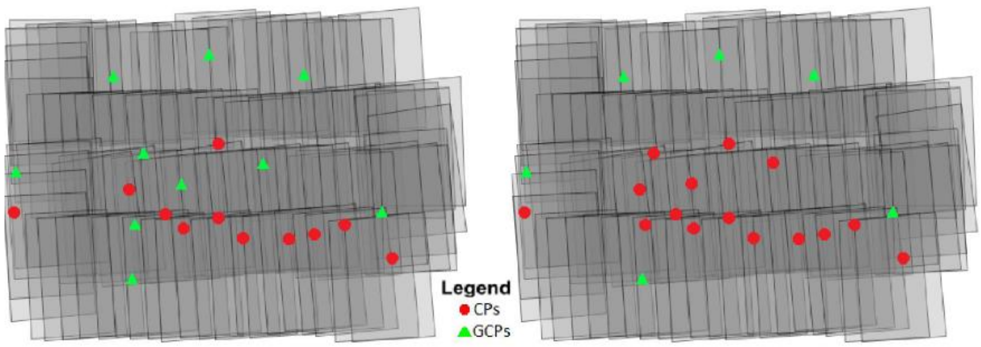

Figure 6.2.4 – The two GCP configuration: on the left 10 GCP and 11 CP, on the right 6 GCP and 15 CP.

Table 6.2.3 shows the RMS of the differences between the TPs ground coordinates estimated by the two BBAs.

Table 6.2.3 – RMS of coordinates differences between the two GCP configurations.

Software	EyeDEA			PM			PS		
	DX (m)	DY (m)	DZ (m)	DX (m)	DY (m)	DZ (m)	DX (m)	DY (m)	DZ (m)
RMS	0.006	0.006	0.024	0.018	0.028	0.036	0.013	0.020	0.033

The horizontal RMSs are of few centimetres for PS and PM and below one centimetre for EyeDEA. Instead, difference in elevation are larger, with the least discrepancies coming from EyeDEA (2.4 cm), whilst the others are between 3 and 4 cm. However, it should be noted that all the values are congruent with the GNSS accuracies of the GCPs coordinates, that is 2-3 cm horizontally and 5 cm vertically.

Table 6.2.4 reports the RMS values of the TPs ground coordinates accuracies, estimated during the BBA with 10 GCPs. Corresponding values of the second configuration are similar, thus not here presented.

Table 6.2.4 – RMS of the standard deviations of the TP coordinates, estimated by the BBA with 10 GCPs.

Software	EyeDEA			PM			PS		
	DX (m)	DY (m)	DZ (m)	DX (m)	DY (m)	DZ (m)	DX (m)	DY (m)	DZ (m)
RMS	0.013	0.021	0.052	0.033	0.021	0.101	0.004	0.004	0.010

Best accuracies of TPs ground coordinates were produced by Agisoft PhotoScan, whose RMSEs are equal to few millimetres horizontally and 1 cm vertically. These interesting results may be connected to the high point's multiplicity (on average 15, see Table 6.2.2). The worst values came from PhotoModeler, especially with respect to the height coordinate.

Furthermore, the CP residuals for both configurations were analysed (Table 6.2.5). Firstly, it can be observed that the values of EyeDEA are consistent with the GNSS accuracies of the GCPs coordinates. This is true also for the PS results, even if they are slightly worse: however, it should be kept in mind the possible operator's error in measuring GCPs and CPs on images, remembering that a mistake of 1 pixel means a residuals variation of 1 cm.

Table 6.2.5 – RMSE on the CPs: BBA with 10 GCP (top); BBA with 6 GCP (bottom).

RMSE on 11 CP (10 GCP used in BBA)									
Software	**EyeDEA**			**PM**			**PS**		
	DX (m)	DY (m)	DZ (m)	DX (m)	DY (m)	DZ (m)	DX (m)	DY (m)	DZ (m)
RMSE	0.019	0.018	0.041	0.030	0.035	0.086	0.032	0.026	0.056
RMSE on 15 CP (6 GCP used in BBA)									
	DX (m)	DY (m)	DZ (m)	DX (m)	DY (m)	DZ (m)	DX (m)	DY (m)	DZ (m)
RMSE	0.020	0.019	0.039	0.043	0.043	0.083	0.031	0.037	0.050

Using 10 GCPs, the RMSE for all programs varies between 2 and 4 cm horizontally, and from 4.1 cm (EyeDEA) to 8.6 cm (PM). Using 6 GCP only the horizontal errors of PS and PM are larger, while the vertical ones slightly improve. Overall, the EyeDEA results have the smallest variation between the two configurations. On the contrary, the PhotoModeler performance was the worst, with the RMSEs of the height coordinate greater than the GNSS analogous accuracy. Thus, this aspect should affect the DSM and, consequently, the volume estimate in PhotoModeler.

6.2.3. Digital Surface Model production

The software performance was further compared by generating point clouds from blocks oriented with both GCP configurations.

The block oriented with the EyeDEA + PM workflow was processed in another in-house program named "Dense Matcher" [96] that implements the Least Squares Matching (LSM) algorithm [56]. A point cloud is generated for every pair of images. All three dimensional point data need to be registered together: this is done in a 3D modelling program using the overlaps between models. Finally, the combined point clouds are interpolated on a regular grid using a Delaunay triangulation.

In PhotoModeler, the appropriate “Create Dense Surface” tool was employed. It allows the user to select the image pairs and set other criteria such as the base-height ratio, the maximum acceptable point residual, the minimum number of homologous points between pairs and the maximum angle between adjacent images. After the point cloud creation, manual editing was necessary to remove some gross errors.

Lastly, the point cloud generation in Agisoft PhotoScan was less laborious and a unique model of the whole image block was obtained automatically.

Because of the huge amount of 3D points, a decimation phase was required for reducing the computation effort (and time), otherwise ArcGIS would not have been able to handle the datasets. Indeed, after this decimation procedure in MeshLab, ArcGIS Desktop 10.0 was employed to interpolate the 3D points on a grid mesh of 2 cm.

6.2.3.1. DSM comparisons

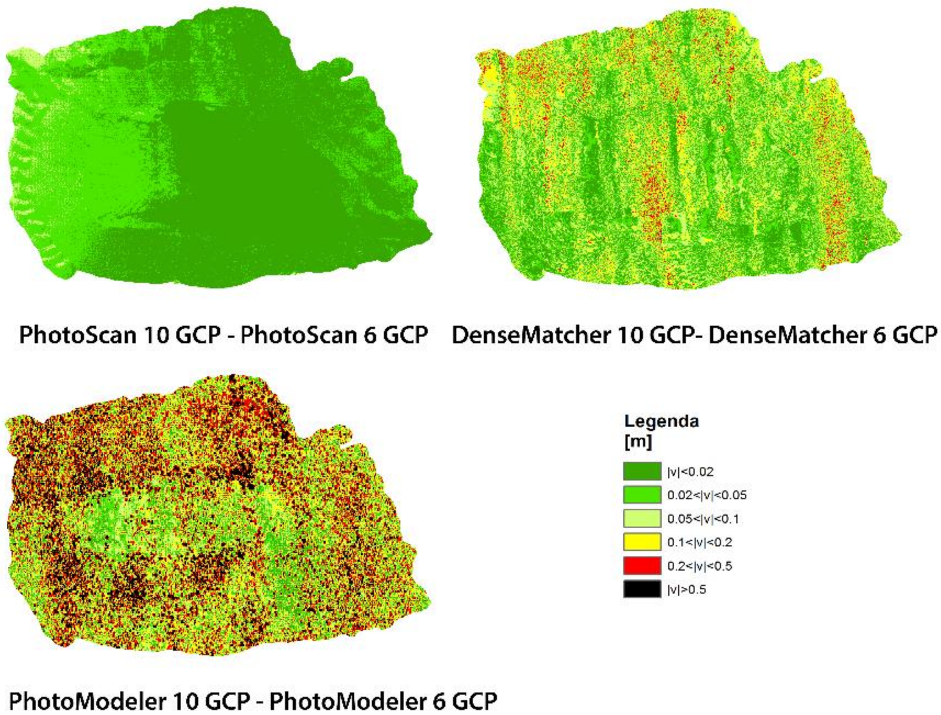

Figure 6.2.5 – Differences between the DSMs generated by the same software with the two configurations of GCPs. From top to bottom, left to right: Agisoft PhotoScan, Dense Matcher and PhotoModeler

Neither a more precise DSM nor an exact volume value to be used as reference data were available at the time of this work: hence, comparisons were necessarily performed only between the generated DSMs. A mask was created and applied to the models in order to isolate the mineral deposit area and focus the analyses on it.

A first visual analysis shows that the Dense Matcher DSM was affected by some disparities caused by the union of the several models. PS was able to create a complete and smooth DSM, whereas the PM product is noisy and irregular.

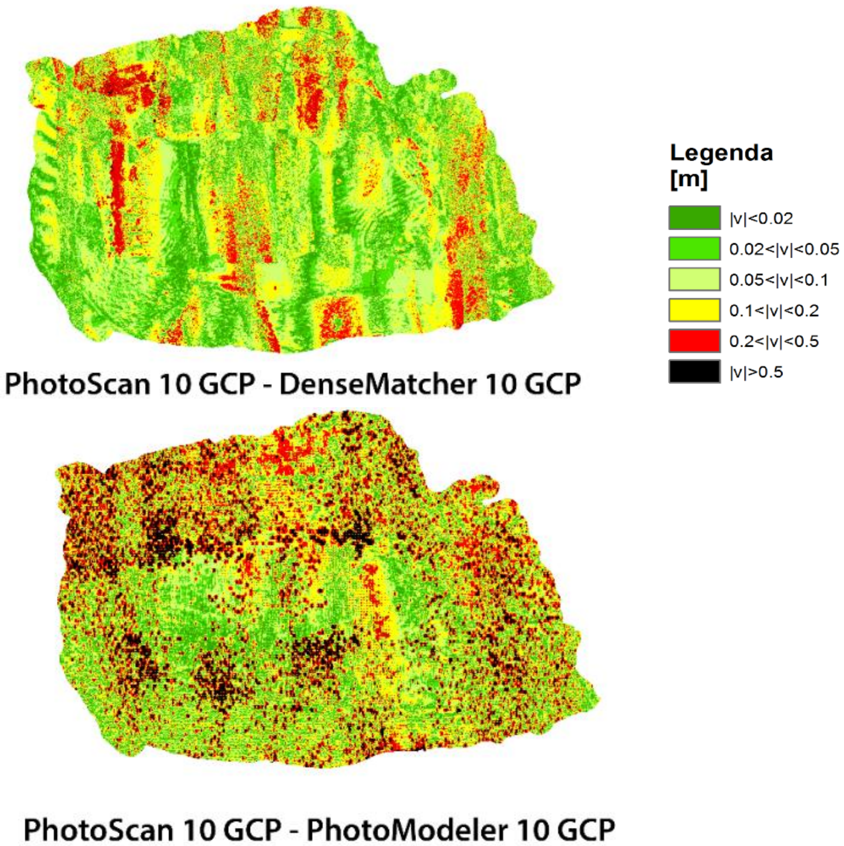

Figure 6.2.6 – From top to bottom: differences between the Agisoft PhotoScan model and, respectively, Dense Matcher and PhotoModeler (configuration with 10 GCPs).

Figure 6.2.5 illustrates the differences between the DSMs generated by the same software with the two configurations of GCPs. It can be easily noted that the PM products are both very noisy and characterized by point differences of some meters, because of the presence of outliers. Concerning DM, the differences pattern is due to the various point clouds of image pairs, thus to the implemented modelling method. Instead, PS supplied similar DSMs, which seem congruent to each other: only small differences of absolute value equal to maximum 10 cm are detectable.

The differences between DSMs were also computed for the 6 GCP configuration, obtaining analogous results.

The PS DSM was assumed as reference model thanks to its smoothness and regularity and the comparisons confirmed what has already been observed. Indeed, local differences with the PhotoModeler DSM are visible in Figure 6.2.6 this means that after the generation of the DSM, the user should perform a manual or automatic editing to remove outliers.

The pattern of the PS-DM differences hints that discrepancies are caused by problems in the alignment of the individual point clouds.

6.2.4. Volume Estimate

As already said, a reference volume value was not available. However, the gravel pile is located over a flat platform: thus, a reference horizontal plane was estimated by employing the minimum GNSS height of the targets placed around the pile. The volumes of the six DSMs were computed with respect to this horizontal plane (Graph 6.2.1).

A discrepancy between the PM values and the others is evident but, without a reference value, it is not possible to say what software provided the best assessment.

VOLUMES

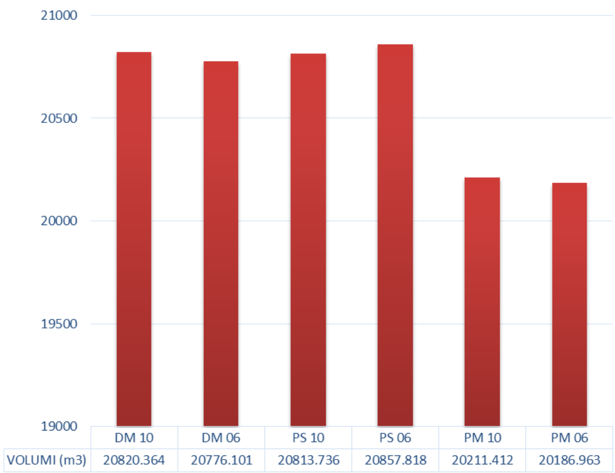

Graph 6.2.1 – Estimated Volumes for each software in both GCP configuration. From left to right: Dense matcher, Agisoft PhotoScan and PhotoModeler.

Table 6.2.6 summarizes the differences between the volumes of the two configurations for each software. The normalised differences are lower than 0.2%. The influence on volume estimate of the two GCP configurations is therefore negligible and it is enough to have a good distribution of GCPs, positioned at the extremities of the strips and around the pile but not on its top.

Table 6.2.6 – Differences in each software between the volumes computed for the two configurations of GCPs.

CONFIGURATION 10 GCP - CONFIGURATION 6 GCP		
SOFTWARE	VOLUME DIFFERENCE	
	(m^3)	(%)
Dense Matcher	44.26	0.21
PhotoModeler	24.45	0.12
PhotoScan	-44.08	-0.21

Taking again as reference the PS DSM, the smoothest and visually not affected by gross errors, the volume variations of the configuration with 10 GCPs are reported in Table 6.2.7.

Table 6.2.7 – Differences between the Agisoft PhotoScan estimated volume, respectively, the Dense Matcher and PhotoModeler ones.

	CONFIGURATION 10 GCP		CONFIGURATION 6 GCP	
SOFTWARE	VOLUME DIFFERENCE		VOLUME DIFFERENCE	
	(m^3)	(%)	(m^3)	(%)
PS - DM	-6.63	-0.03	81.72	0.39
PS - PM	602.32	2.89	670.86	3.22

The PS and PM values differ significantly (more than 600 m^3), whereas Dense Matcher volumes similar to the PS ones, with a difference of only 7 m^3 for the more constrained configuration. Anyway, it should be observed that, even if the results are comparable, Agisoft PhotoScan is almost fully automated and its computation time is definitely lower than that required by the in-house programs EyeDEA and Dense Matcher.

6.2.5. Conclusions

It is not possible to state that one software package outperformed the others in the volume assessment, since a reference value is not available. However, while two programs estimate the volume with a very good agreement (better than 0.4%)

the third show discrepancies up to about 3%. This suggests that a benchmark for testing UAV software packages in different applications should be useful.

Overall, the PS outperforms the other programs in smoothness of the workflow, processing time and visual quality of results. Although a little information is available on the PS algorithms, its results seem reliable since are comparable with those of EyeDEA/Dense Matcher, whose algorithms are well known and well tested. Smoothing of inconsistencies (data gaps, outliers, model alignment, etc.) needs improvements in both PhotoModeler Scanner and DM.

In this particular block, the influence of GCPs number and distribution on the photogrammetric workflow, thus on the volume estimate, turned out to be minor, with differences less than 0.2% of the volume for all programs.

A final remark, that underlines how UAV photogrammetry might be unique in some circumstances, is about getting reference data for the pile volume. A topographic survey with a Terrestrial Laser Scanner would have been indeed impractical, very time consuming and expensive. Third show discrepancies up to about 3%. This suggests that a benchmark for testing UAV software packages in different applications should be useful.

6.3. Gran Sommetta Rock Glacier

Monitoring the surface creep of mountain permafrost is important to understand the effect of on-going climate change on slope dynamics. Rock glaciers in particular are landforms that can show rapid acceleration and destabilization [29]. In the Alps, the accelerating creep of perennially frozen talus/debris with high ice content has already brought problems to high mountain infrastructures [62] and the situation is only likely to get worse. However, traditional techniques (e.g. repeated GPS surveys of a set of points) cannot easily be applied in such scenarios: the glacier surface is rough and presents hazards like crevasses. Only operators with adequate training can carry out a survey in such environment. On the other hand, though continuous point-wise tracking with low cost GPS is feasible, even employing several receivers the velocity field of a glacier would not be properly estimated.

This study presents the evaluation of movements and volumetric changes of a rock glacier, obtained by multi-temporal analysis of UAS images over the period 2012-2015. The movement rate obtained by photogrammetry is validated against repeated GNSS campaigns on 48 points distributed on the rock glacier.

6.3.1. Study area

The study area is located in the western Alps at the head of the Valtournenche Valley (Valle d'Aosta, Italia) on the Italian side of Matterhorn. The body of the rock glacier is composed by two lobes, spanning an elevation range between 2600 and 2750 m. It is nearly 400 m long, between 150 and 300 m wide and has an apparent thickness (based on the height of the front) of 20-30 m. Since 2012, the surface movements of the glacier are monitored by ARPAVdA as a case study for the possible impact of climate change on high-mountain infrastructures: in fact, this glacier juts on a ski slope of the Cervinia resort, and repair or maintenance works are necessary every year. For these reasons, a multi-sensor monitoring system, based on repeated UAS-photogrammetry and GNSS survey as well as collection of meteorological data, has been setup. The current dataset of observation consists of three UAS flights (October 2012, October 2014 and July 2015) and three GNSS campaigns (mid-August 2012, 2013, 2014).

The advantage of using both GNSS and UAV is in their complementarity. On one hand, GNSS gives measures of surface displacement with high accuracy, but just on few points (48 in this study). On the other hand, the UAS-photogrammetry provides a dense cloud of points, which allows (i) describing in detail the whole surface producing high-resolution DSM and (ii) high resolution orthophotos to evaluate the glacier displacements.

The GNSS data can be used as ground truth for validating the displacement obtained by orthoimage analysis and DSM comparison and check the accuracy of the monitoring system.

6.3.2. UAS photogrammetry

Due to the site characteristics, where strong wind is common and weather conditions change quickly, the UAS employed is the fixed-wing SwingletCAM produced by SenseFly (for more detail see 2.6.4) that can complete a survey mission over the extended area in a single flight in about 20 minutes.

The SwingletCAM was equipped with a 12 Mpixel CANON IXUS 220 HS camera for the 2012 flight, and with a 16 Mpixel CANON IXUS 125HS camera for the 2014 and 2015 flights. The former flight was performed at a relative elevation of 150 m with a forward overlap of 60% and a sidelap of 70%, with a GSD of 5 cm. The number of images acquired and used in the bundle block adjustment was 110. For the 2014 and 2015 flights, the same GSD was obtained changing slightly the flight altitude. At the same time, on the basis of MC 1 simulation results (see 2.6.4 for more details), to make the image block more rigid, the forward and side overlap were respectively increased to 80% and 85%. Given the flight characteristics, the images acquired in the photogrammetric block were 246 and 192 respectively for the 2014 and the 2015 flights. Table 6.3.1 summarises the design parameters of the two UAS flights.

Table 6.3.1 – Summary of the UAS flights characteristics.

	2012	2014	2015
Date	October 24th	August 18th	August 18th
N° images used	110	246 (two flights)	192 (two flights)
Side overlap	70%	80%	80%
Forward overlap	60%	85%	85%
GSD	5 cm	5 cm	5 cm

Figure 6.3.1 – Type of signalized marker for Ground Control Point.

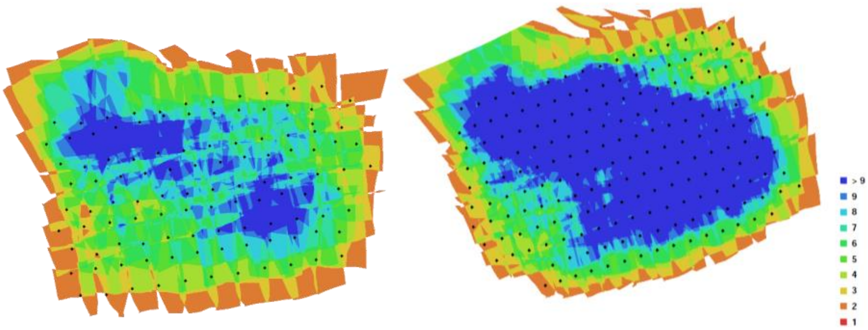

Figure 6.3.2 – Camera location and image overlap of 2012 flight (on the left) and of the 2015 flight (on the right).

The increase of forward and side overlap is visible in the colour map of Figure 6.3.2.

6.3.3.Ground data acquisition

In order to properly register the DSM at every epoch, 19 Ground Control Points distributed on the edges of the rock glacier area were materialized: the GCPs location is shown in Figure 6.3.3.

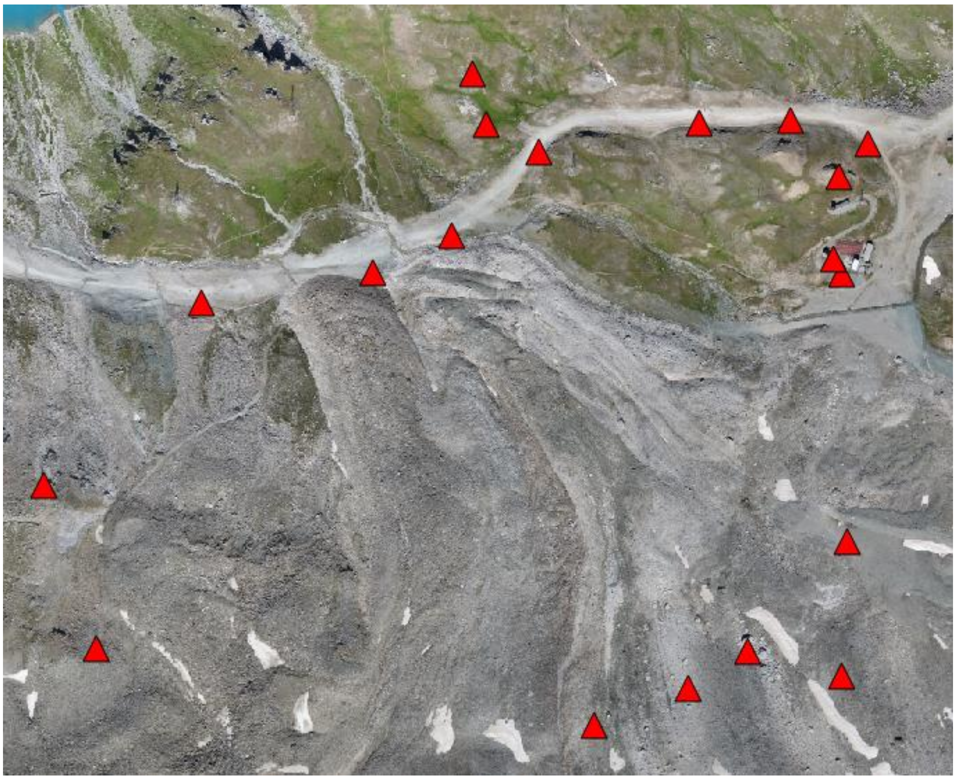

Figure 6.3.3 – Location of GCPs.

The GCPs located in the area were signalized with ad hoc targets, namely black and white square panels with side of 30 cm and triangular pattern as in Figure 6.3.1. These control points were measured with a GNSS receiver GEOMAX Zenith 20 Series in RTK mode. The expected precisions in XY coordinates are 1-2 cm and 2-3 cm in Z.

6.3.4. Data processing

The bundle block adjustment and the consequent dense surface reconstruction of the UAS surveys were performed with the commercial software Agisoft PhotoScan.

Since the images were taken with consumer grade compact cameras, whose optics are usually not very stable, a self-calibration procedure was used in the image orientation process. Even if the on-board navigation system provides the camera locations, their accuracies were too low for correctly co-register the DSM at the different epochs, and the GCPs were preferred to orient the photogrammetric blocks. Finally, to validate the DSMs accuracy, 48 GNSS check points (depicted Figure 6.3.4) were used to check the elevation discrepancies between GPS measurements and photogrammetric surface reconstruction (Table 6.3.2).

Table 6.3.2 – Statistics of the comparison between the GNSS elevation data and the photogrammetric reconstructed DSM for the 2012, 2014 and 2015 flights.

Date	2012	2014	2015
Mean (m)	0.103	0.025	0.022
St. Dev. (m)	0.110	0.156	0.140
N° GNSS points	48	46	44

These DSM check points were measured with a GNSS receiver Leica Viva GS10/15 in RTK mode, with an expected precision of ca. 1 cm. The points were materialized using fluorescent spray paint and drilling a small pilot hole on the rock surface for the GNSS pole. Despite being painted, the points are not clearly recognizable in the UAS images and so their GPS coordinates were compared with the DSM surface. Anyway, the standard deviations of the differences are in good agreement with the theoretical precision computed during image block design. To limit the number of images, a GSD of ca. 5 cm, which provide a final theoretical precision of ca. 8.5 cm for both flights, was considered optimal. The results of the comparison are good, considering also the ground resolution (of 5 cm) of the photogrammetric reconstructed digital models, and the estimated precision of the GNSS survey (comparing the measures on fixed point an accuracy of ca. 5 cm was found). However it is important to highlight the mean value of the differences revealed from the statistics of the 2012 flight: in this case the observed 10 cm can be probable due to a systematic error source between the GCP and GNSS measurements.

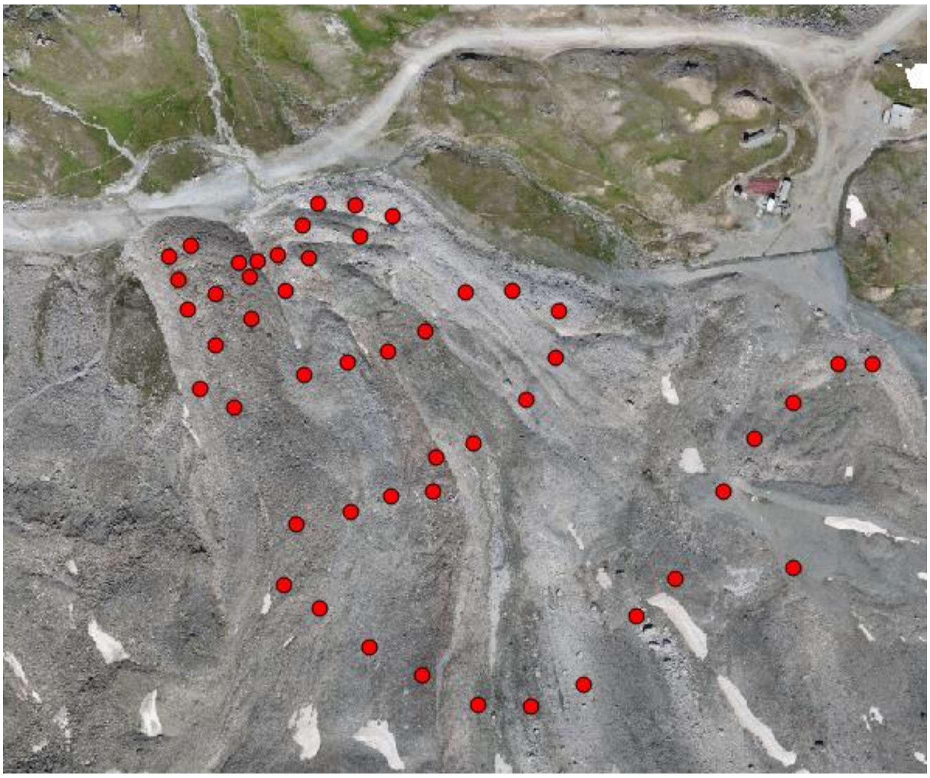

Figure 6.3.4 – Localization of the 48 GNSS measured points.

6.3.4.1.Summer 2015 campaign

On the basis of the annual survey campaigns, in view of the monthly surveys to be performed during the Summer 2015, a study has been carried out to optimize the number of GCP, limiting their number to reduce survey time and survey cost. The aim was to get, from the comparison of two monthly campaigns, a displacement precision of 5 cm (1/3 of the expected displacement) using the minimum number of GCP.

A simulation has been performed with a synthetic block with forward and side overlap of 80-80% and a relative height flight of 140 m. Precisions of ground coordinates were calculated through the BBA covariance matrix in two configurations:

a) 23 GCP distributer over the whole area;
b) 9 GCP on the boundary of the area.

The simulations were executed considering a precision of the tie points of 0.5 pixel.

Table 6.3.3 – Statistics of the ground coordinates for the two BBA configurations.

	23 GCP			9 GCP		
	X (m)	**Y (m)**	**Z (m)**	**X (m)**	**Y (m)**	**Z (m)**
Mean	0.019	0.020	0.042	0.020	0.021	0.044
Std. Dev.	0.011	0.011	0.027	0.011	0.011	0.027

From the summary of the simulations shown in Table 6.3.3 it is apparent that there is no substantial difference due to the high redundancy of the blocks.

Based on these results, the July and August campaigns were flown with high overlap, the other flights parameters are summarised in the Table 6.3.4.

Table 6.3.4 – Summary of the UAS flights parameters for the July - August 2015 flights.

Date	**July 2015**	**August 2015**
N° images used	189	189
Side overlap	80%	80%
Forward overlap	85%	85%
GSD	5 cm	5 cm

The BBA was performed using only 9 GCP, as suggested by the simulations.

In Table 6.3.5 statistics of the July and August 2015 BBA on 9 CPs are illustrated. The July residuals are higher than in August but substantially of the same order of magnitude.

Table 6.3.5 – Statistics of the 9 CPs residuals for the July and August 2015 flights.

CONFIGURATION 9 GCP – RESIDUALS ON 9 CP

Date		**DX (m)**	**DY (m)**	**DZ (m)**
July 2015	**Mean**	-0.002	0.006	0.021
	St. Dev.	0.016	0.027	0.056
	RMSE	0.016	0.027	0.060
August 2015	**Mean**	-0.009	-0.003	0.028
	St. Dev.	0.027	0.007	0.031
	RMSE	0.029	0.007	0.042

It is interesting to compare the RMSE of this block and those of the Campus 140 m block, with about the same relative flight height and size of the area. Due to the different sample size, this statistic is certainly less significant than that of Campus case study (see paragraph 5.2.4.1 – Flight at 140 m – Table 5.2.4). However, it suggest that thanks to greater (80%) side overlap, the accuracies are better than those of the Campus block with a lower (40%) side overlap.

6.3.5. Conclusions

In this experiment, in collaboration with ARPAVdA, the SwingletCAM UAS was employed to monitor an Italian rock glacier, to evaluate the effects of climate change on permafrost masses, which lately have shown progressive destabilization and fast acceleration in their creep behaviour.

In this context, the use of UAS cuts drastically the periodic survey costs, while allowing to acquire dense geometric data on the glacier shape in both in safety and quickly, avoiding hazards and risks for the operators.

The influence of forward and side overlap on the BBA is evident. Increasing the overlap, especially the side one, improves the ground accuracies and allows to estimates reliably the rock glacier displacements with less ground control points.

The execution of a new measurement campaign of GCPs and CPs ensures consistent georeferencing of the data over time and independent accuracy check of the DSM. However, it requires direct access of a surveyor to the glacier area. Taking into account that annual displacements are large (in the order of 1 m and more), block georeferencing could be alternatively obtained (with less but still enough accuracy) by GPS-assisted AT. Therefore, a primary controlled experiment using a RTK-equipped UAS (e.g. the eBee by SenseFly) was carried out as specified in Section 5.3 if the actual RTK positioning accuracy of UAS is really in the cm range as claimed by manufacturers.

6.4. Veleia Romana

A Historical Geographic Information Systems (HGIS) of the Veleia Romana archaeological site is being populated with historical maps and documentation on findings (now kept in Parma Archaeological museum). Since topographic maps of the site are not up-to-date, the production of a new cartographic layer as well as of 3D models have been foreseen. To this aim, a survey campaign has been performed using integrated techniques such as total station, GNSS, terrestrial laser scanner, aerial and terrestrial photogrammetry.

In the context of this work, the main interest is the use of two UAS platforms employed at quite different relative flight height:

1. a multi-rotor wing Easyfly of Eurodrone (see 2.6.2) flew at 50 m on October 10^{th} 2014;
2. the lightweight drone “SwingletCAM” by SenseFly (see 2.6.4) has flown at 130 and 230 m on October 30^{th}.

Co-registration and fusion of the three blocks have been attempted; in the following, the strategies and tests performed on this account will be discussed.

6.4.1. Study area and data acquisition

The Veleia Romana archaeological site is located on the Italian Apennine in the municipality of Lugagnano Val D'Arda, about 50 km from Piacenza. Its discovery occurred in 1747. To date, what has been unearthed and restored, consists of the forum, the thermae, the basilica, the cistern for collecting water and some areas of the residential district, see Figure 6.4.1.

Figure 6.4.1 – Veleia Romana archaeological site: 1- Forum, 2 - Basilica, 3 – Thermae, 4 – Residential district, 5 - Cistern.

Prior to the survey, several control points were evenly distributed within the area of interest. Different types of point were signalized: (i) survey markers for the topographic network; (ii) large square targets for the aerial photogrammetric surveys; (iii) circular targets for the terrestrial laser scans (see Figure 6.4.2).

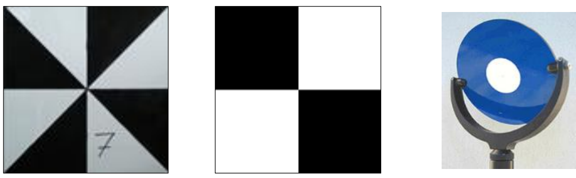

Figure 6.4.2 – Photogrammetric targets (left and centre) and laser scan target (right).

The surveying network was measured with a total station Topcon IS203 to determine the photogrammetric markers used as GCPs in UAS flights with an estimated accuracy of 1 cm.

Two GNSS double-frequency receivers Leica (1230 and SR500) with geodetic antennas were used in static relative positioning, reoccupying stations points of the surveying network in order to convert the coordinates from the local reference system to global reference system WGS84 – ETRS 2000 datum (UTM projection).

The laser scanning survey was performed by a Leica C10, georeferencing the point clouds using the survey network stations.

In order to obtain a high resolution survey, the multi-rotor has been used, equipped with a compact mirror-less Samsung NX1000 (Sensor APS c) with a resolution of 20.3 Mpixel, image frame 23.5 × 15.7 mm and a fixed focal length of 16 mm. It flew in autonomous mode using waypoints of a pre-planned flight at 50 m of relative flight height and with 80-60% forward and side overlap. The GSD is 1 cm. With about 15’ of flight endurance, 6 missions were necessary to complete 6 E-O oriented strips, 3 N-S oriented strips and 1 transversal strip for a total of 68 images (see Figure 6.4.3). This flight (Flight 1 hereinafter) will be used to generate the restitution products for the archaeological site HGIS.

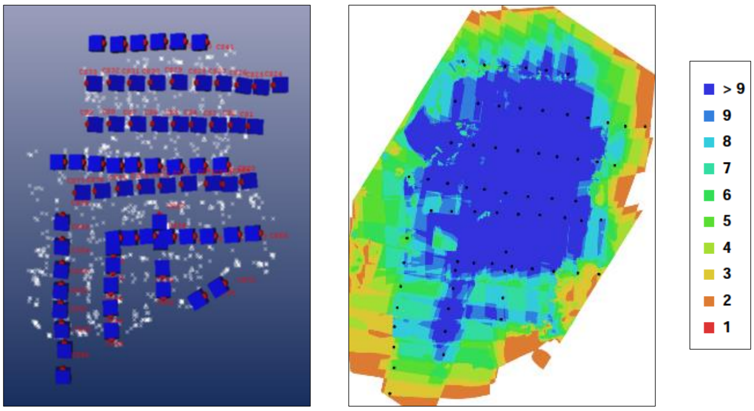

Figure 6.4.3 – On the left camera locations, on the right image overlap of the Flight 1.

The SwingletCAM, having long endurance, was used to survey an extended area (up to 100 Ha). It was equipped with a 16 Mpixel Canon IXUS 125HS compact camera with a RGB sensor and focal length of 4.3 mm used in the Flight 2 at 130m relative flight height. Two more flights were executed with a 16 Mpixel Canon PowerShot ELPH 110 HS with a NIR sensor and 4.3 mm focal length: Flight 3 at 130 m relative flight height and Flight 4 at 230 m relative flight height. The forward and side overlaps were maintained for each SwingletCAM flight to 80-80%. Flight 2 and Flight 3 span over a 40 Ha area with 7 E-O oriented strips;

Flight 4 covers an area of 100 Ha with 7 E-O oriented strips. The SwingletCAM flights were performed to test the platform.

Table 6.4.1 summarises the parameters of each flight.

Table 6.4.1 – Summary of the UAS flight characteristics.

Name Flight	**Flight 1**	**Flight 2**	**Flight 3**	**Flight 4**
Drone	EASYFLY	SwingletCAM	SwingletCAM	SwingletCAM
Relative height flight (m)	50	130	130	230
N. Images acquired	68	97	95	147
Side overlap (%)	60	80	80	80
Forward overlap (%)	80	80	80	80
Camera	NX 100	IXUS 125 HS	PowerShot ELPH 110 HS	PowerShot ELPH 110 HS
Spectral Range	RGB	RGB	NIR	NIR
GSD (m/pixel)	0.01	0.04	0.04	0.07
Area (km^2)	0.007	0.4	0.4	1.4

6.4.2. Block orientation

The availability of flights at different resolutions and of imagery of different spectral range posed the problem of joining the information to make geospatial data consistent with each other.

The UAS imagery were processed in two ways:

a) Each block has been oriented, georeferenced and processed separately for DSM and orthophotos generation.
b) An attempt has been made to orient simultaneously all flights into a single block.

In case a) the BBA and the dense surface reconstruction were performed with the commercial software Agisoft PhotoScan. Since the images were taken with consumer grade compact cameras, whose optics are usually not very stable, a self-calibration procedure was used in the image orientation process. The blocks were georeferenced with the collimation of the GCPs. In particular, for Flight 1, markers were used as GCP. Lower resolution flights where georeferenced using natural features determined from the previous Flight 1. It should be mentioned that the SwingletCAM blocks were flown 3 weeks after Flight 1, therefore the markers placed overall the area were removed in the meantime.

6.4.2.1. Simultaneous orientation of different blocks

To join all UAS imagery into a single block, they were at first imported in PS in order of increasing GSD: from Flight 1 to Flight 4. The automatic orientation of the 407 images failed. Then, the EO parameters of the separate orientation of the flights were imported in PS in order to give an initial solution: only the Flight 1 images were successfully oriented.

Table 6.4.2 – Summary of the performed test.

TEST	CONFIGURATION
1 - RGB	Flight 1 + Flight 2
2 - Relative height flight	Flight 2 + Flight 3
3 – NIR	Flight 3 + Flight 4
4 - SwingletCAM	Flight 2 + Flight 3 + Flight 4
5 – ALL	Flight 1 + Flight 2 + Flight 3 + Flight 4

Since the attempt failed, other software packages were tested: PhotoModeler Scanner, VisualSFM [131], and open access numerical codes implementing SIFT operator [76] as autopano-sift in C# [89] or VLfeat in Matlab [125]. However, none of the packages has been able to orient all images at once.

In order to gain a better understanding of the difficulties found by feature extraction algorithms, a more articulate test sequence has been devised, as summarized in Table 6.4.2.

Test 1 attempts to join the RGB flights, using only image pairs framing the same area. The same results were obtained by all programs: after feature extraction on each image, the matching between images across flights produced too few inlier (just an average of 35 common points, while normally they number in thousands) to allow automatic orientation. The homologous points on some image pair were plotted to find out and, astonishingly, some of the point labelled as inlier were in fact erroneous (see Figure 6.4.4).

Image pairs were successfully oriented only if belonging to the same flight, as visible in

Figure 6.4.5.

Considering the flights parameters (relative height flight and focal length), the scale ratio for the Flight 1 and Flight 2 is about 1:10. On the other hand, considering the GSD, the ratio is 1:4. Even though, as well known, the SIFT operator is scale-invariant, it was decided to reduce the resolution of Flight 1 images in order to obtain the same GSD as Flight 2 images.

Also in this case, not enough homologous points where found to succeed in the automatic orientation.

Figure 6.4.4 – The homologous points found between images of Flight 1 (top) and of Flight 2 (bottom): the erroneous match, highlighted by red arrows, regards a feature located in the Forum for the Flight 1 and in the Cistern in the Flight 2.

Summarizing the various attempts, it is likely that, since the two flights were made in different days and times of day, the differences of shadows and illumination actually lead to failure of joint automatic orientation of the two RGB flights.

The only way to successfully orient together Flight 1 and 2 has been to take advantage of their separate previous orientation in PS. The tie points of both blocks were decimated with an ad-hoc developed code in order to have an average of 40 well-distributed 3-rays points on each photo. Then, the GCPs and additional tie points were collimated manually in PM to connect the two blocks that were finally oriented into a single one (see Figure 6.4.6).

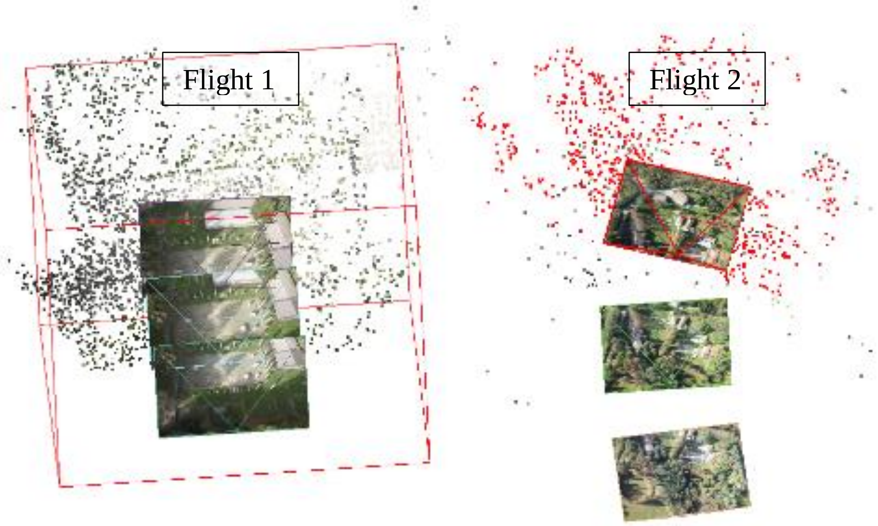

Figure 6.4.5 – Test 1- RGB: the images of Flight 1 and Flight 2 were oriented in two distinct models in VisualSFM after the automatic orientation.

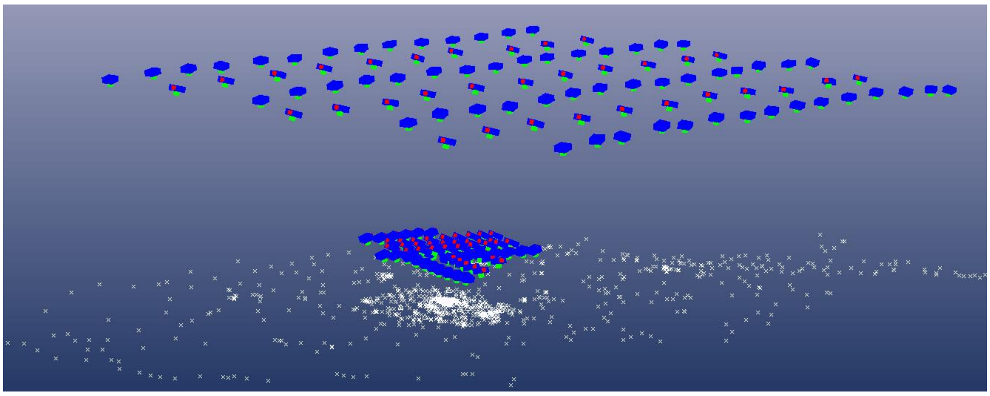

Figure 6.4.6 – Test 1 RGB: Flight 1 and Flight 2 oriented in a single block in PhotoModeler Scanner after manual collimation of some tie points and input of EO parameters extracted from separate PhotoScan orientations.

The second, the third and fourth tests are all about orientation of images acquired by the SwingletCAM, with the same or with a different camera.

In particular, Test 2 consists of automatic orientation between the Flight 2 (RGB) and Flight 3 (NIR) at the same relative flight height.

In Test 3 NIR images were taken from the same camera at different altitudes.

Test 4 includes all the SwingletCAM imagery.

Every test was successfully completed by VisualSFM, PhotoModeler Scanner and Agisoft PhotoScan performed the simultaneous automatic orientation of the blocks.

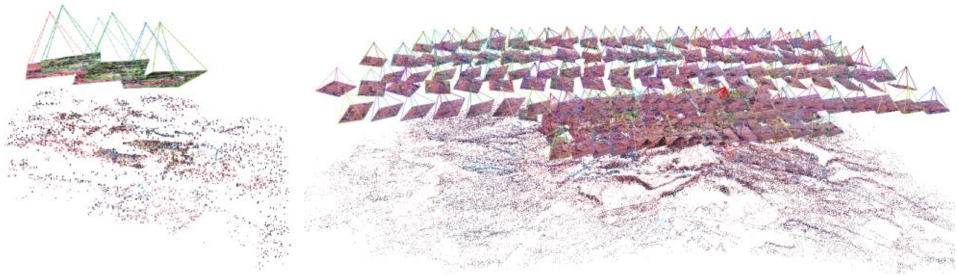

Figure 6.4.7 – Camera locations and 3D points of the flights automatically oriented: on the left, Test 2 – Relative Height Flight, on the right Test 3 – NIR.

The last test (T5 – ALL) involved a subset of the four flights with images framing the same area. In particular, three images were chosen from each flight.

As expected from the results of previous tests, the automatic orientation creates two distinct models: one consisting of the nine images taken by the fixed wing flights and the other comprising the three images taken by the multi-rotor (see Figure 6.4.8. and Figure 6.4.9).

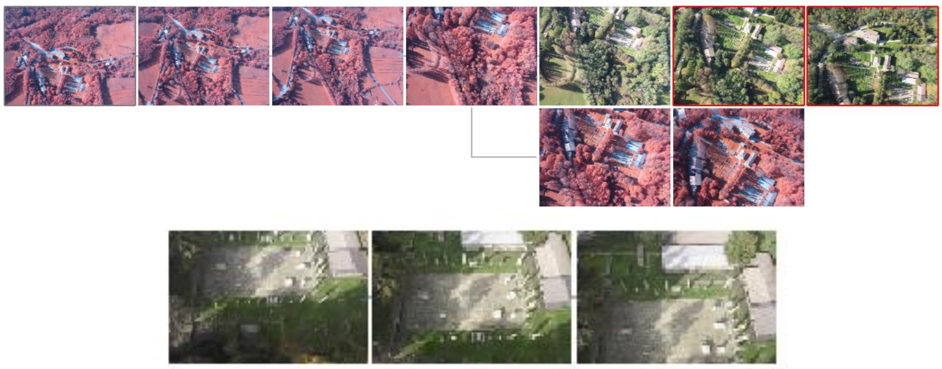

Figure 6.4.8 – Test 5 - ALL: Link between images after the process of automatic orientation. In the upper part, the connection found between the nine images of the SwingletCAM, in the lower part the isolated three oriented images of the Easyfly.

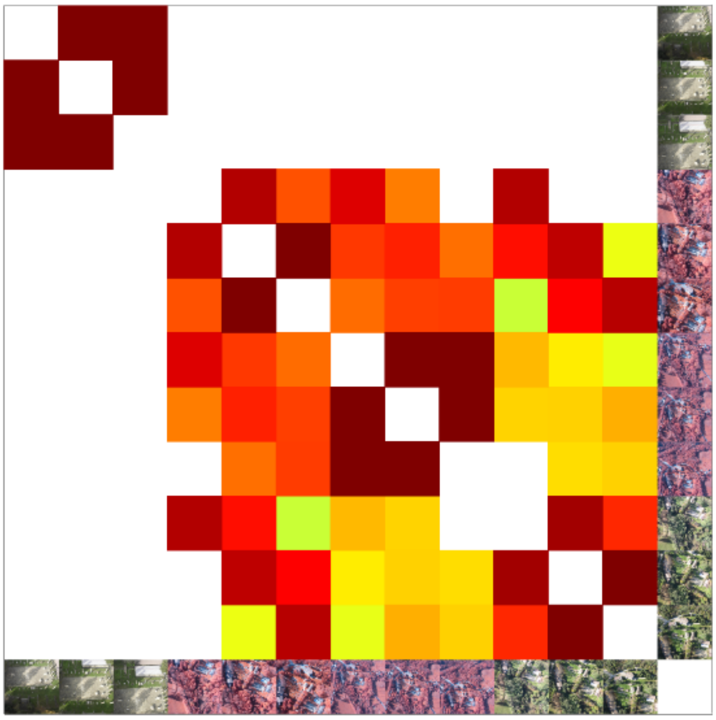

Figure 6.4.9 – Colour map of the connection matrix between the twelve images of the 4 flights after the automatic orientation in Test 5 - ALL: the brown to white colour scale indicates a decreasing number of correspondences (from high to none). The images of the Flight 1 have high correlation each other but none with SwingletCAM flights.

It can be noticed from the connection matrix that a high number of correspondences occurs within the "homogeneous" groups of three images (same Flight). Even a moderate scale difference however make it more difficult to get matches: indeed, the number of connections is higher between the same-scale NIR and RGB images than between the NIR different-scale images.

6.4.3. Conclusions

In this experiment, a multi-rotor Easyfly and a fixed-wing SwingletCAM were available for UAS photogrammetry in cultural heritage documentation.

The multi-rotor drone is indeed a valid platform for very high resolution surveys, though, for an area not exceeding 0.10 km^2, several missions and battery changes were necessary.

On the other hand, the fixed-wing platform is better suited for surveys over extended areas at high relative flight elevation.

A combination of survey flights at different resolutions and with different sensors has been executed. Each flight was oriented in Agisoft PhotoScan and the georeferencing was made by manual collimations of GCPs (signalized marker and natural features). However, trying a joint orientation of all blocks proved unfeasible with PS and other programs: only by manual measurement could the Easyfly block be tied to the SwingletCAM one.

A series of test hints that shadows and illumination differences are the strongest stumbling block that might prevent any successful matching of features; scale differences are another factor that reduce the number of correspondences, though a ratio 1:2 is certainly manageable.

Conclusions

Starting from the last decade, there was a dramatic increase in the use of Unmanned Aircraft Systems (UASs) in Photogrammetry and Remote Sensing (PaRS) for applications such as environmental monitoring, cultural heritage, surveillance and many other.

However, specific guidelines for UAS survey flights have not yet been established and investigations are still needed to assess the accuracies that such imagery can reach for metric purposes. Many software package for UAV photogrammetry exist today, born either in CV or in a photogrammetric environment. This difference in background means that the output documentation is different and that differences exist in the product accuracy and completeness, as the comparisons made in Chapter 6 have shown. This suggests that a benchmark for testing UAV software packages in different applications should be established and that some standard on processing reports should be promoted.

Being the UAV world a quite articulated one, relationships between accuracy on ground and parameters such as image scale, side and forward overlap, GCP distribution are hard to optimize as in aerial blocks with analogue cameras. On this regard, a methodological study has been carried out with Monte-Carlo simulations on georeferencing UAV blocks with GCP and GPS on board. The results show that UAV blocks, with respect to aerial photogrammetric cameras, have to compensate with higher overlaps the lower quality of the sensor and of the navigation system. This grants a greater rigidity against random error unfavourable accumulation if multi-image matching is used; moreover, a reduced number of GCP is necessary to control the BBA. Furthermore, the general acceptance in practice of large side overlaps and the transition to multi image matching in Dense Matching seem to close the gap between adjustment methods including GCP in the BBA and CV methods based on a two-step procedure and to a gain of uniformity of restitution precision over the whole block. The accuracy potential of UAS photogrammetry both for very large scale mapping as well as, perhaps more interestingly, for periodic monitoring of decimetre-level displacements in environmental applications is certainly large.

It must be noticed, however, that empirical tests on Parma University Campus as well as on the Gran Sommetta rock glacier, where DSMs produced from the same block but adjusted with a different control (number of GCP or GPS-determined camera station) show systematic discrepancies larger than the expected accuracy. This points out that other (non-random) unmodelled error sources might be present in UAS block and that quality checks should be well focused.

As far as error sources are concerned, inaccurate interior orientation data (including lens distortion) are likely to be the first that should be examined. Their effect should be identified with additional empirical and simulated tests, which are even more important now that promising results are coming from GPS-assisted blocks, where it is well known that IO residual errors are passed to ground coordinates rather than being adsorbed by EO parameters. Results on using pre-calibration or self-calibration or a mix of the two is not yet clear-cut.

As far as quality checks are concerned, even a fair number of CP might not be enough for such systematic differences being noticed or clearly highlighted; therefore, a sensitivity analysis on the effect on the DSM of changes in exterior orientation and interior orientation should be performed.

Getting rid of Ground Control Points by using GPS-Assisted Aerial Triangulation or even Direct Georeferencing is probably currently the real hot topic for a fair range of applications of UAS photogrammetry. The GPS accuracy requirements and their vulnerability to gross errors have also been investigated with Monte Carlo simulations. The research outcomes indicate that expected performance is very good but that L1/L2 receivers are necessary for a reliable operational system. Specifically, due to high overlaps, the covariance propagation from the receiver to the ground is quite favourable and the solution accuracies are comparable with those obtained with georeferencing with GCP. Furthermore, thanks to the high multiplicity, the recognition of gross errors, which also affect a significant portion of the block, is possible.

The results of an empirical test with GPS on board described in Section 5.3, tough of limited significance due to the small number of CP, suggest that the same accuracy level can be reached on the ground and that this is true for the DSM generation. In other words, the technology seems indeed matured to an operational level. More testing is however needed to consolidate the confidence on such results and study the conditions that guarantees such accuracy.

For their performance, UAVs have already conquered a prominent position in the field of photogrammetry. When georeferencing using GPS in RTK mode will have achieved a sufficient degree of reliability, perhaps making use of the permanent stations networks, their role is certainly destined to grow even more.

Bibliography

1.Abbeel, P., Coates, A., Quigley, M., & Ng, A. Y. (2007). An application of reinforcement learning to aerobatic helicopter flight. In: *Advances in neural information processing systems, Vol. 19*, 1.

2.Ackermann F. (1988): Combined adjustment of airborne navigation data and photogrammetric blocks. In: *ISPRS – International Archives of the Photogrammetry, Remote Sensing and Spatial Information Sciences, Vol. XXVII-B8*, *Comm. III*, Kyoto, pp. 11-23.

3.Ackermann, F., & Tsingas, V. (1994). Automatic digital aerial triangulation. In *ASPRS/ACSM Annual Convention Reno*, pp. 1-12.

4.Agisoft PhotoScan, 2014. Algorithms used in Photoscan, http://www.agisoft.ru/forum/index.php?topic=89.0 (last access 20/10/2015).

5.Air Photo Service Co. Ltd., Japan 2011.http://cryptome.org/eyeball/daiichi-npp/daiichi-photos.htm#20 March (last access 03/11/2015).

6.Annen, S. & Nebiker, S. (2007): Einsatz von Mikro- und Minidrohnen für Fernerkundungsaufgaben in der agrochemischen Forschung und Entwicklung. *GEOMATIK SCHWEIZ, Vol. 105(6)*, p. 288.

7.ArduPilot, 2015. Ardupilot/APM, http://ardupilot.com/ (last access 18/10/2015).

8.Arya, S., Mount, D. M., Netanyahu, N., Silverman, R., & Wu, A. Y. (1994, January). An optimal algorithm for approximate nearest neighbour searching in fixed dimensions. In *ACM-SIAM SYMPOSIUM ON DISCRETE ALGORITHMS*, pp. 573-582.

9.Baiocchi, V., Dominici, D., & Mormile, M. (2013). UAV application in post-seismic environment. In: *ISPRS – International Archives of the Photogrammetry, Remote Sensing and Spatial Information Sciences, Vol. XL-1 W2*, pp. 21-25.

10.Baltsavias, E. P., (1991). *Multiphoto geometrically constrained matching*. Ph.D. thesis, Institute of Geodesy and Photogrammetry, ETH Zurich, Switzerland. 221 pages.

11.Bláha, M., Eisenbeiss, H., Grimm, D., & Limpach, P. (2011). Direct Georeferencing of Uavs. In: *ISPRS – International Archives of the Photogrammetry, Remote Sensing and Spatial Information Sciences, Vol. XXXVIII-1/C22*, pp.131-136.

12.Barazzetti, L., Remondino, F., & Scaioni, M. (2010). Automation in 3D reconstruction: Results on different kinds of close-range blocks. In: *ISPRS – Commission V Symposium International Archives of Photogrammetry, Remote Sensing and Spatial Information Sciences, Newcastle upon Tyne, UK, Vol. XXXVIII(5)*, pp. 55-61.

13.Barazzetti, L., Remondino, F., Scaioni, M., & Brumana, R. (2010). Fully automatic UAV image-based sensor orientation. In: *ISPRS – International Archives of Photogrammetry, Remote Sensing and Spatial Information Sciences, Vol. XXXVIII(1)*, Calgary, Canada (on CD-ROM).

14.Barazzetti, L., Scaioni, M., & Remondino, F. (2010). Orientation and 3D modelling from markerless terrestrial images: combining accuracy with automation. In: *The Photogrammetric Record, Vol. 25*(132), pp. 356-381.

15.Barry, A. J., Majumdar, A., & Tedrake, R. (2012, May). Safety verification of reactive controllers for UAV flight in cluttered environments using barrier certificates. In: *Robotics and Automation (ICRA), 2012 IEEE International Conference on* (pp. 484-490). IEEE.

16.Bäumker, M., & Przybilla, H. J. (2011). Investigations on the accuracy of the navigation data of unmanned aerial vehicles using the example of the system Mikrokopter. In: *ISPRS-International Archives of the Photogrammetry, Remote Sensing and Spatial Information Sciences, XXXVIII-1/C22*, pp. 113-118.

17. Bäumker, M., Przybilla, H. J., & Zurhorst, A. (2013). Enhancements in UAV flight control and sensor orientation. In: *ISPRS-International Archives of the Photogrammetry, Remote Sensing and Spatial Information Sciences, Vol. XL-1/W2*, pp. 33-38.

18.Bay, H., Ess, A., Tuytelaars, T., & Van Gool, L. (2006). SURF: Speeded Up Robust Features. In: *Computer vision–ECCV 2006* (pp. 404-417). Springer Berlin Heidelberg.

19.Beis, J. S., & Lowe, D. G. (1997, June). Shape indexing using approximate nearest-neighbour search in high-dimensional spaces. In: *Computer Vision and Pattern Recognition, 1997. Proceedings. 1997 IEEE Computer Society Conference on* (pp. 1000-1006). IEEE.

20.Bellingham, J. S., Tillerson, M., Alighanbari, M., & How, J. P. (2002 December). Cooperative path planning for multiple UAVs in dynamic and uncertain environments. In: *Decision and Control, 2002, Proceedings of the 41st IEEE Conference on* (Vol. 3, pp. 2816-2822). IEEE.

21.Bendea, H., Boccardo, P., Dequal, S., Giulio Tonolo, F., Marenchino, D., & Piras, M. (2008). Low cost UAV for post-disaster assessment. In: *ISPRS-The*

International Archives of the Photogrammetry, Remote Sensing and Spatial Information Sciences, Vol. XXXVII (Part B8), 1373-1379.

22.Brown, D. C. (1971). Close-range camera calibration. In: *PHOTOGRAMMETRIC ENGINEERING*, 37(8), pp. 855-866

23.Büyüksalih, G., & Li, Z. (2003). Practical experiences with automatic aerial triangulation using different software packages. In: *The Photogrammetric Record*, *Vol. 18*(102), 131-155.

24.Cina, A. (2000). GPS: principi, modalità e tecniche di rilevamento, Ed. Celid, Torino.

25.Colomina, I., & Molina, P. (2014). Unmanned aerial systems for photogrammetry and remote sensing: A review. *ISPRS Journal of Photogrammetry and Remote Sensing*, *Vol. 92*, 79-97.

26.Cramer, M., Stallmann, D., & Haala, N. (2000). Direct georeferencing using GPS/inertial exterior orientations for photogrammetric applications. In: *International Archives of Photogrammetry and Remote Sensing*, Amsterdam, The Netherlands, *Vol. XXXIII, Part B3/1*, pp. 198-205.

27.Dall'Asta, E., Delaloye, R., Diotri, F., Forlani, G., Fornari, M., Morra di Cella, U., Pogliotti, P., Roncella, R., & Santise, M. (2015). Use of UAS in a high mountain landscape: the case of Gran Sommetta rock glacier (Ao). In: *ISPRS – International Archives Photogrammetry, Remote Sensing and Spatial Information Sciences., Vol. XL-3/W3*, pp. 391-397, doi:10.5194/isprsarchives-XL-3-W3-391-2015, 2015.

28.Dall'Asta, E., Thoeni, K., Santise, M., Forlani, G., Giacomini, A., & Roncella, R. (2015). Network Design and Quality Checks in Automatic Orientation of Close-Range Photogrammetric Blocks. In: *Sensors*, *15*(4), 7985-8008.

29.Delaloye, R., Morard, S., Barboux, C., Abbet, D., Gruber, V., Riedo, M., & Gachet, S. (2013). Rapidly moving rock glaciers in Mattertal. In: *Mattertal– Ein Tal in Bewegung. (St Niklaus. Birmensdorf, Eidg. Forschungsanstalt WSL: Graf, C. (Red.)), 21-31*.

30.Deseilligny, M. P., & Paparoditis, N. (2006). A multiresolution and optimization-based image matching approach: An application to surface reconstruction from SPOT5-HRS stereo imagery. In: *IAPRS-Archives of Photogrammetry, Remote Sensing and Spatial Information Sciences, Vol. XXXVI/(1/W41),* 5 pages (on CD-ROM).

31.Deseilligny, M. P., & Clery, I. (2011). Apero, an open source bundle adjusment software for automatic calibration and orientation of set of images. In: *ISPRS – International Archives of the Photogrammetry, Remote Sensing*

and Spatial Information Sciences, *Vol. XXXVIII–5/W16*, pp.269-276. doi:10.5194/isprsarchives-XXXVIII-5-W16-269-2011, 2011.
32.DHL parcelcopter, 2014. DHL Global. http://www.dhl.com/en/press/releases/releases_2014/group/dhl_parcelcopter_launches_initial_operations_for_research_purposes.html (last access 15/01/2016).
33.d'Oleire-Oltmanns, S., Marzolff, I., Peter, K. D., & Ries, J. B. (2012). Unmanned Aerial Vehicle (UAV) for monitoring soil erosion in Morocco. *Remote Sensing*, *4*(11), pp. 3390-3416.
34.Dowman, I., 2012. More than information from imagery. In: *Geospatial World, Vol.* 2, pp. 34–44.
35.Dronecode, 2016. Dronecode Project, Inc., a Linux Foundation Collaborative Project. https://www.dronecode.org/ (last access 15/01/2016).
36.DiYDrones.com, 2016. DiYDrones the leading community for personal UAVs. http://diydrones.com/ (last access 15/01/2016).
37.Easyfly, 2015. Eurodrone flight system Easyfly, http://www.eurodrone.it/engine.aspx?qsPage=34&qsPadre=7 (last access 20/10/2015).
38.Ebee, 2016. SenseFly a Parrot company, © senseFly 2009 – 2015, https://www.sensefly.com/drones/ ebee-rtk.html (last access 15/01/2016).
39.Eisenbeiß, H. (2009). *UAV photogrammetry*. Zurich, Switzerland:: ETH.
40.Eling, C., Klingbeil, L., Wieland, M., & Kuhlmann, H. (2013). A precise position and attitude determination system for lightweight unmanned aerial vehicles. In: *ISPRS – International Archives of the Photogrammetry, Remote Sensing and Spatial Information Sciences*, *Vol. XL-1/W2*, pp. 113-118.
41.Fischler, M. A., & Bolles, R. C. (1981). Random sample consensus: a paradigm for model fitting with applications to image analysis and automated cartography. *Communications of the ACM*, *Vol. 24*(6), pp. 381-395.
42.Forlani, G., 1986. Sperimentazione del nuovo programma CALGE dell’ITM. In: *Bollettino SIFET, Vol. 2*, pp. 63-72.
43.Forlani, G., & Pinto, L. (1994, August). Experiences of combined block adjustment with GPS data. In: *Spatial Information from Digital Photogrammetry and Computer Vision: ISPRS Commission III Symposium*, pp. 219-226. International Society for Optics and Photonics.
44.Forlani, G., Pinto, L., & Scaioni, M. (1998). The TRIADIGIT program for AAT. In: *IAPRS – International Archives of Photogrammetry and Remote Sensing*, *Vol* 32(2), pp. 67–73.

45.Forlani, G., & Pinto, L. (2007, May). GPS-assisted adjustment of terrestrial blocks. In: *Proceeding of the 5th International. Symposium on Mobile Mapping Technology (MMT'07). Padova,* (on CD-ROM). *ISSN,* pp. 1682-1777.
46.Forlani, G., Pinto, L., Roncella, R., & Pagliari, D. (2014). Terrestrial photogrammetry without ground control points. *Earth Science Informatics*, *Vol 7*(2), 71-81.
47.Friess, P. (1986). A Simulation Study on the Improvement of Aerial Triangulation by Navigation Data, *ISPRS Comm. III Symposium, Rovaniemi,* pp. 269-283.
48.Furukawa, Y., & Ponce, J. (2010). Accurate, dense, and robust multiview stereopsis. In: *Pattern Analysis and Machine Intelligence, IEEE Transactions on, Vol. 32(8),* pp. 1362-1376.
49.Gini, R., Passoni, D., Pinto, L., & Sona, G. (2012). Aerial images from an UAV system: 3d modeling and tree species classification in a park area. In: *International Archives of the Photogrammetry, Remote Sensing and Spatial Information Sciences, Vol. XXXIX/B1,* pp. 361-366.
50.Gini, R., Pagliari, D., Passoni, D., Pinto, L., Sona, G., Dosso, P., ... & BILL, R. (2013). UAV photogrammetry: Block triangulation comparisons. In: *International Archives of the Photogrammetry, Remote Sensing and Spatial Information Sciences, Vol. XL-1/W2,* pp.157-162.
51.Goesele, M., Snavely, N., Curless, B., Hoppe, H., & Seitz, S. M. (2007, October). Multi-view stereo for community photo collections. In: *Computer Vision, 2007. ICCV 2007. IEEE 11th International Conference on* (pp. 1-8). IEEE.
52.Gonzalez, J. P., Nagy, B., & Stentz, A. (2006). The geometric path planner for navigating unmanned vehicles in dynamic environments. In: *American Nuclear Society 1st joint emergency preparedness and response and robotic and remote systems, Vol.2,* pp. 405- 411.
53.González-Aguilera, D., Fernández-Hernández, J., Mancera-Taboada, J., Rodriguez-Gonzálvez, P., Hernández-López, D., Felipe-García, B., ... & Arias-Perez, B. (2012). 3D modelling and accuracy assessment of Granite Quarry using unmanned aerial vehicle. In: *ISPRS - Annals of the Photogrammetry, Remote Sensing and Spatial Information, Vol. I-3,* pp. 37-42.
54.Granshaw, S. I. (1980). Bundle adjustment methods in engineering photogrammetry. In: *The Photogrammetric Record, Vol. 10*(56), 181-207.
55.Grenzdörffer, G. J., Engel, A., & Teichert, B. (2008). The photogrammetric potential of low-cost UAVs in forestry and agriculture. In: *ISPRS - The*

International Archives of the Photogrammetry, Remote Sensing and Spatial Information Sciences, Vol. XXXI/B3, pp. 1207-1214.

56.Gruen, A. (1985). Adaptive least squares correlation: a powerful image matching technique. In: *South African Journal of Photogrammetry, Remote Sensing and Cartography, Vol. 14*(3), pp. 175-187.

57.Gruen, A., 2012. Unmanned Aerial Vehicles. In: *Geoinformatics, Vol. 1,* pp. 14-16.

58.Gurtner, W., RINEX: The receiver independent exchange Format version 2, 1997.

59.Haala, N., & Rothermel, M. (2012). Dense multiple stereo matching of highly overlapping UAV imagery. In: *ISPRS-International Archives of the Photogrammetry, Remote Sensing and Spatial Information Sciences, Vol. XXXIX/ B1,* pp. 387-392.

60.Haala, N., Cramer, M., Weimer, F., & Trittler, M. (2011). Performance test on UAV-based photogrammetric data collection. In: *ISPRS - International Archives of the Photogrammetry, Remote Sensing and Spatial Information Sciences, Vol. XXXVIII-1/C22,* pp. 7-12.

61.Haarbrink, R. B., & Eisenbeiss, H. (2008). Accurate DSM production from unmanned helicopter systems. *ISPRS - International Archives of the Photogrammetry, Remote Sensing and Spatial Information Sciences, Vol. XXXVII/B1,* pp. 1259-1264.

62.Haeberli, W. (2013). Mountain permafrost—research frontiers and a special long-term challenge. In: *Cold Regions Science and Technology, Vol. 96,* pp. 71-76.

63.Hartley, R., & Zisserman, A. (2003). *Multiple view geometry in computer vision.* Cambridge university press.

64.Heipke, C. (1997). Automation of interior, relative, and absolute orientation. In: *ISPRS journal of photogrammetry and remote sensing, Vol. 52*(1), pp. 1-19.

65.Heipke C., Jacobsen K., Wegmann H., Andersen Ø., Nilsen B. (2000): Integrated Sensor Orientation – an OEEPE Test. In: *IAPRS – International Archives of Photogrammetry and Remote Sensing, Vol. XXXIII, Part B3/1,* pp. 373-380.

66.Hirokawa, R., Kubo, D., Suzuki, S., Meguro, J. I., & Suzuki, T. (2007, May). A small UAV for immediate hazard map generation. In: *AIAA – American Institute of Aeronautics and Astronautics, Infotech@ Aerospace 2007 Conference and Exhibit,* pp. 2725-2748. (doi: 10.2514/6.2007-2725).

67.Hirschmüller, H. (2008). Stereo processing by semiglobal matching and mutual information. In: *Pattern Analysis and Machine Intelligence, IEEE Transactions on, Vol. 30(2),* pp. 328-341.
68.Honkavaara, E., Ahokas, E., Hyyppä, J., Jaakkola, J., Kaartinen, H., Kuittinen, R., ... & Nurminen, K. (2006). Geometric test field calibration of digital photogrammetric sensors. In: *ISPRS Journal of Photogrammetry and Remote Sensing, Vol. 60(6),* pp. 387-399.
69.James, M. R., & Robson, S. (2014). Mitigating systematic error in topographic models derived from UAV and ground-based image networks. In: *Earth Surface Processes and Landforms, Vol. 39(10),* pp. 1413-1420.
70.Kraus, K. (1993). *Photogrammetry: V. 1, Fundamentals and Standard Processes*. Ferdinand Dummlers Verlag.
71.Kraus, K. (1997). *Photogrammetry. Vol. 2*. Dummler, Bonn, Germany, 466 pp.
72.Kraus, K. (2007). *Photogrammetry: geometry from images and laser scans*. Walter de Gruyter.
73.Küng, O., Strecha, C., Beyeler, A., Zufferey, J. C., Floreano, D., Fua, P., & Gervaix, F. (2011). The accuracy of automatic photogrammetric techniques on ultra-light UAV imagery. In: *ISPRS - International Archives of the Photogrammetry, Remote Sensing and Spatial Information Sciences, Volume XXXVIII-1/C22,* pp. 125-130.
74.Laliberte, A. S., Herrick, J. E., Rango, A., & Winters, C. (2010). Acquisition, orthorectification, and object-based classification of unmanned aerial vehicle (UAV) imagery for rangeland monitoring. In: *Photogrammetric Engineering & Remote Sensing, Vol. 76*(6), pp. 661-672.
75.Leberl, F., Irschara, A., Pock, T., Meixner, P., Gruber, M., Scholz, S., & Wiechert, A. (2010). Point Clouds: Lidar versus 3D Vision. In: *Photogrammetric Engineering & Remote Sensing, Vol. 76(10),* pp. 1123-1134.
76.Lowe, D. G. (2004). Distinctive Image Features from Scale-Invariant Keypoints. In: *International Journal of Computer Vision*, pp. 91-110.
77.Lucieer, A., de Jong, S., & Turner, D. (2013). Mapping landslide displacements using Structure from Motion (SfM) and image correlation of multi-temporal UAV photography. In: *Progress in Physical Geography, Vol. 38(1),* pp 97-116.
78.Linux Foundation (2016). The Linux Foundation Copyright © 2016 Linux Foundation. All rights reserved http://www.linuxfoundation.org/ (last access15/01/2016).

79.Luhmann, T., Robson, S., Kyle, S., & Harley, I. (2006). *Close range photogrammetry: Principles, methods and applications* (pp. 1-510). Whittles.

80.Merino, L., Caballero, F., Martínez-de-Dios, J. R., Maza, I., & Ollero, A. (2012). An unmanned aircraft system for automatic forest fire monitoring and measurement. In: *Journal of Intelligent & Robotic Systems, Vol. 65(1-4)*, pp. 533-548.

81.Mikolajczyk, K., & Schmid, C. (2004). Scale & affine invariant interest operator point detectors. In: *International Journal of computer vision, Vol. 60* (1), pp. 63-86.

82.Mission Planner, 2015. Mission Planner Ground Station, http://planner.ardupilot.com/ (last access 18/10/2015).

83.Morel, J. M., & Yu, G. (2009). ASIFT: A new framework for fully affine invariant image comparison. *SIAM Journal on Imaging Sciences*, *Vol. 2*(2), pp. 438-469.

84.Mohamed, H. A., Hansen, J. M., Elhabiby, M. M., El-Sheimy, N., & Sesay, A. B. (2015). Performance Characteristic Mems-Based IMUs for UAVs Navigation. In: *ISPRS-International Archives of the Photogrammetry, Remote Sensing and Spatial Information Sciences*, *Vol. XL-1/W4*, pp. 337-343.

85.Nex, F., & Remondino, F. (2014). UAV for 3D mapping applications: a review. In: *Applied Geomatics*, *Vol. 6*(1), pp. 1-15.

86.Niranjan, S., Gupta, G., Sharma, N., Mangal, M., & Singh, V. (2007). Initial efforts toward mission-specific imaging surveys from aerial exploring platforms: UAV. In: *GIS development, Map World Forum, Hyderabad, India*.

87.Nocerino, E., Menna, F., & Remondino, F. (2014). Accuracy of typical photogrammetric networks in cultural heritage 3D modeling projects. In: *ISPRS-International Archives of the Photogrammetry, Remote Sensing and Spatial Information Sciences, Vol. XL-5*, pp. 465-472.

88.Nordberg, K., Doherty, P., Farnebäck, G., Forssén, P. E., Granlund, G., Moe, A., & Wiklund, J. (2002, October). Vision for a UAV helicopter. In: *International Conference on Intelligent Robots and Systems (IROS), workshop on aerial robotics. Lausanne, Switzerland*.

89.Nowozin, S., 2006. Libsift - Scale-invariant feature transform implementation. http://www.nowozin.net/sebastian/tu-berlin-2006/autopano-sift/.

90.Papo, H. B. (1985). Extended free net adjustment constraints. In: *Bulletin géodésique*, *Vol. 59*(4), pp. 378-390.

91.Pérez, M., Agüera, F., & Carvajal, F. (2011). Digital camera calibration using images taken from an unmanned aerial vehicle. In: *ISPRS-The*

International Archives of the Photogrammetry, Remote Sensing and Spatial Information Sciences, Vol. XXXVIII-1/C22, pp. 167-171.

92.Pettersson, P. O., & Doherty, P. (2004). Probabilistic roadmap based path planning for an autonomous unmanned aerial vehicle. In: *Sensors*, *200*, 66Hz.

93.Pix4D Mapper, 2015. Pix4D SA, https://pix4d.com/pix4dmapper-pro/ (last access 20/10/2015).

94.PhotoModeler, 2015. © 2014 Eos Systems Inc., http://www.photomodeler.com/index.html (last access 21/10/2015).

95.Püschel, H., Sauerbier, M., & Eisenbeiss, H. (2008). A 3D model of Castle Landenberg (CH) from combined photogrammetric processing of terrestrial and UAV-based images. In: *ISPRS-International Archives of the Photogrammetry, Remote Sensing and Spatial Information Sciences, Vol. XXXVII. Part B6b*, pp. 93-98.

96.Re, C., Roncella, R., Forlani, G., Cremonese, G. & Naletto, G., (2012). Evaluation of area-based image matching applied to DTM generation with Hirise images. In: *ISPRS Annals of Photogrammetry, Remote Sensing and Spatial Information Sciences, Vol. I-4*, pp. 209-214.

97.Rehak, M., Mabillard, R., & Skaloud, J. (2013). A micro-UAV with the capability of direct georeferencing. In: *ISPRS Annals of Photogrammetry, Remote Sensing and Spatial Information Sciences, Vol XL-1/W2*, pp. 317-323.

98.Remondino, F., & El-Hakim, S. (2006). Image-based 3D Modelling: A Review. In: *The Photogrammetric Record*, *Vol. 21*(115), pp. 269-291.

99.Remondino, F., & Fraser, C. (2006). Digital camera calibration methods: considerations and comparisons. In: *IAPRS-International Archives of Photogrammetry and Remote Sensing*, *Vol. XXXVI, Part (5*), pp. 266-272.

100.Remondino, F., El-Hakim, S., Gruen, A., & Zhang, L. (2008). Turning images into 3-D models. In: *Signal Processing Magazine, IEEE*, *Vol. 25*(4), pp. 55-65.

101.Remondino, F., Gruen, A., von Schwerin, J., Eisenbeiss, H., Rizzi, A., Girardi, S., ... & Richards-Rissetto, H. (2009, October). Multi-sensor 3D documentation of the Maya site of Copan. In: *22nd CIPA Symposium, Kyoto, Japan*, pp. 131-1.

102.Remondino, F., Barazzetti, L., Nex, F., Scaioni, M., Sarazzi, D., (2011). UAV photogrammetry for mapping and 3D modelling — current status and future perspectives. In: *ISPRS – International Archives of Photogrammetry, Remote Sensing and Spatial Information Sciences*, *Vol. XXXVIII-1/C22*, pp. 25–31.

103.Remondino, F., Del Pizzo, S., Kersten, T. P., & Troisi, S. (2012). Low-cost and open-source solutions for automated image orientation – A critical overview. In: *Progress in Cultural Heritage Preservation* (pp. 40-54). Springer Berlin Heidelberg.

104.Rieke, M., Foerster, T., Geipel, J., & Prinz, T. (2011). High-precision positioning and real-time data processing of UAV-systems. In: *ISPRS-International Archives of Photogrammetry, Remote Sensing and Spatial Information Sciences, Vol. XXXVIII-1/C22,* pp. 119-124.

105.Rinaudo, F., Chiabrando, F., Lingua, A. M., & Spanò, A. T. (2012). Archaeological site monitoring: UAV photogrammetry can be an answer. In: *ISPRS-International Archives of the Photogrammetry, Remote Sensing and Spatial Information Sciences, Vol. XXXIX-B5,* pp. 583-588.

106.Ro, K., Oh, J. S., & Dong, L. (2007, January). Lessons learned: Application of small uav for urban highway traffic monitoring. In: *45th AIAA Aerospace Sciences Meeting and Exhibit* (pp. 2007-596).

107.Roncella, R., Re, C., & Forlani, G. (2011). Performance evaluation of a structure and motion strategy in architecture and cultural heritage. In: *ISPRS-International Archives of the Photogrammetry, Remote Sensing and Spatial Information Sciences, Vol. XXXVIII-5/W16,* pp. 285-292.

108.Rosnell, T., & Honkavaara, E. (2012). Point cloud generation from aerial image data acquired by a quadrocopter type micro unmanned aerial vehicle and a digital still camera. In: *Sensors, Vol. 12(1*), pp. 453-480.

109.Santise, M., Fornari, M., Forlani, G., & Roncella, R. (2014). Evaluation of DEM generation accuracy from UAS imagery. In: *ISPRS-International Archives of the Photogrammetry, Remote Sensing and Spatial Information Sciences, Vol. XL-5,* pp. 529-536.

110.Sasiadek, J. Z., & Dulęba, I. (2000). 3D local trajectory planner for UAV. In: *Journal of Intelligent and Robotic Systems, Vol. 29(2*), pp. 191-210.

111.Schenk, T. (1997). Towards automatic aerial triangulation. In: *ISPRS Journal of Photogrammetry and Remote Sensing, Vol. 52(*3), pp. 110-121.

112.Scharstein, D., & Szeliski, R. (2002). A taxonomy and evaluation of dense two-frame stereo correspondence algorithms. In: *International journal of computer vision, Vol. 47(1-3),* pp. 7-42.

113.Snavely, N., Seitz, S. M., & Szeliski, R. (2006, July). Photo tourism: exploring photo collections in 3D. In: *ACM transactions on graphics (TOG), Vol. 25, No. 3,* pp. 835-846. ACM.

114.Snavely, N., Seitz, S. M., & Szeliski, R. (2008, June). Skeletal graphs for efficient structure from motion. In: *CVPR, Vol. 1,* p. 2.

115.Stempfhuber, W. (2013). 3D-RTK Capability of Single Gnss Receivers. In: *ISPRS-International Archives of the Photogrammetry, Remote Sensing and Spatial Information Sciences, Vol. XL-1/W2*, pp. 379-384.

116.Sturm, P., Ramalingam, S., Tardif, J. P., Gasparini, S., & Barreto, J. (2011). Camera models and fundamental concepts used in geometric computer vision. In: *Foundations and Trends® in Computer Graphics and Vision, Vol. 6*(1–2), pp. 1-183.

117.SwingletCAM, 2015. SenseFly a Parrot company, © senseFly 2009 – 2015, https://www.sensefly.com/drones/swinglet-cam.html (last access 20/10/2015).

118.Szeliski, R., 2011. *Computer Vision – Algorithms and Applications*. Springe Science &Business Media.

119.Takasu, T., & Yasuda, A. (2008). Evaluation of RTK-GPS performance with low-cost single-frequency GPS receivers. In: *Proceedings of international symposium on GPS/GNSS* (pp. 852-861).

120.Takasu, T., & Yasuda, A. (2009, November). Development of the low-cost RTK-GPS receiver with an open source program package RTKLIB. In: *International symposium on GPS/GNSS* (pp. 4-6). Jeju, Korea: International Convention Centre.

121.Takasu, T.RTKLIB: Open Source Program Package for RTK-GPS, *FOSS4G 2009 Tokyo*, Japan, November 2, 2009.

122.Toldo, R., Fantini, F., Giona, L., Fantoni, S., & Fusiello, A. (2013). Accurate multiview stereo reconstruction with fast visibility integration and tight disparity bounding. In: *ISPRS-International Archives of Photogrammetry, Remote Sensing and Spatial Information Sciences, VOL. XL/(5/W1)*, pp. 243-249.

123.Vallet, J., Panissod, F., Strecha, C., & Tracol, M. (2011). Photogrammetric performance of an ultra light weight swinglet UAV. In: *ISPRS-International Archives of the Photogrammetry, Remote Sensing and Spatial Information Sciences, Vol. XXXVIII-1/C22*, pp. 253-258.

124.Van Der Vegt, J. W. (1989). GPS Test Flight Flevoland. In. *Proceedings of the 42nd Photogrammetric Week*, Stuttgart University, 11-16. Sept. 1989, pp. 285-298.

125.Vedaldi, A., & Fulkerson, B. (2010, October). VLFeat: An open and portable library of computer vision algorithms. In: *Proceedings of the international conference on Multimedia* (pp. 1469-1472). ACM.

126.Vuicin, L., 2014. Mapping a large copper mine - A Romanian UAV project. In: *GEOInformatics, Vol. 17(3)*, pp. 22-24.

127.Ullman, S. (1979). The interpretation of structure from motion. In: *Proceedings of the Royal Society of London B: Biological Sciences, Vol. 203(1153),* pp. 405-426.

128.Wallis, R., 1976. An approach to the space variant restoration and enhancement of images. In: *Image Sciences*, Proceedings, Symposium on Current Mathematical Problems in Image Science, Monterey, California, Nov. 1976), Western Periodicals, North Hollywood, 1977, pp. 10-12.

129. Warner, W.S., Graham, R.W., & Read, R.E. 1996. *Small format AERIAL PHOTOGRAPHY*. Whittles Publishing, Caithness (Scotland), UK, p. 348.

130.Wiśniewski, B., Bruniecki, K., & Moszyński, M. (2013). Evaluation of RTKLIB's Positioning Accuracy Using low-cost GNSS Receiver and ASG-EUPOS. In: *TransNav: International Journal on Marine Navigation and Safety of Sea Transportation, Vol. 7(*1), pp. 79-85.

131. Wu, C. (2011). VisualSFM: A visual structure from motion system. *URL: http://homes. cs. washington. edu/~ ccwu/vsfm*, *9*.

132.Wu, J., & Zhou, G. (2006, July). High-resolution planimetric mapping from UAV video for quick-response to natural disaster. *Geoscience and Remote Sensing Symposium, 2006. IGARSS 2006. IEEE International Conference on (pp. 3333-3336). IEEE.*

133.Yoo, C. S., & Ahn, I. K. (2003, October). Low cost GPS/INS sensor fusion system for UAV navigation. In: *Digital Avionics Systems Conference, 2003. DASC'03. The 22nd, Vol. 2,* pp. 8-A. IEEE.

134.3drobotics, 2015. 3dRobotics corporate website, https://3drobotics.com/kb/follow-instructions/ (last access 15/10/2015).

135.3drobotics Pixhawk, 2015. 3DR Pixhawk https://store.3dr.com/products/3dr-pixhawk (last access 15/01/2015).

Ringraziamenti

Questa tesi è frutto del lavoro di tre anni presso il DICATeA, durante i quali ho collaborato con tante persone che ci tengo a ringraziare.

Un sincero e affettuoso grazie va al mio relatore, il Prof. Gianfranco Forlani, una guida capace di sostenermi, illuminarmi e ispirarmi dal primo all'ultimo giorno. Grazie al Prof. Riccardo Roncella perché ha generosamente profuso passione, entusiasmo e dedizione verso la nostra ricerca. Entrambi hanno contribuito alla mia crescita lavorativa e personale e mi hanno dato la possibilità di conoscere e collaborare con professionisti competenti e divertenti. Per cui i miei ringraziamenti vanno all'Ing. Fabrizio Diotri, al Dott. Umberto Morra di Cella, all'Ing. Diana Pagliari, all'Ing. Daniele Passoni, al Prof. Livio Pinto, all'Arch. Andrea Zerbi, all'Ing. Klaus Thoeni e alla Prof.ssa Anna Giacomini.

Ringrazio i miei colleghi e amici Matteo, Cristina, Giorgia e Nazarena per il supporto, la fiducia e l'empatia, e soprattutto Elisa per essermi stata costantemente vicina con tanto affetto. Un grazie ai dottorandi Camilla, Roberta, Paolo, Federico e Fausto, tutti disperati come me ma in grado di trovare un momento per ascoltarmi e aiutarmi.

Infine grazie a chi mi ha letteralmente sopportato ogni giorno, dalla mattina da zombie alla sera da stordita, a CasaMonteNero_SaporeVero in questi tre bellissimi anni di follia. Grazie a Gabriella perché è stupendamente speciale ed è mio sorella, grazie ad Emiliana perché è una grande amica affidabile e generosa, grazie a Chiara perché una forza della natura.